Dipl.-Ing. Herbert Reingruber

New microscopic methods for the characterization of microfiltration membranes

DOCTORAL THESIS

For obtaining the academic degree of

Doktor der technischen Wissenschaften

Doctoral Programme of Technical Sciences
Technical Physics

Graz University of Technology

Supervisor:

Univ.-Doz. Dipl.-Ing. Dr.techn. Peter Pölt

Institute for Electron Microscopy and Fine Structure Research

Graz, September 2012

Kurzfassung

Filtration stellt heute eine entscheidende Methode in der Separations-Technologie dar. Sie wird in vielen wissenschaftlichen und technischen Bereichen wie etwa in der Medizin, Biotechnologie etc. oder auch in der Wasseraufbereitung eingesetzt. Kürzlich entwickelte Membranen für die Mikrofiltration zeichnen sich durch hohe Durchflussraten bei sehr genau definiertem Rückhaltevermögen aus. Die dafür notwendige Membranstruktur ist meist sehr komplex und besteht häufig aus mehreren asymmetrisch angeordneten Schichten: einer sehr dünnen Trennschicht und verschieden breiten Stützschichten auf beiden Seiten der Trennschicht. Die mechanische Stabilität ist durch die Stützschicht gegeben, während die Filtereigenschaften durch die Porenstruktur der Trennschicht bestimmt werden. Besonders wichtig für die weitere Entwicklung und Optimierung der Membranstruktur sind neue Methoden zur Membrancharakterisierung im Mikrobereich. Die vorliegende Arbeit präsentiert zwei neue rasterelektronenmikroskopische Methoden für die Charakterisierung der Struktur von Mikro-Filtrationsmembranen auf Polymerbasis.

Eine Methode beschäftigt sich mit der dreidimensionalen (3D) Rekonstruktion der Membranstruktur. Das grundlegende Verfahren besteht im automatisierten sequentiellen Schneiden der Membran und dem darauf folgenden Abbilden des jeweils neu geschaffenen Membranquerschnittes. Zu diesem Zweck wurde ein miniaturisiertes Ultramikrotom in die Probenkammer eines Niedervakuum Rasterelektronenmikroskops (ESEM) eingebaut. Die nach den herkömmlichen Verfahren für die Ultramikrotomie präparierten Membranproben wurden mit einem Diamantmesser geschnitten und die jeweils frische. Oberfläche dann im ESEM abgebildet. Die Anzahl der Schnitte und die Schnittdicke, im vorliegenden Fall 50 nm, kann vorgegeben werden. Mit dem daraus gewonnenen Bildstapel wurde anschließend eine 3D Rekonstruktion der Membranstruktur mit Hilfe moderner Visualisierungssoftware durchgeführt. Die verwendete Software ermöglichte zusätzlich das Berechnen von Parametern, welche die Membranstruktur auch quantitativ charakterisieren. So konnten zum Beispiel die Volumenporosität, die spezifische Oberfläche, die Konnektivität der Poren untereinander und die Verteilung der Porendurchmesser sowie die Permeabilität der Membranstruktur berechnet werden. Da bei den untersuchten Membranen die Porenstruktur entlang des Membranquerschnittes stark variierte, wurden Parameterprofile ermittelt, welche die Änderung der entsprechenden Parameter entlang des Membranquerschnittes darstellen. Die daraus bestimmten Mittelwerte wurden dann mit experimentell bestimmten Daten sowie den Herstellerangaben verglichen.

Andererseits kann mit dieser „*statischen*“ Methode aber keine Aussage über die dynamische Wechselwirkung zwischen den Porenwänden (hydrophil oder hydrophob) und der Flüssigkeit getroffen werden. Um diese ebenfalls zu erhalten, wurde die Probenkammer des Mikroskops als Mikro-Labor eingesetzt und das Benetzungs- und Trocknungsverhalten der Membranen mit Wasser untersucht. Ein eigens dazu entwickelter Versuchsaufbau ermöglichte die Beobachtung der Interaktion von Poren und Wasser bei hoher Vergrößerung und großer Schärfentiefe und die Bestimmung der Anzahl und der Größenverteilung von nassen und trockenen Poren an der Membranoberfläche während des Benetzungs/Trocknungsvorganges. Im Mikroskop kann jedoch nur die Membranoberfläche direkt beobachtet werden. Um Aufschluss über die entsprechenden Parameter im Membraninneren zu bekommen, wurde simultan die Temperatur an den Membranoberflächen gemessen. Die gewonnenen Temperaturcharakteristika reflektieren den inneren (asymmetrischen) Membranaufbau, da das im Inneren der Membran verdampfende Wasser auch die Temperatur der Membranoberflächen beeinflusst. Wenn man die *makroskopischen Parameter* (Temperatur an den Membranoberflächen) mit den *mikroskopischen Parametern* (Anzahl und Größe der nassen und trockenen Poren) korreliert, dann erlaubt diese neu entwickelte Methode sehr detaillierte, wenn auch großteils nur qualitative Aussage über die Struktur der Membran. Das dabei erfasste Probenvolumen ist ungleich grösser als bei der 3D Rekonstruktion und die damit gewonnenen Aussagen dementsprechend statistisch sehr viel zuverlässiger. Nichtsdestoweniger ergänzen sich die beiden Methoden gegenseitig.

Abstract

Filtration represents one of the most important separation technologies and is used in various fields of science and technology, including medicine, biotechnology and water treatment. Newly developed microfiltration membranes are designed to achieve high flow rates at well defined retention capacities. Therefore the membrane structure often consists of several asymmetrically arranged layers: a very thin separation layer enclosed by backup or support layers of different widths. The mechanical stability of the membrane is provided by the support layer. The actual membrane performance and its properties are largely defined by the pore structure of the separation layer. New methods for membrane characterization at a microscopic scale are essential for future membrane development and optimization. The present work deals with the development of two new electron microscopic methods for the characterization of the structure of microfiltration membranes on a polymeric basis.

One method covers the three dimensional (3D) reconstruction of the membrane structure. The basic procedure is the automated serial slicing and viewing of the membrane cross-section. For this purpose a miniaturized ultramicrotome was mounted in the specimen chamber of an environmental scanning electron microscope (ESEM). The membranes, prepared by methods customarily used in ultramicrotomy, were cut with a diamond knife and the respective surface of the cross-section imaged in the ESEM. Both the number and the thickness of the slices, in the present case 50 nm, can be set in advance. The resultant stacks of images were used to perform 3D reconstructions of the membrane structure using modern 3D visualization software packages. The visualization software also enables the calculation of parameters which characterize the membrane structure quantitatively, for example the inner membrane surface, the volume porosity, the connectivity of the pores, the pore diameter distribution and the permeability. As the structure along the cross-section of the membranes varied strongly, parameter profiles were calculated which show the change of the respective parameters along the membrane cross-section. The mean values determined were compared with experimentally measured data and manufacturers data.

This *"static"* method, however, provides no information about the dynamic interaction between the pore walls (hydrophilic or hydrophobic) and the liquid. The specimen chamber of the microscope was therefore used as micro-laboratory to investigate the wetting and drying behavior of the membranes with water. A special experimental setup allows the interaction between the pores and water to be observed at high magnification and great depth of focus. Additionally the number and size distribution of wet and dry pores during the wetting / drying process were determined. But the microscope only allows direct observation of the membrane surface, the temperatures at the membrane surfaces were measured simultaneously in order to access the processes taking place in the membrane interior. The resulting temperature characteristics reflect the interior membrane structure, as the evaporated water also influences the temperature at the membrane surfaces. Finally, the correlation of the *macroscopic parameters* (temperature at the membrane surface) and the *microscopic parameters* (number and size of dry and wet pores) provide in-depth information about the membrane structure, albeit of a more qualitative nature. The sample volume used in these experiments is much larger than in 3D reconstructions, thus substantially increasing the statistical reliability of the measured parameters. Nevertheless, on the whole, both membrane characterization methods complement one another.

Acknowledgements

Special thanks go to the company Membrana from Wuppertal, Germany, which provided the membrane samples. I am especially grateful to Ramona Tatsch and Jens Osterloh who gave me the opportunity to visit the company at Wuppertal and gain a detailed insight into the production process. They also supplied me with a wealth of background information concerning membrane technology. This work would not have been possible without this support from industry and its keen interest in basic research.

Gaby Stöckl and Peter Westenberger from VSG (visualization science group) gave me the opportunity to test the latest version of AVIZO®Fire (7.0) including the XLAB Hydro package for fluid simulations, which contributed one of the most fruitful parts of the present work.

Colleagues like Armin Zankel and Claudia Mayrhofer made the work at FELMI very pleasant and successful. I benefited from the input of many new ideas to improve my experimental setup and received great support concerning sample preparation at all times.

My supervisor Peter Pölt enabled my attendance at various scientific conferences, where I had the opportunity to present my scientific work to colleagues from around the world. The resulting discussions as well as contacts with other scientists were very important for improving and pushing my work further ahead. Peter reviewed and adapted my abstracts and papers to perfection and I also wish to thank him for all the discussions about membranes.

Deutsche Fassung:
Beschluss der Curricula-Kommission für Bachelor-, Master- und Diplomstudien vom 10.11.2008
Genehmigung des Senates am 1.12.2008

EIDESSTATTLICHE ERKLÄRUNG

Ich erkläre an Eides statt, dass ich die vorliegende Arbeit selbstständig verfasst, andere als die angegebenen Quellen/Hilfsmittel nicht benutzt, und die den benutzten Quellen wörtlich und inhaltlich entnommene Stellen als solche kenntlich gemacht habe.

Graz, am …… ……
(Unterschrift)

Englische Fassung:

STATUTORY DECLARATION

I declare that I have authored this thesis independently, that I have not used other than the declared sources / resources, and that I have explicitly marked all material which has been quoted either literally or by content from the used sources.

…… ……
date (signature)

Nomenclature

G	Gibb´s free enthalpy
H	Enthalpy
T	Temperature
S	Entropy
P	Pressure
V	Volume
μ	Chemical potential
n	Number of …
k_b	Boltzmann constant
Ω	Number of permutations
r	Radius
t	Time
L, l	Length, distance
η	Viscosity
γ	Surface tension
Θ	Contact angle
m	Mass
p_V	Volume porosity
p_A	Fraction of the pore area
ρ	Density
A	Area
q	Flux
λ	Wave length
h	Planck´s constant
$\boldsymbol{F}$	Force
e	Electron charge
$\boldsymbol{v}$	Velocity
$\boldsymbol{B}$	Magnetic field
f	Focus length
d	Diameter
R_{KO}	Interaction radius
A_W	Atomic weight
Z	Atomic number
σ	Cross-section
φ	Scattering angle
ϕ	Volume fraction
E_0	Primary electron energy
J	Ionization potential
BSP	Bethe stopping power
η_{BSE}	Backscattered electrons coefficient
δ	Secondary electrons coefficient
i	Current
α_T	Townsend´s first ionization coefficient
V_a	Detector bias voltage
V_i	Ionization energy of the gas
g	Gain
α	Thermal diffusivity
c_p	Specific heat capacity at constant pressure
λ_{th}	Thermal conductivity
k	Permeability
$\vec{\boldsymbol{k}}$	Permeability tensor
Q	Volume flow

R_{xx}	Local membrane resistance
R_m	Overall membrane resistance
∇	Nabla operator
$\dot{m}$	Mass loss (mass change)
β	Mass transfer number
R	Ideal gas constant
μ_{diff}	Diffusion resistance
δ_{diff}	Diffusion coefficient
n_α	Heat transfer number

Abbreviations

3D	Three dimensional
AFM	Atomic force microscopy
BGPL	Beam gas path length
BSE	Backscattered electrons
BSP	Bethe stopping Power
CFD	Computer fluid dynamics
ESEM	Environmental scanning electron microscope
FEG	Field emission gun
FEM	Finite element method
FIB	Focused ion beam
FTIR	Fourier transform infrared spectroscopy
GSED	Gaseous secondary electron detector
HV	High vacuum
IGP	Ion getter pump
LV	Low vacuum
MF	Micro filtration
MWCO	Molecular weight cut-off
NIPS	Non-solvent induced phase separation
PE	Primary electrons
PES	Polyethersulfone
PLA	Pressure limiting aperture
RO	Reverse osmosis
SBFSEM	Serial block face scanning electron microscope
SE	Secondary electrons
SEM	Scanning electron microscope
TIPS	Thermal induced phase separation
TMF	Trans-membrane flow
TMP	Turbo molecular pump
UF	Ultra Filtration
UHV	Ultra high vacuum
VPSEM	Variable pressure SEM
WLI	White light interferometry

Content

1 Motivation

Filtration is regarded as a key technology of the future. The demand for clean drinking water has risen dramatically over the last years due to higher standards resulting from increased economic development and the significant growth in urban populations. Water and waste water treatment are considered indispensable for solving upcoming problems of water shortage, especially in countries where clean drinking water is rare [1]. The methods used to obtain clean water free of bacteria, germs or toxic substances like heavy metals include reverse osmosis (RO), which is the main method for desalting water, as well as artificial microfiltration (MF) and ultrafiltration (UF) membranes. These membranes are high tech nano-structured products and their properties (bacteria retention rate etc.) are based mostly on their membrane structure. Membrane characterization is thus one of the most important fields in membrane science [2].

Two new characterization methods for asymmetric, flat microfiltration membranes were developed in this work. Both are based on *in situ* experiments in an environmental scanning electron microscope. The main goals were to obtain the essential parameters specifying the membrane structure and to study the interaction between the membrane material and water. This should finally lead to a better understanding of the basic principles of the filtration process.

1.1 Microfiltration membranes[1]

Separation media for microfiltration purposes are widely used in a range of industries such as pharma, biotech, semiconductor, microelectronics, chemistry and water filtration applications (waste water recovery, ultra-pure water, etc.). Portfolio membranes deliver the highest performance and quality concerning retention, flow rates and reliability in microfiltration. Such membranes can be used either in cross-flow filters (e.g. in wine clarification or water applications) or in dead-end filter cartridges (sterile filters for drug solutions or particle removal in the semiconductor industry). Other MF separation media like non-woven media offer higher flow rates but cannot be used for sterile filtration and usually do not show as high retention rates as membranes. Ultrafiltration membranes allow even small particles and microbes such as viruses to be removed. However, the limited flow rates of such membranes prevent them from being used in many processes, especially when virus retention is not required. In order to clarify the general meaning of microfiltration the retention range of microfiltration membranes is shown in Fig. 1.

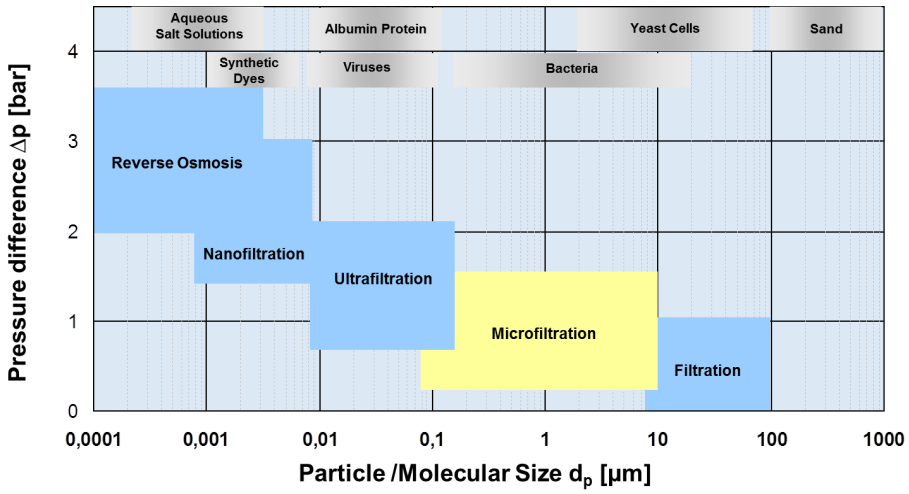

Fig. 1 Overview of filtration applications.
(sketch provided by courtesy of Membrana GmbH, Wuppertal / Germany)

[1] This section was written with the support of Jens Osterloh - Membrana GmbH Wuppertal Germany

The microscopic structure of MF membranes can vary substantially. With regard to particle retention, however, the separation or retention layer is the most important and critical part of a membrane structure. In general, three main types of microstructures can be found in today's portfolio of MF membranes:

- Symmetric membranes: more or less homogenous pore size distribution through the complete cross-section; the full cross-section can be considered as separation layer.
- Asymmetric membranes: are complementary to the symmetric membranes; the pore size distribution is inhomogeneous through the cross-section; only the part with the smallest pores constitutes the separation layer.
- Composite membranes: consist of two or more separate structures forming a composite.

These structures can be found in both capillary and flat sheet membranes and cannot always clearly be classified in practice. Further sub-types include double asymmetric membranes or composite membranes combining elements of different structures. The differences between various membrane structures are illustrated in Fig. 2.

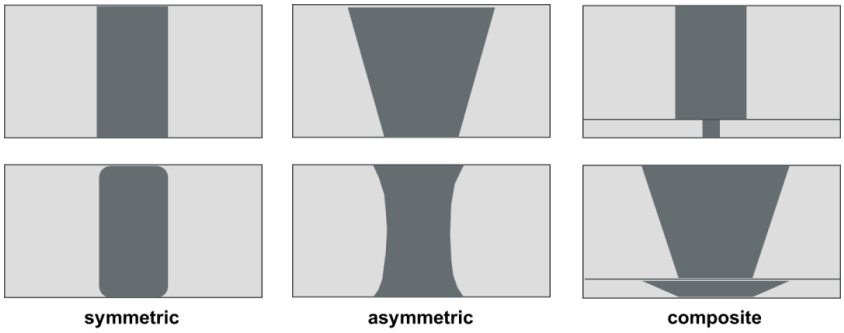

Fig. 2. Types of filtration membrane microstructures.

(sketch provided by courtesy of Membrana GmbH, Wuppertal / Germany)

In addition to structural differences, MF membranes can also be differentiated by measurable parameters like the bubble point (indicating the size of the largest pore in the separation layer), retention of bacteria or particles, trans-membrane flow (TMF), porosity of surface and cross-section or hydrophilicity. Most of the parameters characterizing membranes and their performance are closely related to and influenced by the microscopic structure of the membrane. This also includes material related interactions, e.g. between the membrane polymer or polymer blend and liquids or substances dissolved or suspended in water. This will be illustrated by a few examples.

The results of the bubble point method are determined by the largest pore in the separation layer. The bubble point corresponds to the pressure which is needed to remove a liquid from a fully wetted pore. The pressure is inversely correlated to the size of this pore. Since physical-chemical interactions can be seen as constant for a given liquid and a certain membrane the bubble point is directly and simply correlated to the pore diameter.

The TMF is correlated to more than just one parameter of the membrane structure. For a certain liquid with a given viscosity and physical-chemical interaction potential and a defined membrane material, the TMF depends on the inner surface area, the volume porosity, the thickness of the retention layer (in accordance with the law of Hagen-Poiseuille) and the bubble point. The TMF is enhanced by lower bubble point pressures, high porosity and thinner separation layers. The correlation between TMF and microscopic membrane structure is definitely more complex than for the bubble point.

Another example is the retention of bacteria. If (attractive) physical-chemical interactions between the membrane surface and the bacteria surfaces can be neglected (e.g. by a proper, usually zeta-potential) the retention depends on the bubble point, in other words the maximal pore size of the retention layer, the thickness of the separation layer, the tortuosity (ratio between membrane thickness and the average path length of a pore from surface to surface) and also the porosity.

High porosities and thin retention layers will enhance the probability that bacteria can penetrate a membrane. For example gram-negative bacteria are known for their ability to adapt their surface shape to their environment which may allow them to squeeze through a pore. This is also relevant for tortuosity. Bacteria can more easily "squeeze" through a straight channel (tortuosity factor = 1) than through a highly tortuous "winding" pore. Of course, the pore size is also a key factor for retention.

The latter two examples indicate the great interest in learning more about the correlation of single measurable parameters and the two- or rather three-dimensional (3D) structure of membranes. From the perspective of membrane manufacturing it is possible to control and design the membrane structure by careful control of process parameters. But the performance of such membranes under specific application conditions is often not fully understood, and still not fully predictable. A better understanding of the correlation between the 2 and 3D structure and parameters such as bacteria retention or TMF could help in the design of optimized high performance membranes. Such investigations could provide information about the optimal pore size in the separation layer, its optimal thickness, the most suitable tortuosity and porosity of the membrane in order to provide optimal solutions for a specific separation problem with regard to retention and flow rate.

Against this background, two newly developed microscopic methods, which have the potential to answer the questions elaborated above, are presented in this work. One method allows a 3D reconstruction of the inner membrane structure to calculate such parameters as the porosity, the surface area or the connectivity between the pores. Moreover fluid simulations based on 3D models were performed to calculate the TMF as well as the membrane resistance.

Such static models do not, however, provide information about the nature of the membrane pore surfaces, e.g. whether they are hydrophilic or hydrophobic, or the interaction mechanisms between pore surfaces and fluid. The focus of the second method was thus on investigating of the dynamics of the system "liquid (water) - solid (membrane matrix) - gaseous (water vapor)" during the wetting and drying process of the membrane.

1.2 **Advanced electron microscopy and *in situ* experiments** [3,4]

Electron microscopy is widely used for the characterization of microfiltration membranes. Scanning electron microscopy (SEM) or transmission electron microscopy (TEM) images of the membrane surfaces and cross-sections provide a good impression of the membrane structure. Image processing software can be used to calculate quantitative parameters such as pore diameters, the mean free path and the porous fraction in two dimensions (2D). She et *al*. [5] and Masselin et *al*. [6] describe these calculations for membrane surfaces. A comparison between SEM, atomic force microscopy (AFM) and white light interferometry (WLI) is discussed in [7] using the surface roughness of four different cut-off ceramic membranes as an example and showing 3D visualizations of the membrane surface.

Another method for the quantification of 2D images of membrane cross-sections was developed by Ziel et *al*. [8]. They used single TEM images of the cross-section to quantify the porosity profile. But since they did not reconstruct the 3D pore structure, they were not able to calculate the internal surface area and had to estimate the porosity based on the ratio of the area fraction of the polymer matrix to that of the holes. However, parameters such as the inner specific surface area may be important because the interaction between the pore walls and the fluid could significantly affect membrane performance.

The present study, concentrates on membranes consisting of organic materials. The extraction of 3D information about the membrane structure generally requires serial sectioning and imaging of the membrane embedded in resin. The 3D structure of the membrane can then be reconstructed from the resulting stack of images. Until recently, this was accomplished by sectioning with an ultramicrotome and imaging of the individual sections in the TEM. This is very tedious and time-consuming work, which cannot be fully automated. Moreover, all the images must finally be aligned, a process which itself represents a substantial source of errors. In some cases a 3D impression of the membrane structure was achieved by cutting single sections of the membrane and subsequent image recording in all three directions [9]. But the resulting cube can only give a rough impression of the 3D membrane morphology. A direct calculation of 3D membrane parameters from these images is not possible.

Serial sectioning and imaging using dual beam instruments (focused ion beam [FIB] / SEM) allows 3D reconstruction of the inner sample structure, but only in a rather small field of view, approximately 30 µm × 20 µm. In this case the images are well aligned, but a specimen drift during the sputtering process by the ion beam is nearly unavoidable and requires additional correction routines [10]. The implementation of Gallium ions into the specimen, different sputter rates of the resin and the membrane matrix and especially irradiation damage cause additional problems. Nonetheless this can be the method of choice for inorganic porous materials.

One can get rid of most of the above-mentioned problems by use of serial block face imaging with an ultramicrotome mounted in the specimen chamber of an environmental scanning electron microscope (ESEM). The method called serial block face scanning electron microscopy (SBFSEM), is described in [11]. After each cut not the slice itself, but the corresponding block face of the specimen is imaged, the next cut is then made and the block face is imaged again. This is repeated until the predetermined number of cuts is reached. The whole process can be fully automated and all the images are already aligned. Residual, unavoidable thermal or mechanical sample drift during the cutting procedure can be easily corrected by image processing. But the material must be soft enough to be cut with a diamond knife and hard enough to avoid smearing effects. Various methods like staining with heavy metals can be used for hardening materials that are too soft. Although the SEM provides a lower resolution than the TEM, it is generally sufficient to characterize microfiltration membranes.

A range of other methods has been developed to characterize the membrane morphology and to measure 3D parameters like pore size distribution, connectivity etc. [12-16]. Most of these methods enable the measurement of only one parameter, whereas a 3D model allows the simultaneous extraction of all parameters of interest. But some of these other methods are non-invasive and cause no damage to the membrane.

X-ray tomography, in particular, is a powerful tool for the 3D visualization of complex structures. The sample is exposed to X-rays, with the gray levels of the resulting image corresponding to the absorption of the X-rays in the sample. By rotating the sample many images can be obtained representing the projection of the internal sample structure. This technique enables the visualization of pore structures in the µm size range, which means a much lower resolution than can be obtained by SBFSEM [17].

A single 2D image of the membrane cross-section can be helpful for membrane manufacturers to roughly analyze their membrane structures. Nevertheless, the main goal of the first part of this work is to characterize membranes in a more accurate and direct way than is possible with other established 3D methods.

In the second method the focus is put on the dynamics at the surface or cross-section, but also in the interior of a membrane during the wetting and drying process. Here again the ESEM plays a crucial role in performing the experiments. The wetting and drying process at the membrane surfaces can be directly observed in the microscope. Microscopic parameters such as the size distribution of wet and dry pores can be determined as a function of the wetting / drying time. A macroscopic parameter, the temperature at the membrane surfaces, can be used to study the processes taking place in the interior of the membrane. Correlating the macroscopic parameter with the microscopic ones provides not only a qualitative description of the membrane structure but also information about the interaction water - membrane.

In any case a well established experimental setup is essential for proper results. Cooling stages are commercially available for the investigation of wet samples. In most cases these experimental setups are designed for “standard” investigations and not for measuring e.g. the sample temperature, which is indeed an important parameter. An upgrading of the basic setup is therefore needed in most cases. Jenkins et *al*. [7] used a special sample holder for the investigation of cellulose fibers. The water swelling behavior of the fibers was documented by series of images. Actually every single sample shape (fibers, flat sheet or particles) needed a specially “adapted” holder to provide accurate and repeatable data of the behavior with water.

Hydrophobic and hydrophilic membranes under wet conditions were studied by de la Parra [18], who used an ESEM for the recording of images of the membrane surface during the wetting process. Hydrophobic membranes show water droplet formation at the surface. The droplet shape is in correlation with the hydrophobic level of the membrane material. The shape of the droplet becomes

more and more spherical with increasing hydrophobicity of the membrane surface. The images also show droplet formation at hydrophobic spots at the surface of an otherwise hydrophilic membrane surface. The potential of using an ESEM for localization of less hydrophilic areas was clearly shown. However, the results are more qualitative and do not provide a direct correlation between the membrane structure and the flow of water.

As porous solid materials show characteristic drying rate curves, the drying behavior of membranes should also give information about the interior porous structure [19]. Staude et *al*. used drying rate curves for characterizing different types of membranes [20]. The change in membrane weight during the drying process was measured by a precision balance to obtain characteristic drying rate curves, which are influenced by both the membrane structure and the membrane material. The direct observation of the membrane surface during the drying process and the simultaneous measurement of the membrane weight were not implemented in our microscope setup. Instead of the change in membrane weight, we recorded the change in temperature at both membrane surfaces during the wetting and drying of the membrane with cooled water.

It is vital for the investigations that the dry membrane has a much higher temperature than the cooled water. These temperature-time characteristics provide information about the successive wetting and drying of membrane layers with different pore size distributions and thus about the membrane structure, especially for asymmetric membranes. This is mainly due to the dependence of the capillary force on the pore diameter. Small pores will thus dry more slowly than large ones. As soon as the surface of the membrane is dry it starts to warm up, even if inner membrane layers still contain cooled water. This and other effects entail characteristic features in the temperature-time characteristic, which reflect the membrane structure. The advantage of this method over 3D reconstructions is the much larger volume investigated (membrane volume around 15 mm × 5 mm × 0.15 mm). It provides the additional opportunity to study the interaction between pore surface and water. Changes in the properties of the pore surfaces or membrane fouling may result in changes in the temperature characteristic. If the membrane properties change substantially during operation these characteristics could thus help to find the cause for that change.

Generally the investigation of samples in a wet environment is very critical, even more so when the aim is to obtain quantitative data. The chronology of the experiment is essential and its optimum can be found mostly by trial and error, which can be a challenge. Modern computer-controlled microscopes provide very reproducible environmental conditions, which make *in situ* experiments easier but still with clear limitations. For example, the maximum chamber pressure is limited to 20 Torr, and the electron beam can influence the sample surface, which can lead to misinterpretations of the results obtained. These aspects must be considered when interpreting the results obtained by a “wet” *in situ* experiment.

A short outline of the present work will now be given: In the introduction I will discuss the main aspects of the fabrication of microfiltration membranes and then go on to present established membrane characterization methods with a focus on electron microscopy.

The experimental section starts with an overview of the investigated membranes and their structures including the necessary preparation steps. This is followed by detailed information about the design of the experimental setups used for the investigations. First the basic principles of the established SBFSEM method are discussed, especially in connection with the serial sectioning and imaging of microfiltration membranes. The main steps in the challenging development of a new cooling stage for the investigation of the wetting / drying of membranes are shown and the problems encountered during this work discussed in full detail.

Finally the results of the investigations are documented and discussed in chapters 4 and 5. Chapter 4 presents the reconstructed 3D models of the membrane and compares some of it with those obtained from single SEM images. The basics of computational fluids dynamics (CFD) are explained and the calculated results for parameters such as permeability and trans-membrane flow are compared with the experimental ones. Chapter 5 is devoted to analyzing the wetting and drying behavior of membranes and the information this provides about the membrane structure and properties.

2 Introduction

Polymeric microfiltration membranes are produced in large-scale dimensions, either in flat sheet or tubular form. In any case the phase inversion process is used to obtain the desired membrane pore structure. Production takes place on specially designed large machines, whose construction and process parameters have a significant influence on the final membrane structure. The production process is backed by many years of research and development, resulting in a well reproducible, high quality, error-free membrane. The detailed composition of the cast solution is patented and can be found in [21]. As the present work deals with microfiltration membranes made from polyethersulfone (PES), PES is the basic polymer component. Other additives are also used, however, to provide hydrophilic properties of the resulting membrane structure. The solvent also consists of at least 3 different components. The following description of the phase inversion process describes the simpler case of only 3 components involved: the polymer, the solvent and the non-solvent.

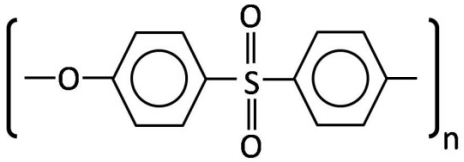

Fig. 3. Chemical structure of polyethersulfone (PES).

2.1 **Phase inversion** [22]

The phase inversion process is the most important method in the production of micro-porous filtration membranes. The principle of the phase inversion can be described by basic thermodynamics and is similar to the thermodynamics of alloys [23].

The basic polymer - in our case polyethersulfone - is dissolved in a mixture of caprolactam and butyrolactone as solvent [24]. The porous membrane structure is formed by the exchange of solvent and non-solvent (in most cases water). Generally the state of the solution, i.e. whether it is stable, meta-stable or instable, is described by the minimum of Gibbs free enthalpy:

$$G = H - TS, \qquad (1)$$

$$dG = VdP - SdT + \sum \mu_i \, dn_i. \qquad (2)$$

For a process at constant temperature and pressure, the free Gibbs enthalpy is given by:

$$\Delta G_m = \Delta H_m - T \, \Delta S_m \, . \qquad (3)$$

Assuming a two component system, two factors determine the Gibbs enthalpy: the entropy of mixing (ΔS_m) and the enthalpy of mixing (ΔH_m). Change of one or both of these parameters can lead to phase separation. Assuming $\Delta H_m = 0$, a stable mixture of the two component solution can be observed when the change in the Gibb's enthalpy has a well pronounced minimum.

The entropy of mixing is related to the molecular weight of the components involved (polymer and solvent). The entropy is determined in statistical physics as follows:

$$S = k_b \, ln \, \Omega \, , \qquad (4)$$

where Ω is the number of microstates of the system. As a consequence, the decrease in the entropy caused by mixing of long polymeric chains is less than that caused by mixing of low molecular weight components or gases (see Fig. 4.) A detailed derivation of the entropy of mixing ΔS_m starting from the statistical entropy can be found in [23,25].

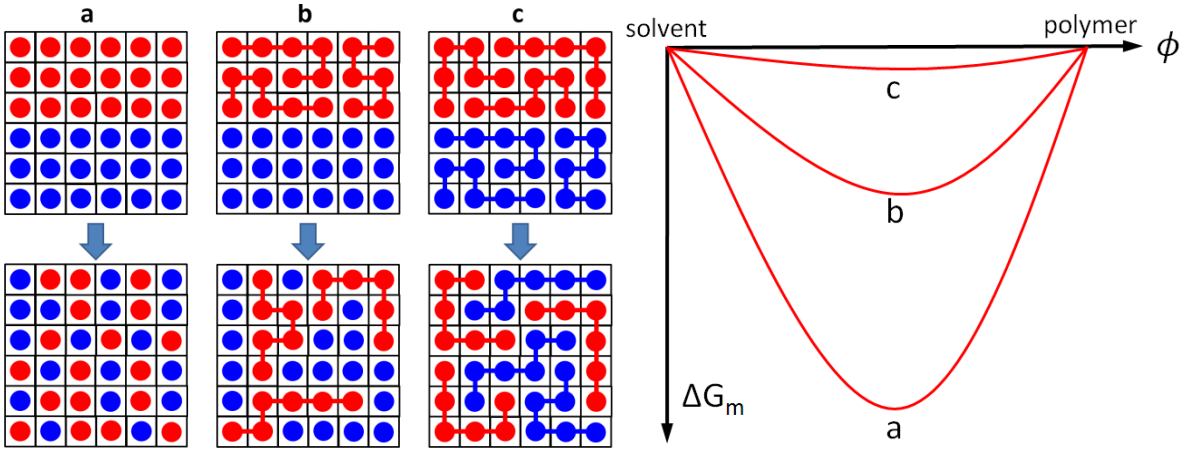

Fig. 4. Sketch of two component mixing: left: a: mixing of low molecular weight components or gases, b: mixing of a polymer solution, c: mixing of long polymeric chains. right: decrease in the Gibbs enthalpy as a function of the volume fraction ϕ for the three cases; adapted from [22].

The minimum in ΔG_m is very significant in 4a, enabling mixing in all ratios. On the other hand, $\Delta G_m$of long polymeric chains provides a flat curve, and demixing can occur as a result of a very small positive enthalpy in the mixing term ($\Delta H_m > 0$). Introducing a positive enthalpy leads to the separation of the components. Two options for the initialization of the phase separation process are commonly used. In many cases, a decrease in temperature leads to an increase in the enthalpy of mixing: temperature-induced phase separation (TIPS) [26]. The adoption of a non-solvent (in the most cases water) can also lead to the desired phase separation: non-solvent-induced phase separation (NIPS) [24,27] (see Fig. 8).

After addition of the non-solvent the components are no longer miscible in all fractions as can be seen in Fig. 5b. As a consequence, the components separate spontaneously (unstable region - miscibility gap) for certain volume ratios ϕ_1 and ϕ_2 (miscibility gap between 1 and 2 in Fig. 5b) and below temperature T_0. Small local fluctuations in the component solution increase and the solution will demix into small interconnected regions of compositions ϕ_I and ϕ_{II} (*spinodal demixing*). In the meta-stable regions the solution is stable against small concentration fluctuations, but small nuclei (large localized concentration variations) can lead to demixing. To enable nucleus growth in between regions ϕ_I and ϕ_1 the composition of the nucleus must be close to ϕ_{II}.

In any case structures obtained from *nucleation and nuclei growth* differ from *spinodal demixing*. This means that the position of the critical point (and as a consequence the position of the miscibility gap) is essential for the final structure. The critical point can be shifted by changing the length of the polymer chains. By increasing the polymer chain length the miscibility gap shifts to the right and also to higher temperatures as shown in Fig. 5c.

Fig. 6 shows a phase diagram for three components. Each edge point represents the pure component (solvent, non-solvent and polymer). A point located inside the triangle represents a mixture of all three components; a point at the borderline represents a mixture of only two components (solvent - non-solvent, polymer - solvent or polymer - non-solvent). Two possible paths representing the phase separation are marked with A and B. The paths can be taken by exchanging solvent with non-solvent (water) until a thermodynamic stable state is reached. The resulting membrane structure depends on the path taken. In the case of path A the meta-stable region is crossed and thus nucleation and nuclei growth dominate, whereas crossing the critical point directly into the miscibility gap will result in spinodal demixing as the major process (path B). Again, both the position of the critical point and the

starting conditions decide whether path A or path B will be taken, and as a consequence which membrane structure will be formed.

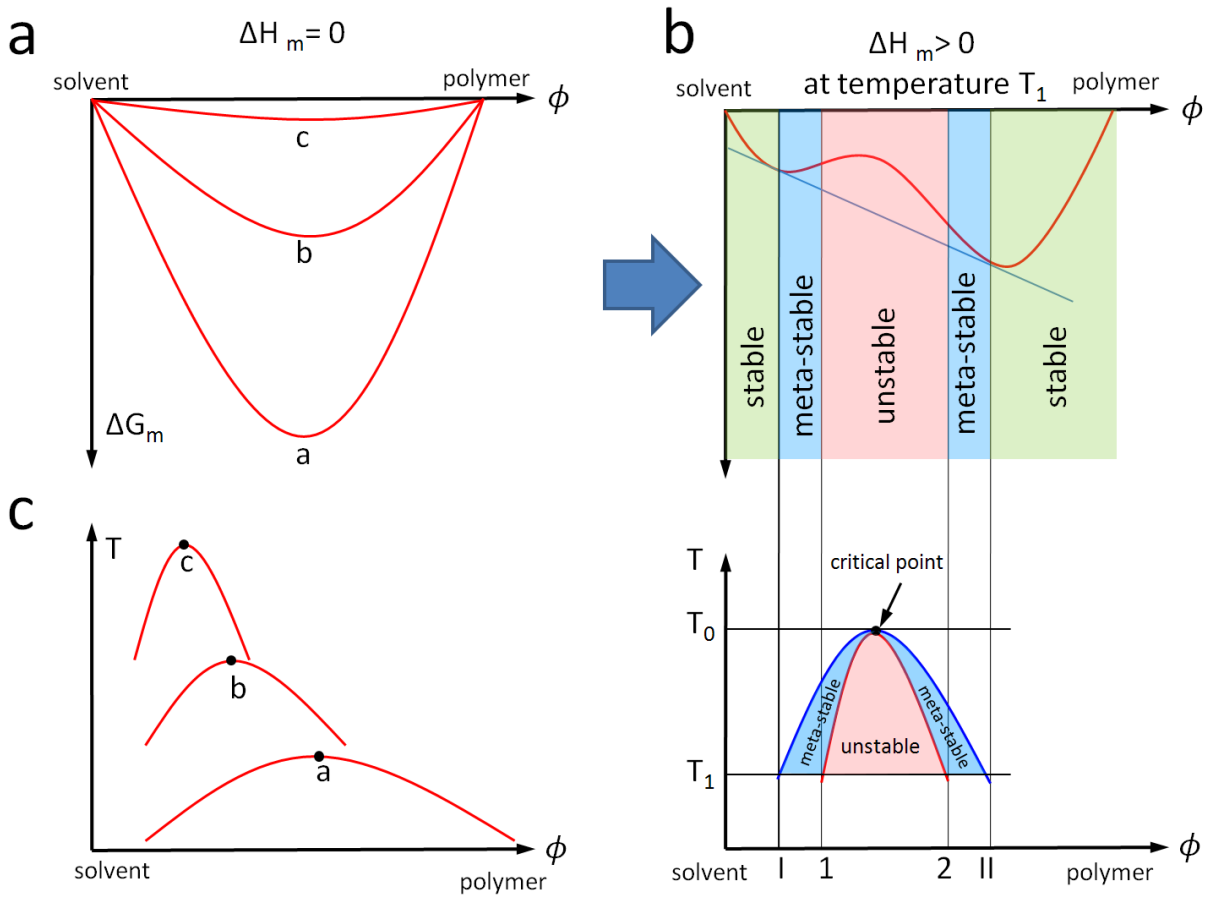

Fig. 5. a: Change in the Gibbs enthalpy as a function of the volume fraction for three different polymer components for ΔH = 0; b: change in the Gibbs enthalpy as a function of the volume fraction for ΔH > 0 and the corresponding phase diagram; c: phase diagram for three different polymer solutions showing position change of the miscibility gap; adapted from [22].

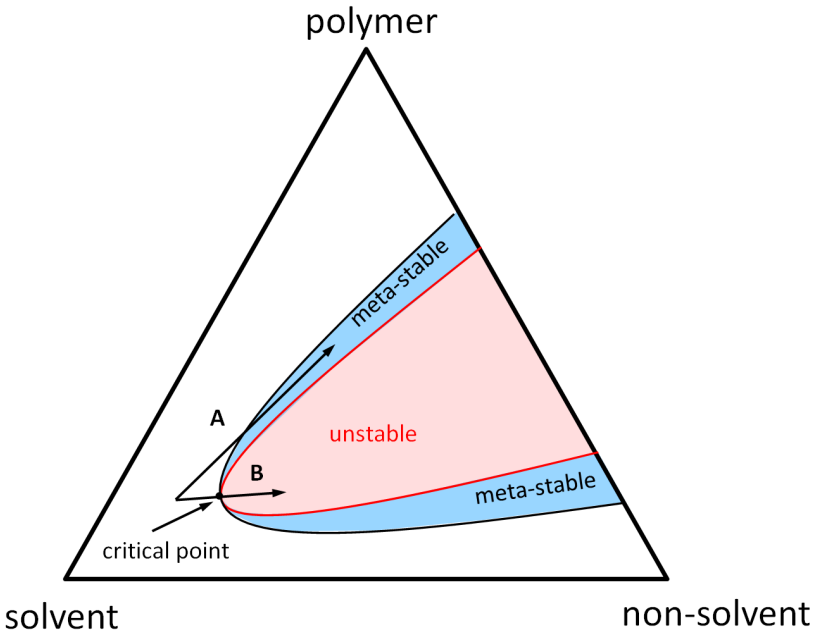

Fig. 6. Phase diagram of three components (solvent, non-solvent and polymer), showing the miscibility gap and two possible paths (A and B) during phase separation; adapted from [22].

Desired asymmetric membrane structures can be achieved by immersion of the polymer-solvent mixture into a non-solvent coagulation bath. A polymer solution consisting of the polymer and the solvent is cast onto a film and immersed into a non-solvent water bath. The non-solvent will replace the solvent until the miscibility gap is reached as described above (Fig. 7). The exchange of both components is determined by the diffusion and the local compositions (the concentration of the components involved).

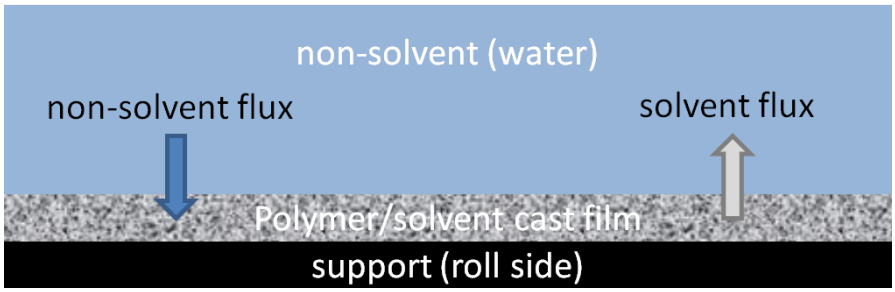

Fig. 7. Sketch of the cross section support - cast film and non-solvent, an exchange of the solution and water takes place until a thermodynamically stable state is reached; adapted from [22].

It is obvious that the miscibility gap will first be reached on the upper side of the cast film, leading to an asymmetric pore structure. A more detailed description of the diffusion aspects determining the fluxes of solvent and non-solvent can be found in [22]. The asymmetric structure can be determined by factors like the temperature on the roll side and upper side (air side) prior to immersion in the coagulation bath. Membrane formation can also be influenced by other parameters such as bath temperature, additional components in the cast solution or the choice of polymer and non-solvent.

After immersion in the coagulation bath the finished membrane is passed through a series of rolls to wash out residual solvents. In the last step the membrane quality is checked using optical methods.

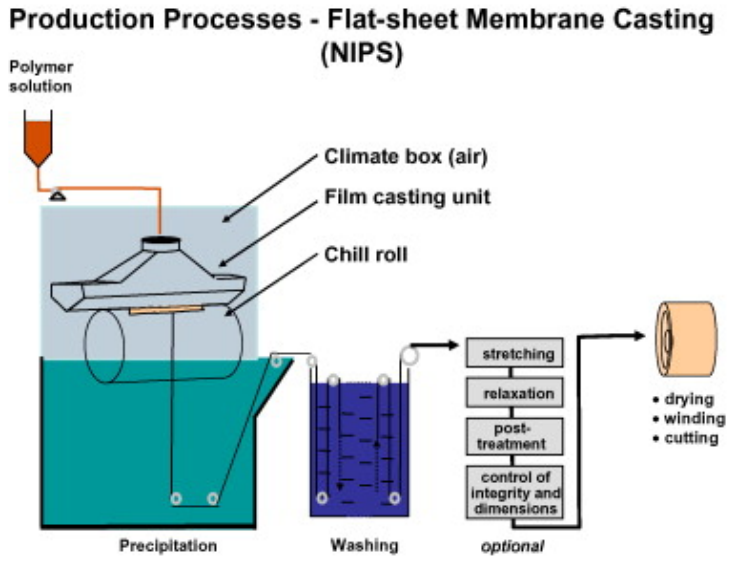

Fig. 8. Sketch of the NIPS process; adapted from [24].

2.2 **Membrane characterization** [22]

The dramatic rise in demand for separation over the last decades has resulted in increasingly complex separation membranes. A wide range of different membranes is currently in use for different separation tasks. The membranes can be generally classified into two groups: *porous* and *non-porous membranes*. This work will concentrate on porous membranes. As outlined in section 2.1, various production parameters can affect the membrane structure. One main task of membrane characterization is to verify the reproducibility of the decisive membrane parameters. The characterization method to be used depends on the pore size, which can range from nano-porous to macro-porous. Different types of characterization methods for porous membranes can be distinguished:

- Structure related parameters:

  Pore size and pore size distribution
  Membrane thickness
  Symmetric or asymmetric cross-section
  Position of the separation layer

- Permeability related parameters:

  Retention rates
  Molecular weight cut off (MWCO)
  Water flux

- Moreover parameters of the membrane material itself can be important:

  Organic, inorganic
  Hydrophobic or hydrophilic

The membrane characterization methods generally used are described in the following.

2.2.1 **Basics** [22]

The main obvious features of a porous membrane are the pores themselves. However, the pore size and the pore size distribution do not fully characterize the membrane structure. The pore shape or pore geometry are also very important factors which are ignored in many theoretical models. For example, using the Hagen-Poiseuille equation calculating the volume flow Q though a membrane, cylindrically formed pores with radius r are assumed.

$$Q = \frac{V}{t} = \frac{r^4 \pi}{8 \eta l} (P_A - P_B), \qquad \textbf{(5)}$$

with; η the liquid viscosity, l the membrane thickness and P_A, P_B the applied pressure.

In most cases real pores are not cylindrically shaped. The membranes studied in this work have a more or less sponge-like structure. The calculated membrane parameters will thus differ from the real ones. Nevertheless, a combination of well defined characterization methods can give at least partial information about the membrane morphology.

2.2.2 Bubble point method [22]

A commonly used method for obtaining the maximum pore diameters of a membrane is the so called bubble point method. Fig. 9 shows the principle: a gas (air) is pressed through an already wetted membrane. The pressure is increased until bubbles appear at the opposite side. The maximum pressure difference is achieved when the diameter of the meniscus in the largest pore has the diameter of that pore. In this case the contact angle between membrane and liquid is zero (Fig. 9). The applied pressure difference is measured and the radius of the largest pore can be calculated using the Young-Laplace equation:

$$r_p = \frac{2\gamma}{P_A - P_B} cos\,\theta, \qquad \textbf{(6)}$$

with γ the surface tension at the liquid / air interface, and θ the contact angle membrane - liquid. At maximum pressure $\cos\theta = 1$.

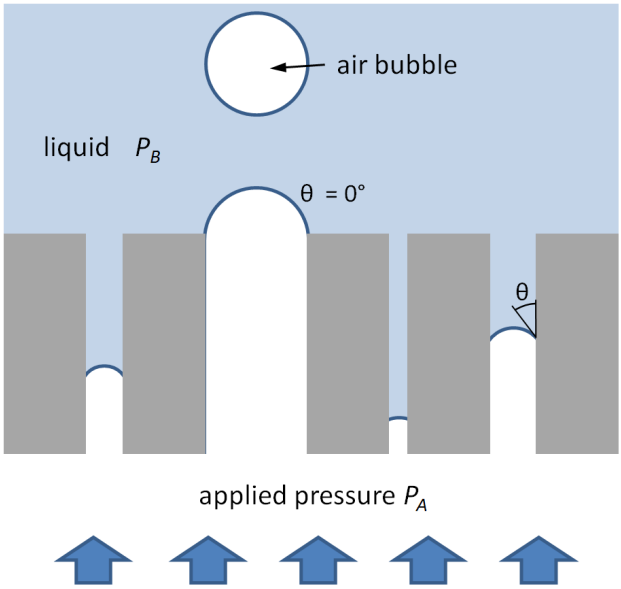

Fig. 9. Principle of the bubble point method: a gas is pressed through a wetted membrane until bubbles appear at the opposite side; adapted from [22].

This method measures the largest active pores and has thus become one of the standard techniques for membrane manufacturers to characterize their microfiltration membranes. Using liquids other than water will change both the surface tension and the contact angle, but the pore radii should remain unchanged, independent of the liquid used for the measurement. Nevertheless, different liquids (water, ethanol, methanol etc.) lead to different pore radii. The main reason for this are differences in the wettability of the membranes. Moreover other effects like variations in the pressure ramp or the stretching of the membrane material during the test can lead to different results.

The classical bubble point method can be modified to obtain more information about the pore size distribution of a given membrane. The so called wet-dry flow method first measures the gas flow through a dry membrane. As expected, the gas flow increases linearly with pressure. Subsequently the membrane is wetted and the gas flow is again measured as a function of the pressure applied (Fig. 10a). At low pressures the gas flux is low - all pores are still filled with water. At a certain minimal pressure the largest pores will be opened and the flux increases. A further increase in pressure will also open smaller pores. At very high pressures the gas flow should reach the flow of the dry membrane- if this is not the case small pores are still filled with water. Extensions of the bubble point method are the mercury intrusion and permeability methods, which are discussed below.

2.2.3 **Mercury intrusion method** [22]

The principle of the mercury intrusion method is pressing mercury into the dry membrane. The mercury volume is measured as a function of the pressure applied (Fig. 10b). Again, the relationship between the applied pressure and the pore size is given by the Young-Laplace equation (6). The mercury volume can be measured very precisely and so the results are also very accurate. However, small pores need very high pressures to be filled with mercury, which can cause damage to the pore structure.

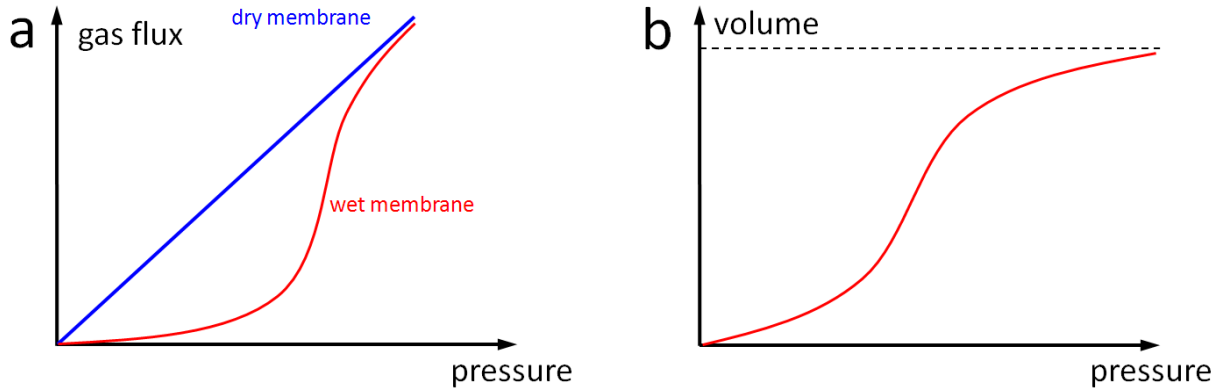

Fig. 10. a: Gas flux as a function of the applied pressure using the modified bubble point method (wet-dry method); b: cumulative volume in as a function of the pressure applied using the mercury intrusion method; adapted from [22].

2.2.4 **Permeability method** [22]

This method involves pressing a liquid (in most cases water) through a membrane at a constant pressure and measuring water flux. The water flux increases with pressure - see also equation (5). Although many membranes are hydrophobic and are not instantly wetted by water, however their pore size can also be measured using water as a penetrating liquid. At a certain pressure large pores become permeable, while small pores still remain impermeable. The minimum pressure is determined by the membrane material (contact angle), the surface tension and the pore size distribution. Similar to the method discussed in section 2.2.2, all small pores become permeable at sufficiently high pressures. A further increase in pressure causes the water flux to increase linearly. The resulting curve (water flux as a function of the pressure applied) is similar to the curve shown in Fig. 10a.

2.2.5 **Porosimetry** [28]

The volume porosity is determined by measuring the membrane weight in its dry as well as in its wet state. A well penetrating liquid with a low vapor pressure (e.g. silicon oil) is used to wet the (hydrophilic) membrane. The membrane is then centrifuged to get rid of the excess liquid. The rotation velocity of the centrifuge must be chosen carefully so that only the excess liquid will be ejected from the membrane surface, while the liquid still remains in the pore structure. The wet and dry membrane weight determines the volume porosity as follows:

$$p_V = \frac{\frac{m_1 - m_2}{\rho_{oil}}}{\frac{m_1 - m_2}{\rho_{oil}} - \frac{m_2}{\rho_{poly}}} \quad , \qquad (7)$$

with m_1 the mass of the wet membrane, m_2 the mass of the dry membrane, ρ_{oil} the density of the test liquid and ρ_{poly} the density of the membrane polymer.

Incorrect results can occur when the liquid did not wet the membrane completely or when the rotation velocity was too high or too low. The number of tests must thus be large enough to obtain statistically significant results. In any case the membrane must be hydrophilic, so that the liquid penetrate into the pore structure without pressure applying.

2.2.6 Bacteria retention method or bacteria-challenge-test [20]

As mentioned in the motivation part, bacteria retention is essential, especially when the membrane is used for sterile filtration. Membrane characterization is thus also possible using bacteria. The membrane will be pressurized with a suspension containing the specific bacteria culture. The standard test method is described in ASTM F838 - 05 as well as in DIN 58355 [29]. The bacteria Pseudomonas is used for membranes with a pore size of 0.2 µm and Serratia marcescens for a pore size of 0.45 µm. However, these tests give only additional information about the effectiveness of the membrane concerning sterile filtration, but not about the pore size distribution or other structural parameters.

2.2.7 Trans-membrane flow (TMF) measurements [29]

TMF measurements involve pumping a liquid through the membrane at a specific pressure. It is essential that the pressure difference is constant during the experiment. The volume of the liquid flowing through the membrane during a preset time is measured to calculate TMF as follows:

$$q = \frac{V}{t\,A\,\Delta P}, \qquad \textbf{(8)}$$

with V the volume of the liquid, A the membrane area and ΔP the pressure difference applied.

The test is performed on an already wetted membrane. Distilled water is used for hydrophilic membranes and organic solutions for hydrophobic ones. In any case it must be guaranteed that the filtration equipment, especially the membrane holder, does not influence membrane resistance.

Beyond the methods presented above, electron microscopy is one of the most widely used methods to get a direct impression of the membrane structure, as will be discussed in the next section.

2.3 **Electron microscopy** [30-32]

The simplest way to obtain an image of the surface structure of a membrane in sufficient detail (e.g. a microfiltration membrane) is to use a conventional light microscope. In most cases the pore size of at least the largest pores as well as the main morphological properties (sponge-like or tube-shaped pores, flat or rough surface) of the membrane and other key parameters such as mean membrane thickness and asymmetry can be determined. However, the membrane separation layer - which mainly determines the filtration properties - is often structured in the nm range. Conventional light microscopy can thus not be used for a comprehensive analysis as its resolution is limited by the wavelength of visible light. Particles like electrons, which can have much smaller wavelengths (de Broglie) than light, depending on their energy, enable even nano-structured samples to be analyzed:

$$\lambda = \frac{h}{m\,v}\,, \qquad \textbf{(9)}$$

with λ the wavelength of the electrons, h Planck´s constant, m the mass of the electron and v the electron velocity.

2.3.1 Scanning electron microscopy (SEM)

The main principle of the SEM involves scanning a fine focused electron beam across a sample surface and detecting electrons leaving the surface as a result of the interaction processes of the primary beam electrons with the sample. An electron gun generates an electron beam and subsequently the electrons are focused onto a small spot by magnetic lenses. To avoid damage to the cathode and scattering of the primary beam electrons on gas atoms, ultra high vacuum (UHV) is needed in the electron column and high vacuum (HV) in the sample chamber.

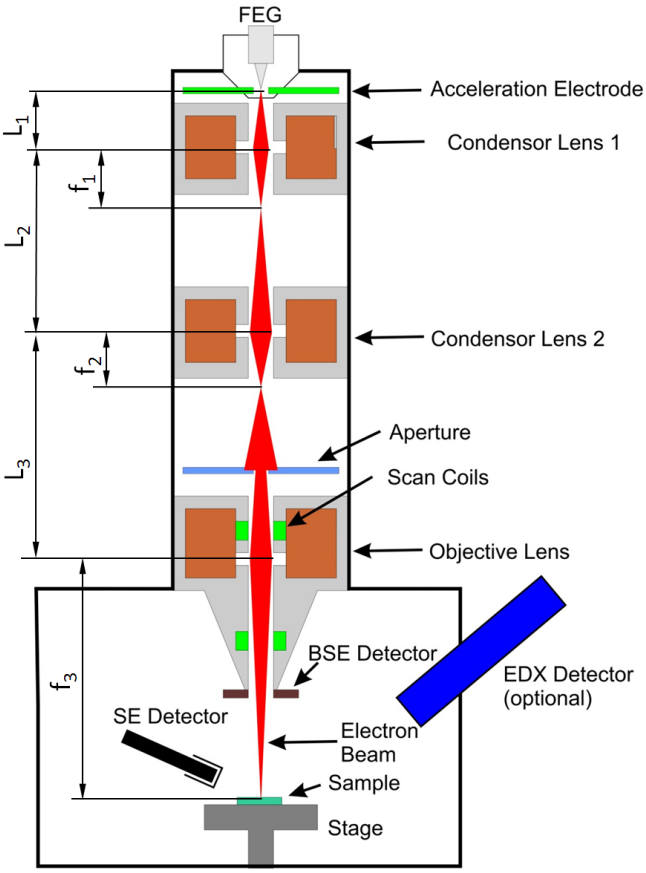

Fig. 11. Schematic of the SEM: a focused electron beam is scanned across the sample surface, electrons leaving the sample are detected and used for imaging.

Fig. 11 shows the principle of the SEM. The main components as well as the mode of operation of the instrument are described in detail in the following sections.

2.3.1.1 Electron sources [31,33]

Electrons can be emitted from an electrode by heating of the electrode (thermionic electron emission) or by applying a high electric field (field emission). A so called Schottky emitter combines both heating and the application of a modest electric field, with the latter lowering the work function but not enabling field emission. In any case, the electron beam should have high intensity (brightness), low energy spread and a small diameter of the virtual source.

A thermionic electron gun consists of a filament tip made from tungsten or LaB_6. A tungsten filament must be heated up to a temperature of approximately 2400 K to overcome the work function. The emitted electrons are accelerated by an electric field. The final electron energy is determined by the anode voltage. Most SEM´s operate with electron energies between 100 eV and 30 keV.

Field emission guns (FEGs) consist of a fine tungsten tip. A tip radius smaller than 100 nm and a field strength exceeding 10^7 V/cm enable field emission (tunneling of the electrons as indicated with a blue arrow in Fig. 12). In principle FEGs can be operated without heating. To avoid fluctuations in the beam current, however, FEGs are sometimes heated to 1000-1500 K. In any case the brightness of electron beams in microscopes equipped with a FEG is much higher and the energy spread much lower compared to those with thermionic sources. Also the virtual source is much smaller, so that a lower demagnification can be used.

This work was carried out using a Schottky emitter installed on the microscope (FEI Quanta 600 FEG). The electrode is made of W (100) coated with ZrO. As zirconium is electropositive the work function can be reduced from 4.5 to 2.8 eV. The work function is additionally lowered by the application of an electric field. As the tip radius is around 1 µm the field strength is too low for tunneling of the electrons.

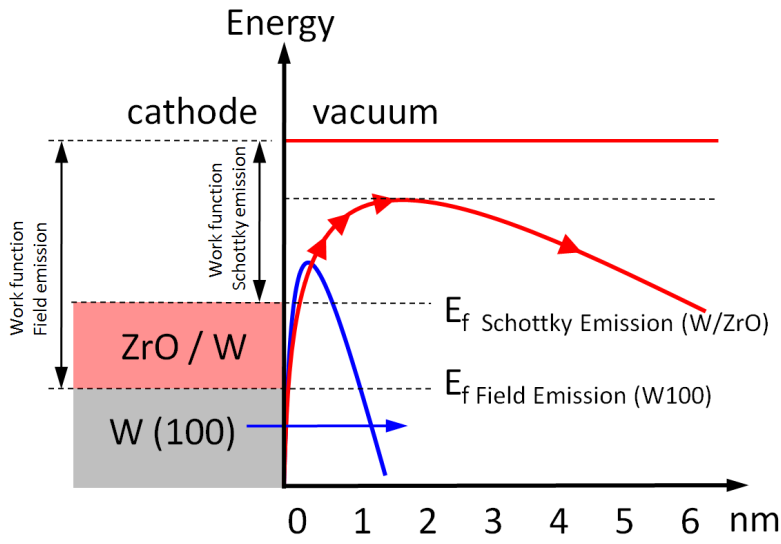

Fig. 12. Energy level diagram for Schottky emission and for field emission; adapted from [33].

2.3.1.2 Electron optics [31]

The electron optics is responsible for the demagnification of the virtual source and the focusing of the electrons onto a small spot on the specimen surface (electron probe). Electrons are deflected by magnetic fields due to their electrical charge:

$$\boldsymbol{F} = -e(\boldsymbol{v}\ x\ \boldsymbol{B}) \quad \textit{(Lorentz Force).} \qquad \textbf{(10)}$$

An axial magnetic field with rotational symmetry is used for electron focusing. The magnetic field is created by specially formed electron magnets. The coil current determines the strength of the magnetic field ***B*** and, as a consequence, the focus length of the lens:

$$f \propto \frac{1}{B^2} \ . \qquad \textbf{(11)}$$

As can be seen from (11), the focal length can only be positive. Magnetic dispersing lenses thus do not exist. In many cases the electron column consists of two condenser lenses and a final objective lens. Assuming the crossover image is formed at large distances in front of the next lens ($L_2 \gg f_1$ and $L_3 \gg f_2$ respectively) the demagnification of the source can be estimated by [31]:

$$d_0 = \frac{f_1 f_2 f_3}{L_1 L_2 L_3} d_c = mag \cdot d_c \ , \qquad \textbf{(12)}$$

with d_c the diameter of the virtual source, d_0 the spot diameter, L_1-L_3 and f_1-f_3 the distances shown in Fig. 11.

The demagnification is in the range of 1/5000 for thermionic emitters. As FEG´s can produce much smaller (virtual) sources (in the range of 10 nm) no such strong demagnification is necessary and instruments equipped with such an emitter can thus also be operated with one or two lenses. The last probe forming lens (objective lens) also contains the scan coils which deflect the electron beam, enabling scanning across the specimen surface (Fig. 11). The magnification is determined as the length of the area scanned by the electron beam and the width of the image at the output medium (screen):

$$mag = \frac{width\ of\ the\ image\ at\ the\ output\ medium}{width\ of\ the\ scanned\ area}$$

2.3.1.3 Sample stage and specimen chamber

The specimen chamber is usually located below the electron column. Additional detectors as well as the sample stage, which enables precise positioning of the sample, are attached to the chamber. The size of the specimen chamber and the sample stage itself is adapted for the specific use of the microscope. The present work was carried out using an instrument with a large specimen chamber to be able to mount additional experimental setups on the sample stage. In extreme cases the door of the specimen chamber, including the sample stage, can be removed and replaced by another door with additional large equipment, for example an automated ultramicrotome (see section 3.2.2), directly attached to it. In any case a highly flexible chamber system is needed to perform special experiments requiring additional components.

2.3.1.4 Interaction with the specimen

The primary electron beam interacts with the specimen, causing both elastic and inelastic scattering of the primary electrons. For example, the interaction of the primary electrons with the screened Coulomb field of the atomic nuclei can cause both a change in direction of the electrons without energy loss (elastic scattering) and a deceleration of the electrons. In case of large angle scattering these electrons can leave the sample as backscattered electrons (BSEs).

On the other hand the primary electrons can lead to ionization of the specimen atoms. Part of the primary electron energy is transferred to the target atom and as a consequence secondary electrons (SEs) can be emitted (inelastic scattering).

In any case the primary electron beam leads to an interaction volume, where all kinds of scattering events can occur. Kanaya et *al*. [34] give an estimation of the radius of the interaction volume:

$$R_{KO} = \frac{0.0276\, A_W}{Z^{0.89}\rho} E_0^{1.67}\ [\mu m], \qquad \textbf{(13)}$$

with Z the atomic number, E_0 the primary electron energy [keV], A_W the Atomic weight [g/mol] and ρ the sample density [g/cm³].

Low electron energies require modification of the equation. The most important fact for the present work is the dependency of the radius on the primary electron energy: $R \propto E_0^{1.67}$. An increase in E_0 leads to much greater interaction volumes and, as a consequence, to an increase in the information depth. Therefore, if surface sensitivity is required, as is the case for *in situ* ultramicrotomy in the ESEM (see section 3.2), the electron energy must be as low as possible. The probability of an elastic scattering event is described by the cross-section σ. In a rough approximation the classical Rutherford model [31] can be used:

$$\sigma \propto \frac{Z^2}{E_0^2} cot^2\left(\frac{\varphi}{2}\right), \qquad \textbf{(14)}$$

with φ the scattering angle.

The increasing probability of elastic scattering events with higher atomic number is due to the stronger Coulomb interaction because of the higher positive charge of the nucleus. Conversely, the scattering probability decreases with higher electron energies. Other theoretical models like Mott [35] include quantum mechanical aspects such as the electron spin as well as the fact that the atomic nucleus is screened by the electron cloud. This model leads to better results in the simulation of the cross-sections.

Monte Carlo simulations are currently used for the calculation of the interaction volume and the escape depth of the backscattered electrons [31]. Fig. 13a shows a Monte Carlo simulation of the interaction of the primary electrons with polyethersulfone (density 1.4 g/cm³ [36]), created with the simulation software CASINO [37]. The primary electron energy was set to 4 keV and the Mott model was chosen for the calculation of the scattering cross-section. The escape depth of the BSEs is shown in Fig. 13b. The maximum penetration depth of those primary electrons leaving as BSEs is around 100 nm. This depth determines the maximum slice thickness in connection with *in situ* ultramicrotomy for 3D reconstruction of the sample (see section 3.2). In the present work, however, a slice thickness of 50 nm was used because BSEs coming from a greater depth also lose more energy and thus do not provide a sufficient signal at the detector. The energy loss of the primary electrons traveling within the specimen are described theoretically by the Bethe stopping power [30]:

$$BSP = \frac{dE}{dx} = -\,7.85\ \cdot 10^4 \frac{Z}{A_W}\frac{\rho}{E_m}\ ln\left(1.166\frac{E_m}{J}\right)\ [keV/cm], \qquad \textbf{(15)}$$

where E_m is the mean energy lost along the distance dx [keV], J the ionization potential [keV], Z and A_W the atomic number and the atomic weight [g/mol], respectively.

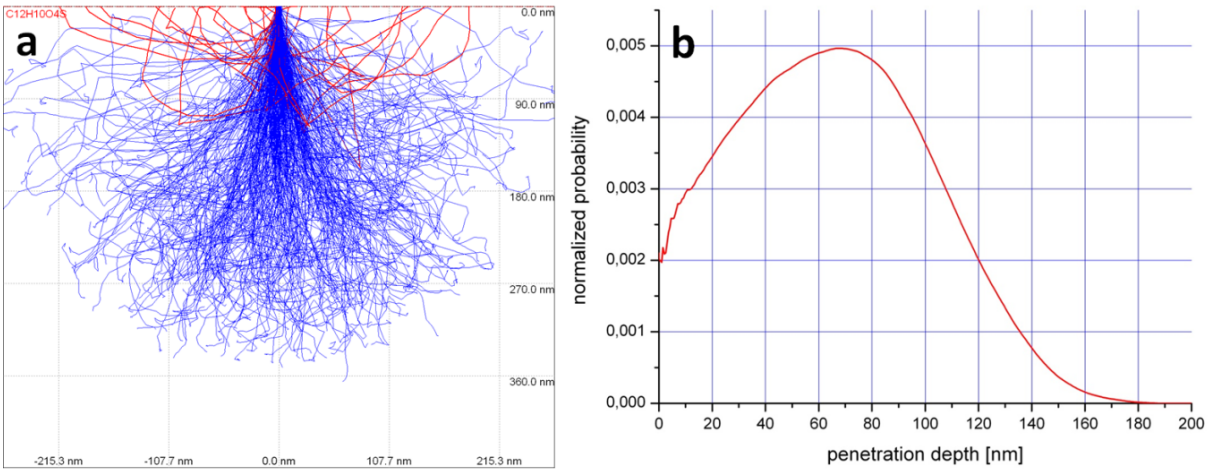

Fig. 13. Monte Carlo simulation of the interaction of electrons with polyethersulfone (density 1.4 g/cm³); primary electron energy: 4 keV, Mott model for scattering. a: electron paths, with the backscattered electrons (BSE) in red; b: normalized probability of the BSEs as a function of the penetration depth.

The BSE coefficient describes the ratio of the primary electrons which leave the sample as BSEs as follows:

$$\eta_{BSE} = \frac{n_{BSE}}{n_{PE}}, \qquad \textbf{(16)}$$

with n_{BSE} the number of backscattered electrons and n_{PE} the number of primary electrons.

One of the most important properties of the BSEs is the dependency of η_{BSE} on the atomic number of the sample atoms, as shown in Fig. 14a. This contrast mechanism is known as “material contrast” or “compositional contrast” [30], the curve in Fig. 14a can be fitted with a polynomial of third order. Equation (17) gives the polynomial with the respective constants for incident beam energy of 20 keV [38]:

$$\eta_{BSE} = -0.0254 + 0.016 \cdot Z - 1.86 \cdot 10^{-4} \cdot Z^2 + 8.3 \cdot 10^{-7} \cdot Z^3. \qquad \textbf{(17)}$$

η_{BSE} is nearly independent of E_0 in the range of 5-50 keV [30]. This unexpected result is due to the fact that interaction range and stopping power are competitive effects. As the range of the interaction volume increases at the power of 1.67, the stopping power is the inverse of the primary electron energy E_0.

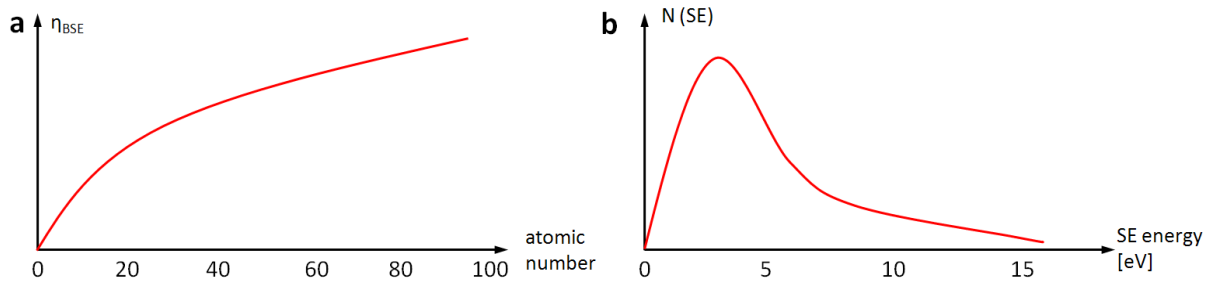

Fig. 14. a: BSE coefficient as a function of the atomic number; b: Number of SEs as a function of their energy. Most SEs have an electron energy below 5 eV.

Secondary electrons (SE) are the result of inelastic scattering. All emitted electrons with energies below 50 eV are defined as SEs, but most secondary electrons have an energy below 5 eV (see Fig. 14b). The most important property of SEs is their small escape depth, especially for metallic samples and the resulting high spatial resolution. The probability for a generated SE in a sample depth z to reach the sample surface is described by:

$$p_{rop} = e^{-\frac{z}{\lambda_f}}, \qquad \textbf{(18)}$$

where λ_f is the mean free path length of the SE within the sample. This length is around 1 nm for metallic samples and around 5 - 20 nm for insulators [39]. The short free path length for SEs in metallic materials is due to their strong scattering at the free electrons (electron gas). Similar to the BSE coefficient a SE coefficient (δ) is introduced:

$$\delta = \frac{n_{SE}}{n_{PE}}, \qquad \textbf{(19)}$$

with n_{SE} the number of secondary electrons leaving the sample and n_{PE} the number of primary electrons. As δ is nearly independent of the atomic number Z, but dependent on the tilt angle of the respective surface region SEs can be used for topographic imaging of the specimen surface.

The ratio of the total number of emitted electrons in relation to the number of primary electrons is plotted in Fig. 15 as a function of the primary electron energy. As can be seen in Fig. 15 there exist two energies at which the number of primary electrons penetrating the sample and the number of electrons leaving the sample (η_{BSE}+δ) are equal. But only E_2 is a stable point of equilibrium.

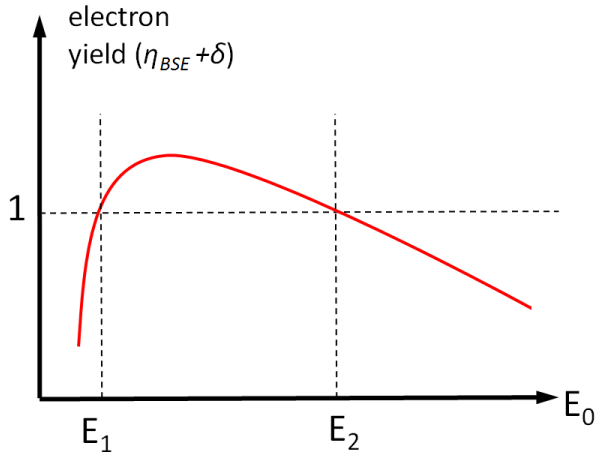

Fig. 15. Total electron yield as a function of the energy of the primary electrons.

This means that no charge is accumulated on the sample surface of insulators at an electron energy E_2. At other electron energies charging on the specimen surface will occur and lead to imaging artifacts. Therefore it is essential to coat non-conductive samples with a thin conductive layer of carbon or metal such as platinum or gold.

In many cases sample coating is not possible or not wanted, however, for example in *in situ* tests, where the sample surface might be modified. To overcome this problem and enable the investigation of non-conductive samples such as PES membranes in their native state, low vacuum is used inside the sample chamber instead of high vacuum. The residual gas atmosphere enables the compensation of the negative surface charges, while on the other hand the investigation of wet systems is possible using water vapor as chamber (imaging) gas. The following sections describe the basic concepts of image formation in the VPSEM (Variable Pressure SEM) or ESEM (Environmental SEM).

2.3.2 Environmental scanning electron microscope (ESEM) [32]

The main idea of the ESEM is to use gas inside the sample chamber at pressures between 0.1 and 20 Torr. The so called imaging or chamber gas has two main functions:

- the interactions of electrons with the imaging gas molecules generate ions, which can reduce or even completely eliminate charge effects on the sample surface;
- amplification of the secondary electrons and thus enhancement of the detected signal; in this context the gas forms part of the detector which acts as a proportional counter.

Fig. 16 shows a sketch of the ionization processes inside the ESEM sample chamber. Generated SEs (green) are accelerated in the direction of the SE detector (GSED - gaseous secondary electron detector), which consists in principle of a positive biased ring electrode. On their way to the detector the SEs are able to ionize gas molecules, creating further electrons and thus an electron avalanche develops (orange). The electrons are finally collected at the detector and the signal obtained is amplified.

In case of a negatively charged specimen surface the resulting positive ions will be accelerated towards the sample surface and compensate the charging. The use of an imaging gas, however, makes image formation more complicated than in the conventional SEM. The corresponding effects will be discussed in section 2.3.2.3.

The two main signals (SEs and BSEs) and their detection are discussed in the following.

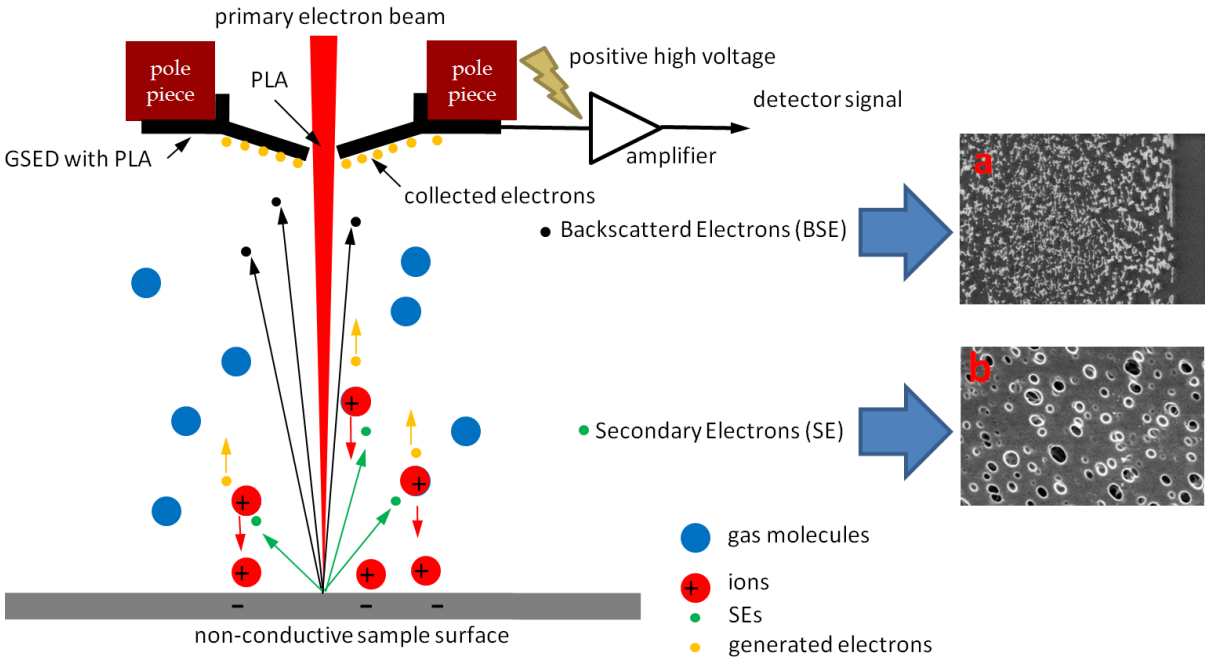

Fig. 16. Gas amplification in the ESEM chamber. a: BSE image of a membrane cross-section; b: SE image of a partly wet membrane surface.

2.3.2.1 Detectors

A GSED detector device is shown in Fig. 17a and b. The GSED has an integrated pressure limiting aperture (PLA), which is necessary to minimize the flow of gas from the specimen chamber to the microscope column. The GSED was used for imaging of the surface of the membranes and their cross-section in a partly wet state. The SE signal is reduced in areas where the surface pores are dry. This is due to shadowing of SEs which are generated inside the dry pores. Therefore dry pores appear dark.

No shadowing effects occur in wet areas of the membrane (on the surface or at pores filled with water), which therefore appear brighter (see also Fig. 16a). This contrast makes it possible to discriminate between dry and wet pores and calculate their numbers as a function of time - details will be discussed in sections 3.4.1 and 5.2.

On the other hand BSEs, which provide material contrast, were mainly used for image recording of the membrane cross-sections in combination with ultramicrotomy. A specially designed solid state detector with an active circular area of approximately 1 cm in diameter (see Fig. 17c) was used for the detection of the backscattered electrons. As the BSEs angular distribution has a maximum in the beam direction [31], the aperture of the detector through which the primary electron beam passes was kept extremely small (approx. 1 mm). This special geometry allows an efficient collection of most of the BSEs, especially at the small working distances used for *in situ* ultramicrotomy.

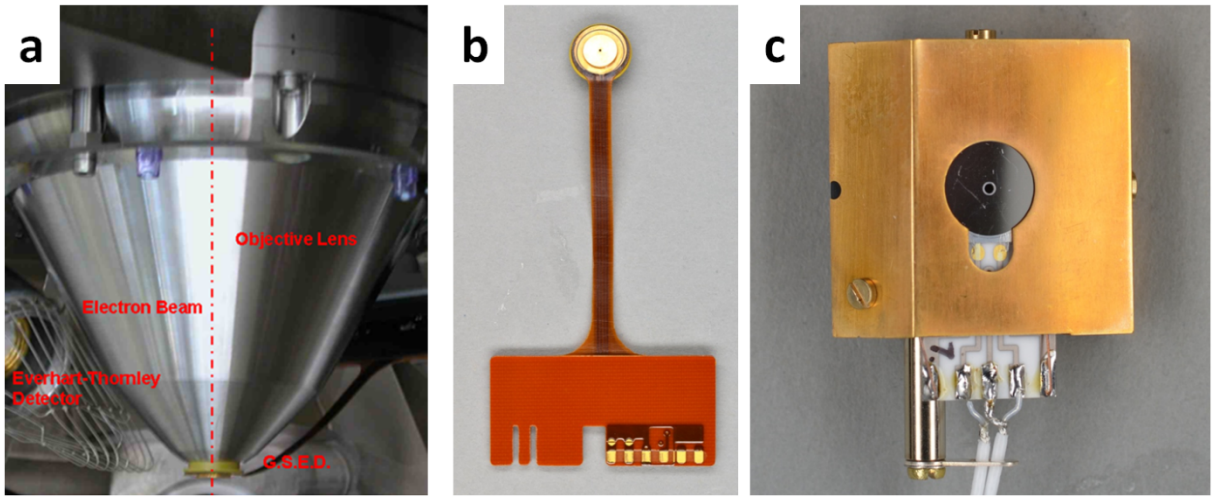

Fig. 17. The detectors used for imaging. a: final electron lens with GSED, b: GSE detector device with PLA, c: BSE detector.

2.3.2.2 The vacuum system

The electron column, especially the FEG, needs ultra high vacuum (UHV) for operation, whereas the vacuum in the specimen chamber can be as low as 20 Torr. As a consequence the electron column needs a differential pumping system for separating the two vacuum regions (see Fig. 18). The ultra high vacuum (UHV) regions are pumped by ion getter pumps (IGP), while the lower part of the electron column as well as the sample chamber itself are pumped by a turbo molecular pump (TMP) and rotary pump used as a pre-vacuum pump (PVP) [40]. The instrument used (Quanta 600 FEG) features three different vacuum modes:

- High vacuum mode (HV): $P < 10^{-4}$ Torr
- Low vacuum mode (LV): P up to 1 Torr
- ESEM mode: P up to 20 Torr

The ESEM can operate as a conventional SEM when using the high vacuum mode (HV). In this case the sample chamber is pumped with the TMP (path 1) as well as through the PLA (path 2) as shown in Fig. 18a. Using the LV mode (enabling pressures up to 1 Torr) the sample chamber is pumped via the PLA in the lower part of the electron column as shown in Fig. 18b. The lower part of the electron column is further divided into two parts, which are pumped by the PVP1 via path 3 and by the turbo molecular pump via path 2. This differential pumping system establishes a pressure gradient between the sample chamber and the UHV regions of the column. It should be noted that the sample chamber is not pumped via the “main” path 1. The main difference between the LV mode and the ESEM mode is the insertion of additional pressure limiting apertures. Increasing the pressure (e.g. from 1 to 6 Torr) can be done via the inlet valve and path 4 as shown in Fig. 18c. A pressure reduction (e.g. from 6 to

1 Torr) is achieved by opening valve ChEV to the PVP2 as shown in Fig. 18d (path 5). This means that by connecting PVP2 as an additional pump the pressure can be reduced quickly and accurately.

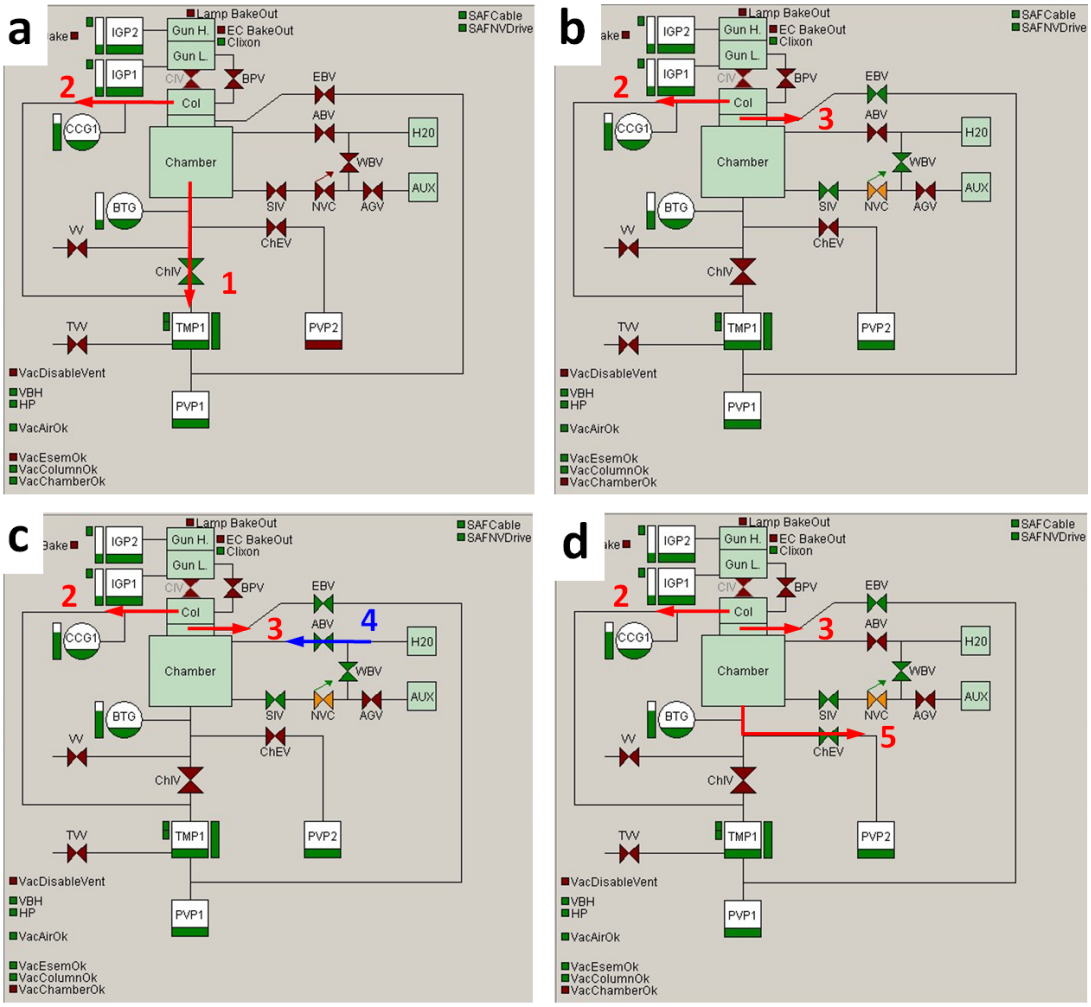

Fig. 18. ESEM vacuum system. a: HV mode, b: ESEM (or LV) mode at 1 Torr, c: ESEM mode increasing pressure from 1 to 6 Torr, d: ESEM mode, pumping from 6 Torr to 1 Torr. Red valves are closed, green are open; images from microscope user interface.

2.3.2.3 Image formation

The principle of the image formation in an ESEM has been sketched in section 2.3.2. In this section image formation is described in a more quantitative manner as can also be found in [32]. The main disadvantage of using an imaging gas is the fact that the primary beam electrons are scattered on their way to the sample surface. This effect, known as “skirt” effect, can dramatically reduce the signal / noise ratio of the imaging signal, while on the other hand ionization processes result in an increase in SEs (gas amplification) [41]. These two competitive processes strongly affect image formation.

First, the difference between working distance (WD) and beam gas path length (BGPL) will be explained, because these two parameters have a great impact on both electron scattering and gas amplification. The WD is defined as the distance between the impact point of the electron beam on the sample surface and the lower pole piece. The WD can be adjusted by moving the sample stage. The BGPL is the length of the primary electron beam within the imaging gas. Stokes [32] describes this length as GPL (gas path length) and defines it as the length between the final PLA and the sample surface. However, the (unwanted) interaction of the primary electrons with the gas atoms / molecules does not start at the last PLA, but also occurs in the region of the differential pumping system of the

microscope. Hence, the BGPL increases with increasing chamber pressure [42] and is thus longer than the WD. Gas amplification is not only caused by the SEs generated at the sample surface, but also by electrons generated by ionization of the primary electrons (PE) and BSEs [43]:

$$i_{amp} = i_{g(PE)} + i_{g(BSE)} + i_{g(SE)} \,. \qquad \textbf{(20)}$$

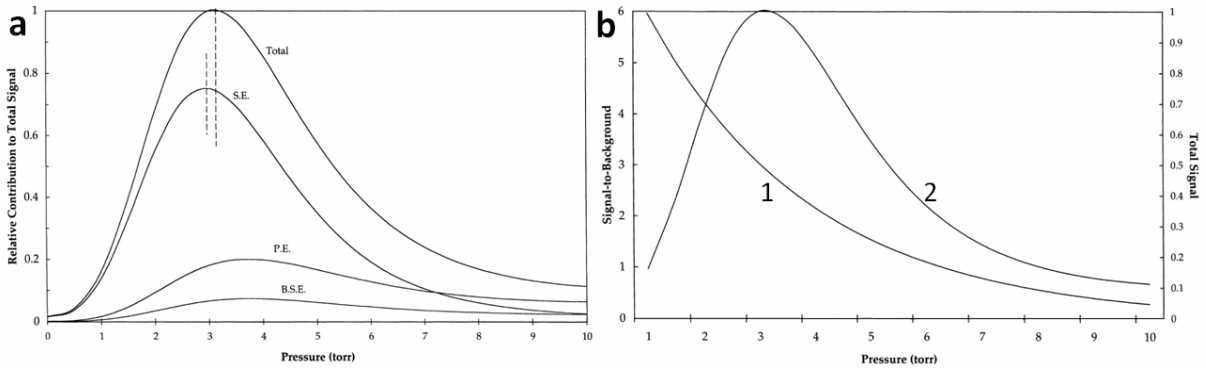

Fig. 19. a: contributions of the PE, BSE and SE to the detected signal as a function of the chamber pressure. b: signal-to-background ratio of the SE contribution as a function of the chamber pressure (1) and the total signal as shown in a (2); carbon substrate, anode voltage: 300 V, sample - detector distance: 7 mm; adapted from [43].

At higher pressures the contribution of the SEs decreases and as a consequence the total signal contributes significantly to material contrast (Fig. 19a), which means a decrease in the signal-to-background ratio concerning the SE signal (Fig. 19b). The behavior can be understood as follows: At very low pressure almost no ionization takes place due to the lack of sufficient gas molecules. At high pressures scattering occurs instead of ionization, which also means a decrease in the amplification of the SEs. This is due to the short mean free path length at high pressures (21), and the fact that the electrons are not able to build up sufficient energy for ionization between collisions.

$$\lambda_f = \frac{k_b\, T}{\sigma\, P}\,, \qquad \textbf{(21)}$$

with P the chamber pressure, T the gas temperature, σ the total cross-section and k_b Boltzmann's constant.

The ionization is described by Townsend´s first ionization coefficient [44]:

$$\alpha_T = aPe^{-\frac{b\,P\,l}{V_a}}\,, \qquad \textbf{(22)}$$

with $a = \frac{1}{\lambda_f}$ and $b = \frac{V_i}{\lambda_f}$ gas specific coefficients, P the chamber pressure, V_a the detector bias voltage, V_i the ionization energy of the gas and l the distance between sample surface and detector electrode. The expected amplification (gain) is given by [43,45]:

$$g = e^{\alpha_T l}\,. \qquad \textbf{(23)}$$

At a given detector voltage V_a electron amplification is determined by the product $P{\cdot}l$ [32,41]. Working with relatively high pressures (e.g. liquid water conditions) as described in section 2.3.2.4 allows reducing the distance between sample surface and detector electrode, which has a positive impact on PE scattering (skirt effect). The distance is limited, however, by the experimental setup (see section 3.3).

At low vacuum the PEs are generally scattered by the gas atoms / molecules and so the intensity of the still focused primary electron beam is reduced [42]:

$$i_p = i_0 \cdot e^{-\frac{\sigma P BGPL}{k_B T}} = i_0 \cdot e^{-n}, \qquad \textbf{(24)}$$

with $n = \frac{BGPL}{\lambda_f}$ the average number of collisions per electron, i_0 the primary beam current and i_p the beam current consisting of the unscattered electrons. The percentage of scattered electrons can be reduced by increasing the electron energy as this results in a decrease in the total cross-section σ [46]:

$$\sigma = a\, E_0^{-b}, \qquad \textbf{(25)}$$

with $a = 1.568 \cdot 1^{-20}$ $[m^2/keV]$ and $b = 0.864$, gas specific parameters experimentally determined by Rattenberger [42].

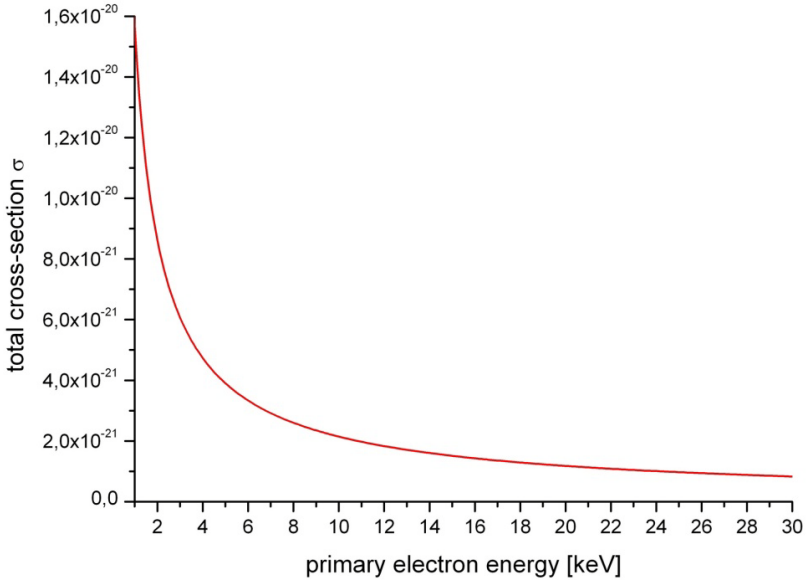

Fig. 20: Total cross-section of water vapor as a function of the primary electron energy, calculated with (25) using the values from [42].

The differential cross-section gives information about the angles at which the PEs are scattered on their way through the imaging gas and thus about the skirt effect. The main result of analytical and numerical analysis presented in [47] is the fact that the unscattered PE fraction is focused in a spot of a size comparable to that obtained in the high vacuum mode. Thus there is no loss of resolution, but a decrease in the signal / noise ratio. The knowledge of the skirt radius is important in connection with x-ray spectrometry [32].

2.3.2.4 Imaging at liquid water conditions

Referring to the previous section modification of the following parameters can help to reduce scattering of the primary electrons [32]:

- Decreasing the chamber pressure
- Increasing the primary electron beam energy
- Decreasing the BGPL (by decreasing the WD)

Yet observation of samples in their wet state is only possible using water vapor at pressures higher than the dew point at the respective temperature (see phase diagram of water shown in Fig. 36). Moreover, organic samples like PES membranes are sensitive to radiation damage, and the higher the electron energy the more severe the damage. The distance between the sample surface and the detector is limited to approximately 7 mm due to the experimental setup. In view of these restrictions the parameters mentioned above cannot be changed arbitrarily, and this will also limit image quality.

As already explained in previous sections the electron energy should be kept as low as possible. But at high pressures a high electron energy is desirable to minimize skirting. Fig. 21 presents images recorded at different electron energies. They show that an electron energy of 7 keV is a good compromise, providing sufficiently low noise level and sufficient contrast for subsequent image processing.

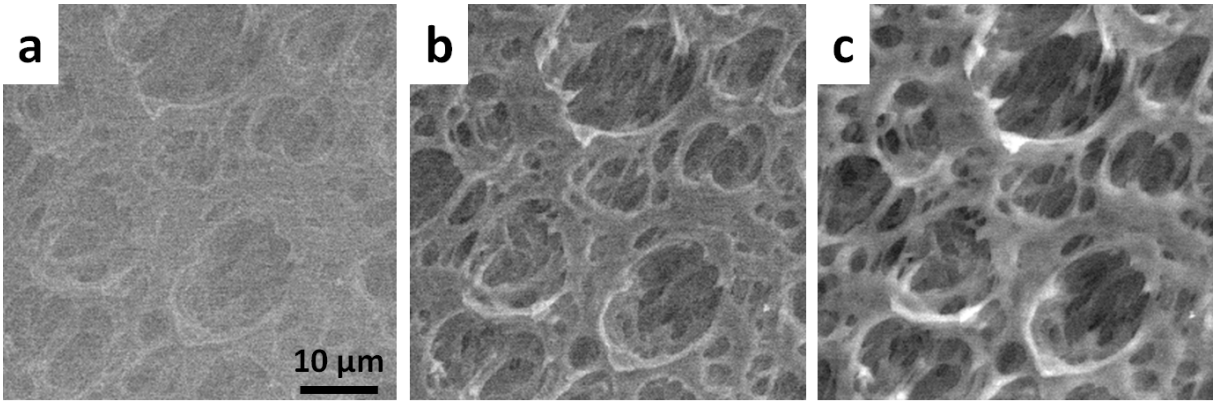

Fig. 21. Noise in images recorded at different primary electron energies. a: electron energy = 5 keV; b: electron energy = 7 keV; c: electron energy = 10 keV. All images were recorded at a chamber pressure of 6 Torr and a WD of 7 mm.

One must also bear in mind that an increase in the electron energy also increases the penetration depth of the PEs. But the penetration depth of the electrons should not be larger than the thickness of the pore walls. Otherwise one image can contain information about several pore layers, which is especially undesirable when performing a 3D reconstruction of the membrane structure from such images.

2.3.2.5 Radiation damage

One of the main effects limiting the maximum possible magnification and thus the minimum size of pores that can be imaged is specimen damage caused by irradiation of the specimen with electrons. As the magnification increases, the energy of the PEs is deposited into smaller volume fractions. Coating can help to protect the sample from beam damage, but is not possible using *in situ* ultramicrotomy. If the behavior of the membranes in a wet environment is investigated coating will definitely affect the results because it substantially changes the interaction between membrane and water.

A further problem using high electron energies is the change in the chemical properties of the irradiated pore surfaces, which could also change the hydrophilicity of the membrane. Beam damage is enhanced in the presence of water at the irradiated specimen surface, as free radicals are formed which additionally attack the polymer [48]. The dominant reactive species is the hydroxyl (O – H) radical. Royall et *al*. show that the combination of low beam energy and high beam current causes less specimen damage than the combination of low beam current and high electron energy [48].

A detailed discussion concerning beam damage to the materials used in this work can be found in sections 4.5 and 5.5.

3 Experimental

3.1 Morphology and preparation of microfiltration PES membranes

The mean pore sizes of the highly asymmetric membranes used for the investigation are shown in Table 1. According to the type of asymmetry and the mean pore size the membranes were named either MicroPES® or DuraPES® with suffixes 2F or 200 (mean pore size: 200 nm); 4F or 450 (mean pore size 450 nm) etc., respectively. Table 1 gives an overview of some of the most important technical parameters. The membranes were kindly provided by the companies Membrana (MicroPES® and DuraPES®) and Sartorius (Type 15406). The Sartorius type 15406 was chosen for comparative studies due to the fact that it has nearly the same nominal pore size as the MicroPES®4F and DuraPES®450 but a less asymmetric cross-section.

Table 1: Technical data of the membranes investigated; data from [49,50].

Membrane type	Nominal pore size [µm]	Thickness [µm]	Bubble point [bar]	TMF (water 25°C) [ml/(min cm² bar)]	Charge number
MicroPES®2F	0.20	110 ± 10	4.30 ± 0.25	35	08189 8078 04
MicroPES®4F	0.40	110 ± 10	3.00 ± 0.25	60	07229 8021 13
MicroPES®6F	0.60	110 ± 10	1.90 ± 0.42	90	08046 8054 07
DuraPES®200	0.20	140 ± 10	4.80 ± 0.5	45	08288 80093 17
DuraPES®450	0.45	140 ± 10	3.45 ± 0.35	75	08280 8092 15
DuraPES®600	0.60	140 ± 10	2.25 ± 0.35	160	8092 10099 18 002
DuraPES®600 (old version)	0.60	140 ± 10	2.25 ± 0.35	160	07266 8089 18
Sartorius 15406	0.45	150	2.6	46	

3.1.1 Morphology of the membrane surfaces

Fig. 22 and Fig. 23 show that the surface morphologies of the individual membranes listed in Table 1 differ substantially. The Membrana MicroPES® membranes are characterized by large pores and a low pore density on the air side and smaller pores and a higher pore density on the roll side. The situation is vice versa for the Sartorius 15406 membrane (Fig. 22 right). The pore size on the air side increases from the MicroPES®2F (0.2 µm) to the MicroPES®6F (0.6 µm). Huge differences in pore size between air and roll side can be observed for the DuraPES® types. Fig. 23 (second and third row) shows images of both surfaces of the DuraPES® membranes. Images of the roll side were also recorded at a lower magnification to get a better impression of pore morphology (Fig. 23 first row).

The pore size on the air side increases from the DuraPES®200 (0.2 µm) to the DuraPES®600 (0.6 µm). The mean pore size on the roll side seems to be approximately the same for all membranes. However a special characteristic is the subdivision of the large pores and the many small pores within the large ones. The resulting bimodal pore size distribution is dominated by the small pores and leads to a very special drying behavior of individual pores of different sizes as will be discussed in section 5.2.

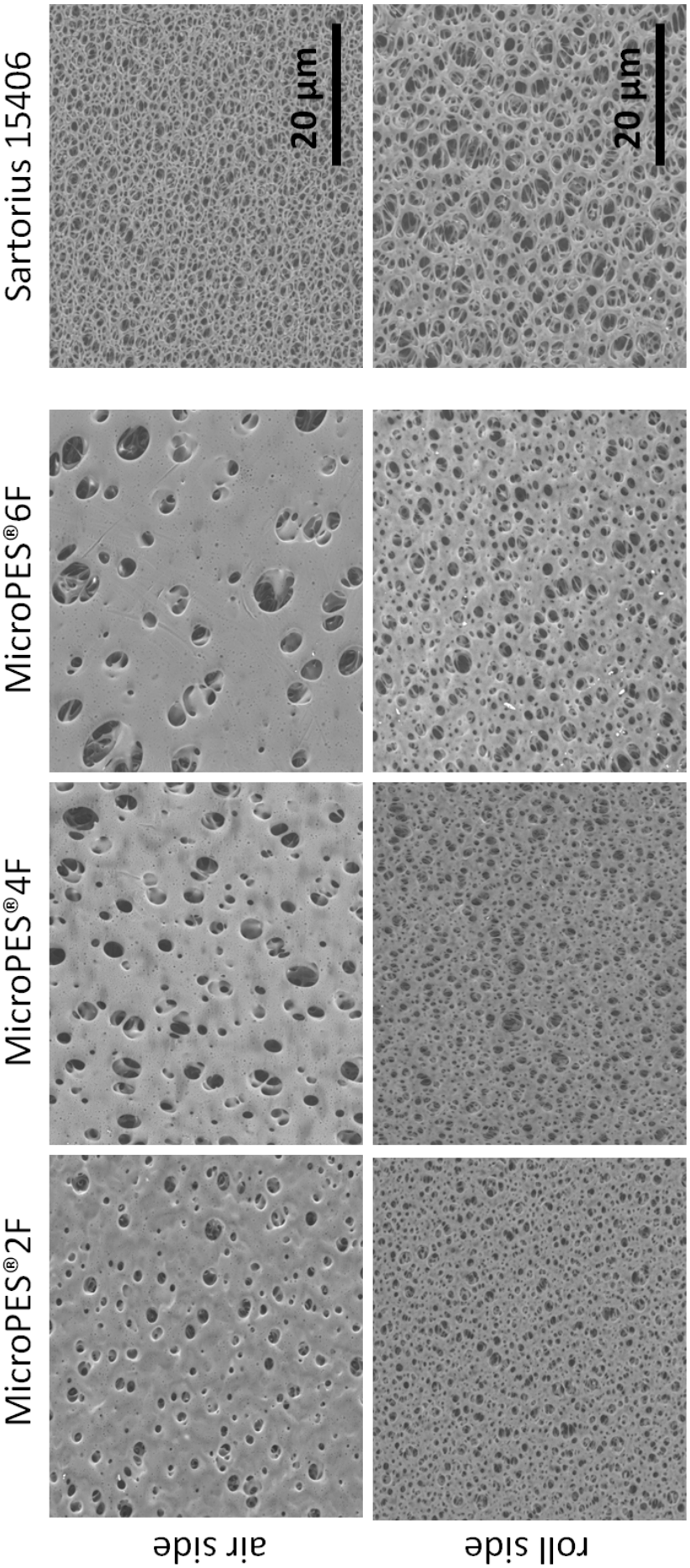

Fig. 22. SEM images of the surface morphology of the roll side and the air side of the Membrana MicroPES® and Sartorius 15406 membranes. (low vacuum mode, P = 0.5 Torr, electron energy = 5 keV)

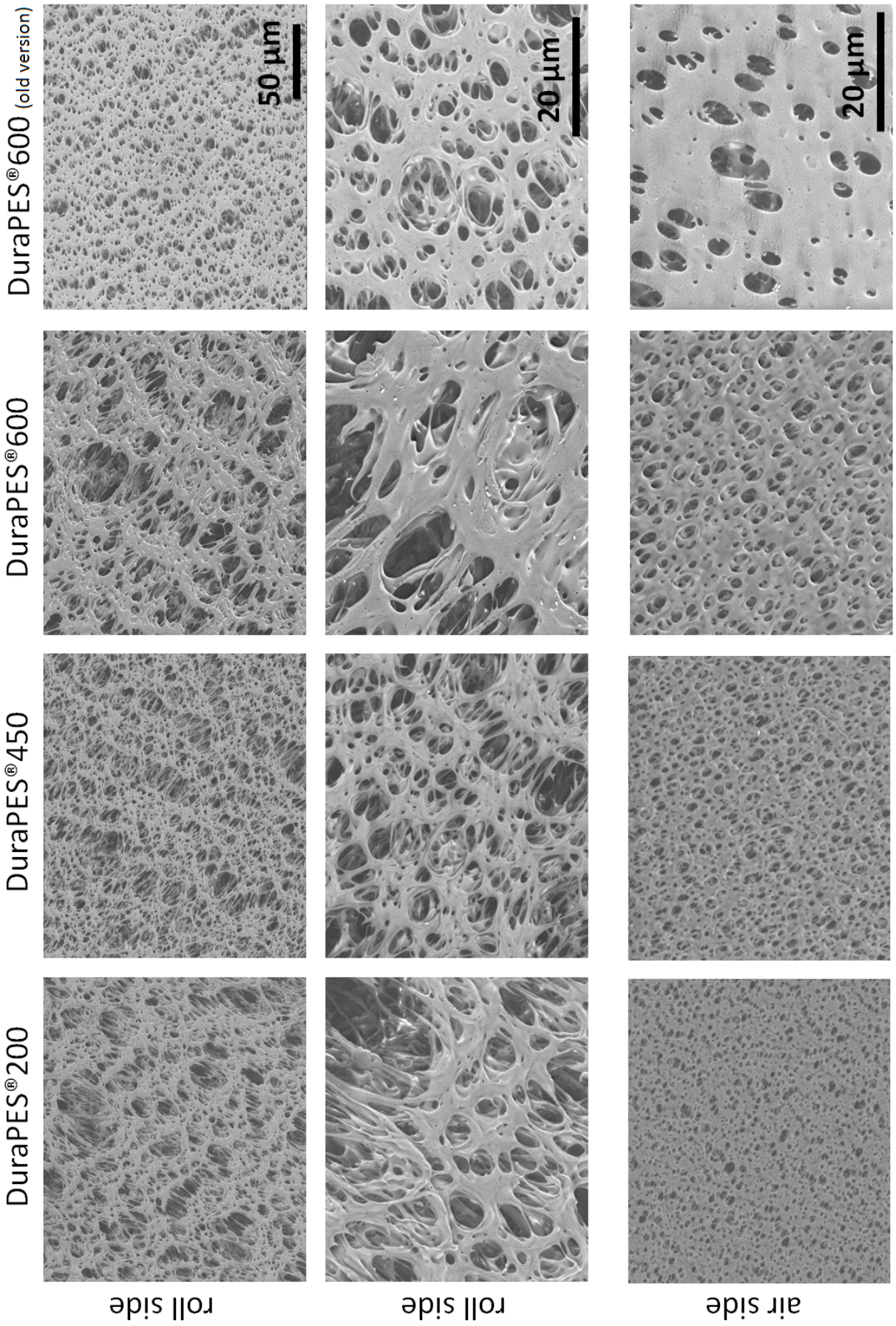

Fig. 23. SEM images of the surface morphology of the roll side and the air side of the Membrana DuraPES® membranes, with the roll side imaged at two different magnifications.
(low vacuum mode, P = 0.5 Torr, electron energy = 5 keV)

Generally, the investigation of small sample sections is reasonable only when the specific section is representative of the whole sample. This can be a problem, especially when the membrane surface morphology changes within the sample sheet as is the case for the DuraPES®600 membrane. For a thorough investigation of this membrane, samples were taken at different positions of the membrane sheet (see Fig. 24).

Fig. 25 shows images of the surface morphology of both the roll and air side of the DuraPES®600 membrane at the positions marked in Fig. 24. On the roll side, the central section of the sample sheet (section B) and the two outside sections (sections A and C) vary in their morphology. The pore size in the central section is much smaller than that of the outside sections. However the main membrane properties (retention rate or TMF) do not seem to be strongly influenced by this morphological anomaly. This may be due to the fact that this anomaly is confined to the surface, because Fig. 31 proves that the cross-sections of all three sections show very similar structures.

3.1.2 Morphology of the membrane cross-sections

Embedding of the membrane is essential for proper observation of the membrane cross-sections. Resin is generally used for embedding in order to stabilize fragile sample structures during the subsequent cutting or polishing process. The final sections should be as flat as possible, without any scratches or other artifacts induced by the preparation procedure. In the present work ultramicrotomy [51] was used for the preparation of the cross-sections. Additionally, an alternative method for achieving membrane cross-sections without embedding was developed and compared with the traditional method.

3.1.2.1 Preparation of membrane cross-sections by ultramicrotomy and cryo-ultramicrotomy

Different types of resin are available for sample embedding. Care must be taken in the choice of the resin, because embedding can cause swelling or shrinking of the samples. Fig. 26 shows cross-sections of the Membrana DuraPES®200 embedded in three different resins. The right column shows the separation layer marked in the left column at higher magnification. The parameters used for the embedding procedure are listed in Table 2. Small parts of the membrane (size approximately 5 mm × 3 mm) were put into the mixed resin. Due to the hydrophilic properties of the pore surfaces, the resin penetrates into the membrane structure without the need to apply vacuum. Afterwards the membrane cross-sections were prepared by ultramicrotomy at room temperature (Fig. 26, first three rows) as well as under cryogenic conditions (Fig. 26, last row). The best image results were obtained using the resins Specifix 40 and Epofix (both from Struers A/S). UHU+ shows additional contrast in the resin itself due to nitrogen containing components (white arrows).

The two vertical red lines in Fig. 26 mark a thickness of 150 µm. No swelling seems to occur in the membranes embedded in UHU+ and Epofix, whereas the Specifix 40 sample shows a swelling of around 5%. But as the three different samples were not taken at exactly the same position of the membrane sheet, this thickness difference could also be due to thickness differences within the membrane sheet itself.

Additionally, atomic force microscopy (AFM, Veeco Dimension 3100) was used to obtain information about the surface roughness. The instrument was operated in tapping mode. A detailed description of AFM can be found in [52]. Fig. 27 shows topographic AFM images of the membrane separation layer embedded in the different resins. An additional height profile is given at the position of the white lines marked in the images. The flattest surface can be achieved using Specifix 40; Epofix also shows small height variations. In the case of UHU+, cutting at RT results in much greater height variations than cutting under cryogenic conditions.

In contrast to Specifix 40, both UHU+ and Epofix are not transparent. This makes the handling of the embedded sample (see section 3.2.1) much more difficult as the orientation of the membrane sheet within the resin is not visible.

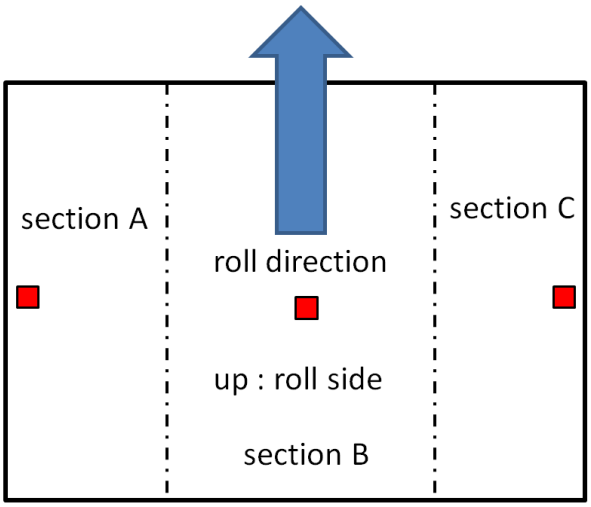

Fig. 24. Positions of the sections imaged in Fig. 25.
(sheet width approximately 28cm)

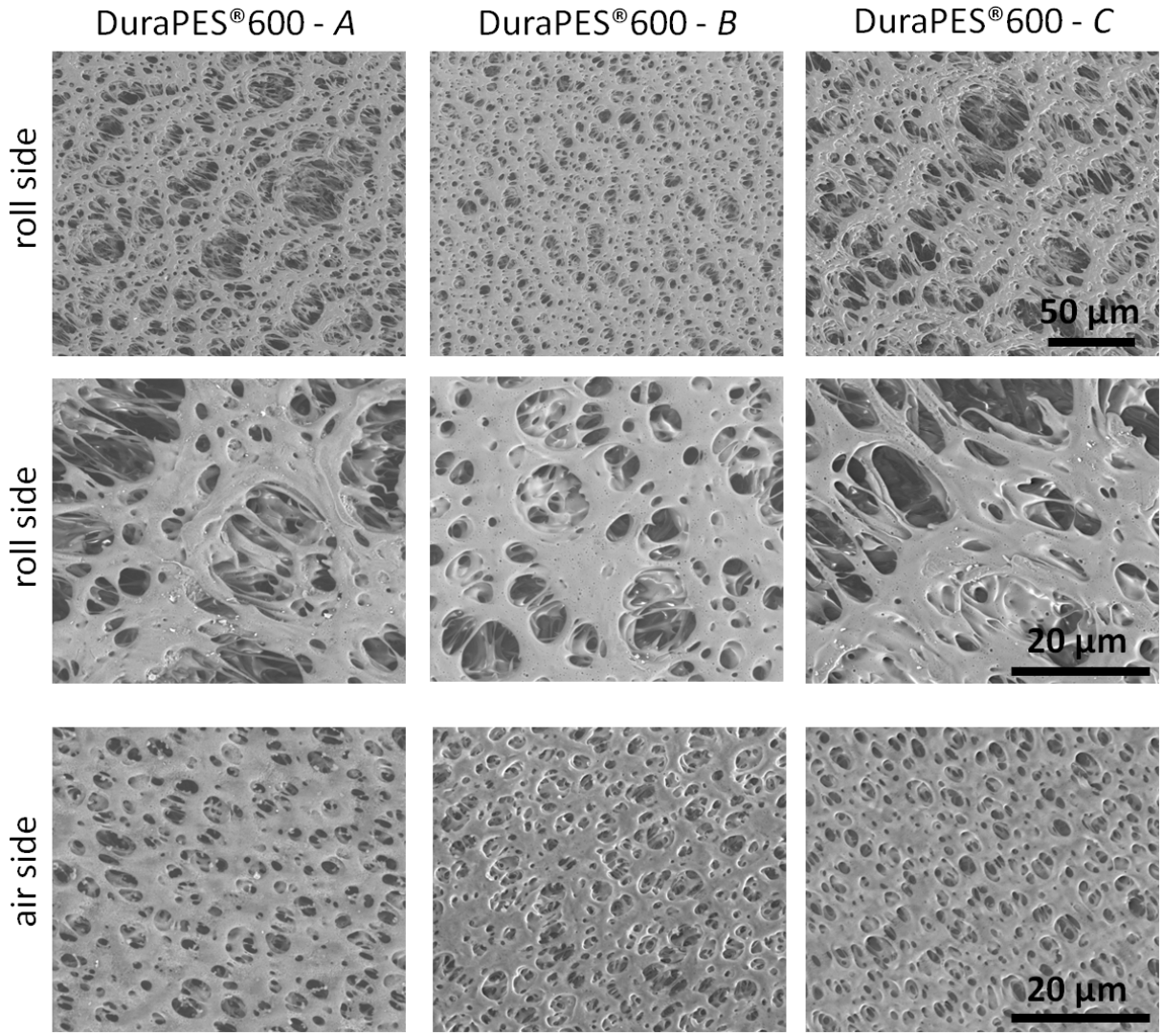

Fig. 25. SEM images (BSE) of the surface morphology of the Membrana DuraPES®600 at different positions of the sample sheet marked in Fig. 24.

(low vacuum mode, P = 0.5 Torr, electron energy = 5 keV)

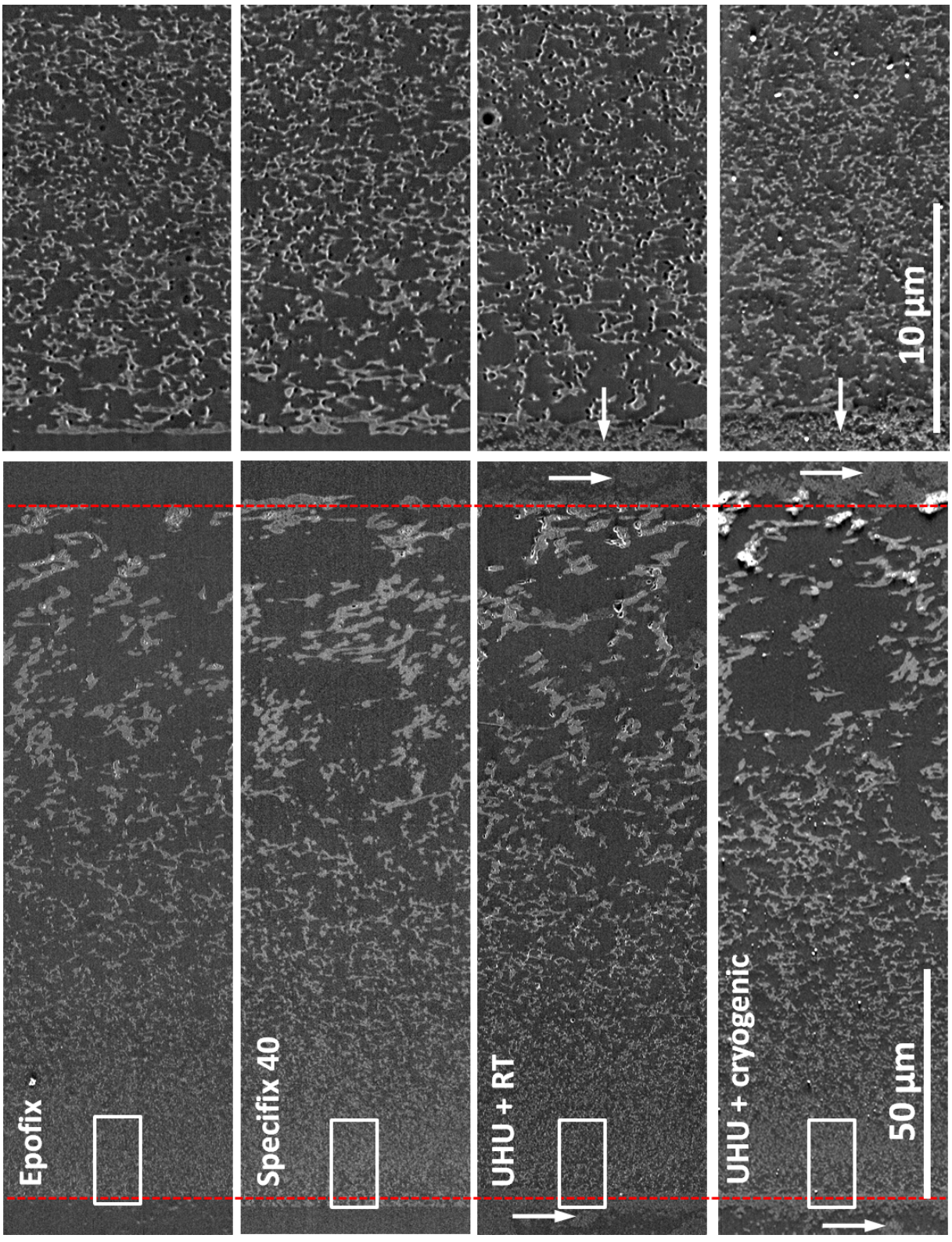

Fig. 26. SEM images (BSE) of the DuraPES®200 membrane cross-sections, with the membranes embedded in Epofix, Specifix 40, UHU+ and UHU+ cut under cryogenic conditions;
(low vacuum mode, P = 0.5 Torr, electron energy = 4 keV for all images).

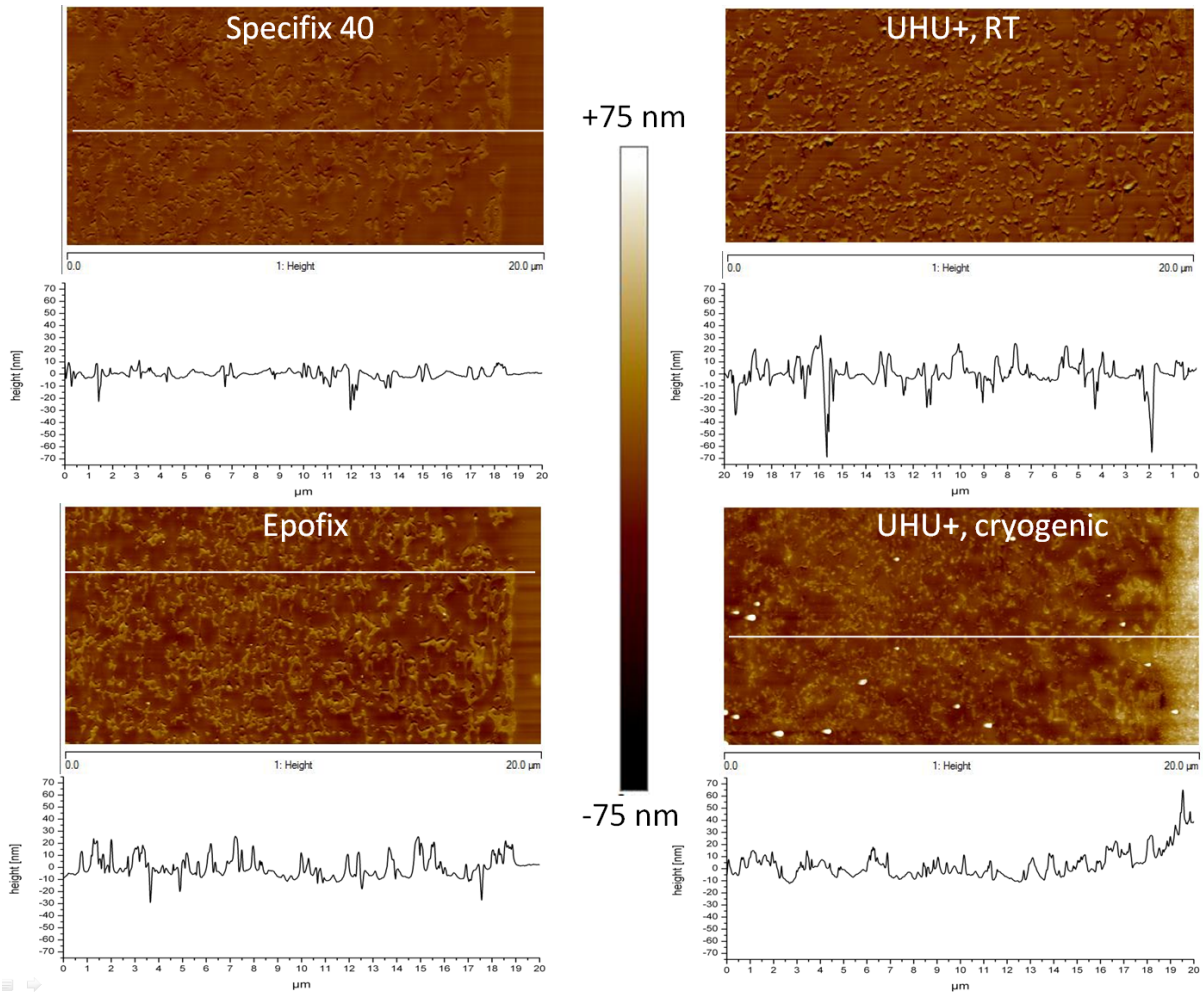

Fig. 27. AFM topographic images of the separation layer of the DuraPES®200 membrane, with the membrane embedded in Epofix, Specifix 40, UHU+ cut both under RT and cryogenic conditions.

Table 2: Parameters used for embedding the membranes in various resins.

Resin	Curing time [hours] at 21°C	Mixing ratio resin / curing agent
Specifix 40	8	7 :1
Epofix	12	25:3
UHU+	12	1:1

SEM imaging was carried out using backscattered electrons. As mentioned in section 2.3.1.4, the BSE coefficient and thus the detector signal increase with the mean atomic number of the material. Therefore, due to the sulfur in the membrane matrix, the membrane appears brighter than the resin. All membranes were embedded in Specifix 40 for further investigation. Possible thickness changes due to the embedding are listed in Table 4 below.

Relatively long recording times were necessary to achieve both high contrast and a high signal / noise ratio. Yet soft materials can be prone to radiation damage, which also increases with recording time. Both problems can be minimized by staining of the membrane material with heavy metals, e.g. osmium or ruthenium tetroxide. On the other hand, staining can also harden the polymer and cause the material to become brittle, resulting in scratches and cracks during the cutting process. A sketch of the staining procedure is given in Fig. 28. The non-embedded membranes were exposed to a RuO_4 atmosphere for 5 min. Afterwards the samples were embedded in Specifix 40 as described above. A detailed description of the staining procedure can be found in [51].

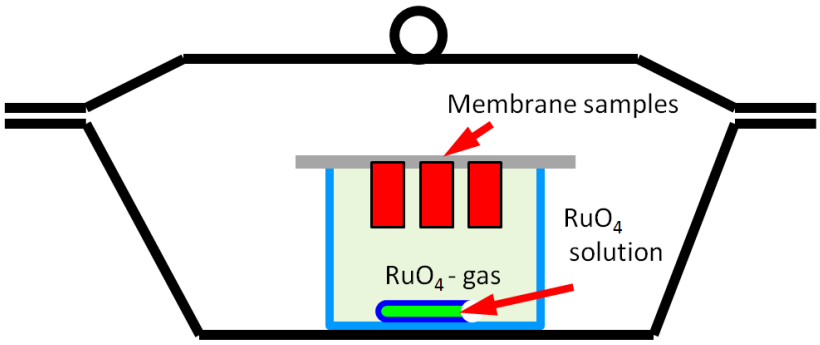

Fig. 28. Staining of the membranes in RuO_4; adapted from [51].

Fig. 29a and b show the cross-section of the MicroPES®4F membrane stained with RuO_4 for 5 minutes. The short staining time resulted in inhomogeneous staining. The surface and the separation layer (marked with a red *) appear brighter than the rest of the membrane cross-section (marked with a white *). This can cause problems with image segmentation as will be discussed in section 3.4.1. Moreover staining hardens the membrane material and causes it to become brittle, which leads to the formation of cracks (red arrows Fig. 29b). Fig. 29c and d show the unstained cross-section; the intrinsic contrast is sufficient for further image processing. Therefore no staining was carried out for the actual membrane investigations and potential noise was removed by subsequent image processing.

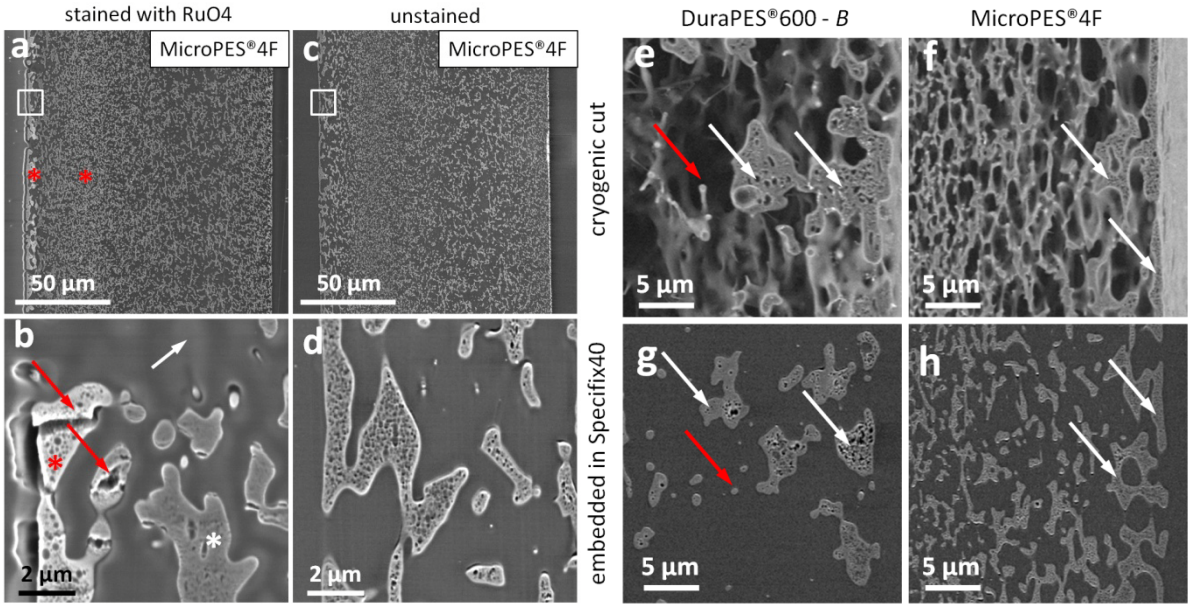

Fig. 29. SEM images (BSE) of the cross-sections of the MicoPES®4F membrane stained with $Ru0_4$ 5 min (a and b) and unstained (c and d); b and d are images of the areas marked by rectangles in a and c; SEM images of details of the membrane cross-section of the DuraPES®600 and MicroPES®4F. e and f: cryogenic cut of isopropanol wetted membrane, g and h: embedded in Specifix 40.

(low vacuum mode, P = 0.3 Torr, electron energy = 5 keV)

Wetting with isopropanol (ISP) is a quick and rough way to characterize the membrane cross-section without using ultramicrotomy. After putting the membrane into liquid nitrogen (LN_2) the frozen alcohol stabilizes the membrane structure and it can be easily fractured [24]. The resulting membrane cross-section, however, is very bumpy. But if the ISP wetted membrane is immediately mounted in the cryo-ultramicrotome it can be sectioned to achieve a flat and undeformed surface.

Table 3. Ultramicrotomy and cryo-ultramicrotomy operating parameters.

	Knife	Temperature [°C]	Slice thickness [nm]	Cutting speed [mm/s]
Ultramicrotomy	DIATOME 45°	RT	120	1.0
Cryo ultramicrotomy	DIATOME Histo cryo 45°	–120°C	200	1.0

Table 3 lists the operating parameters used for microtomy. The quality of the resulting block face is strongly dependent on both the sample material and cutting speed. Fig. 29e and f show SEM images of ISP wetted cryo-ultramicrotomy cuts. All fragile membrane structures seem well preserved and resemble those obtained by ultamicrotomy after embedding the membranes in Specifix 40 resin (Fig. 29g and h).

These SEM images are suggestive of a stronger three dimensional impression of the membrane structure than those that were obtained from the embedded membranes. The membrane structure is free and the cut is flat and precise. The so prepared samples were used for the visualization of the wetting and drying behavior of the membrane cross-section. The experimental setup and the results will be discussed in sections 3.3 and 5.4 respectively.

Although the contrast in the SEM images is sufficient for PES membranes, staining can be necessary for other types of membranes, e.g. cellulose acetate membranes. As these membranes do not contain any inorganic components the contrast to be expected between membrane and embedding medium will be very low. And cellulose acetate membranes are even more prone to radiation damage than PES membranes. In such cases staining will be definitely necessary and must be properly adapted to the type of membrane material used.

3.1.2.2 Overview of the membrane cross-sections

Fig. 30 and Fig. 31 give an overview of the cross-sections of the membranes studied. The left edge of the images shows the air side and the right edge the roll side. The top image always shows the cross-section of the respective membrane embedded in Specifix 40 and subsequently cut by ultramicrotomy at room temperature, while the bottom image shows the cross-section after cryo-ultramicrotomy of membranes wetted with isopropanol. As both samples were taken from nearly the same location at the center of the membrane sheet, any differences should be due to the preparation process and not to thickness variations of the membranes.

All membranes show a strong asymmetric structure. The different layers (support and separation layer) can easily be identified. The nominal pore sizes increase from left (0.2 µm) to right (0.6 µm). The DuraPES® membranes have a thickness of around (140 ± 10) µm and the separation layer is located very close to the air side. The roll side shows a very large free volume and pore sizes up to 20 µm. In contrast, the MicroPES® membranes are thinner (110 ± 10) µm and show two layers with very small pores, one located close to the roll side of the membrane, the other (actually the separation layer) approximately 30 µm beneath the air side. The Sartorius 15406 membrane has a similar structure, but the pore size difference between the separation and support layer is not that large - it has a less asymmetric pore structure. However the Sartorius 15406 membrane has the greatest thickness (150 µm).

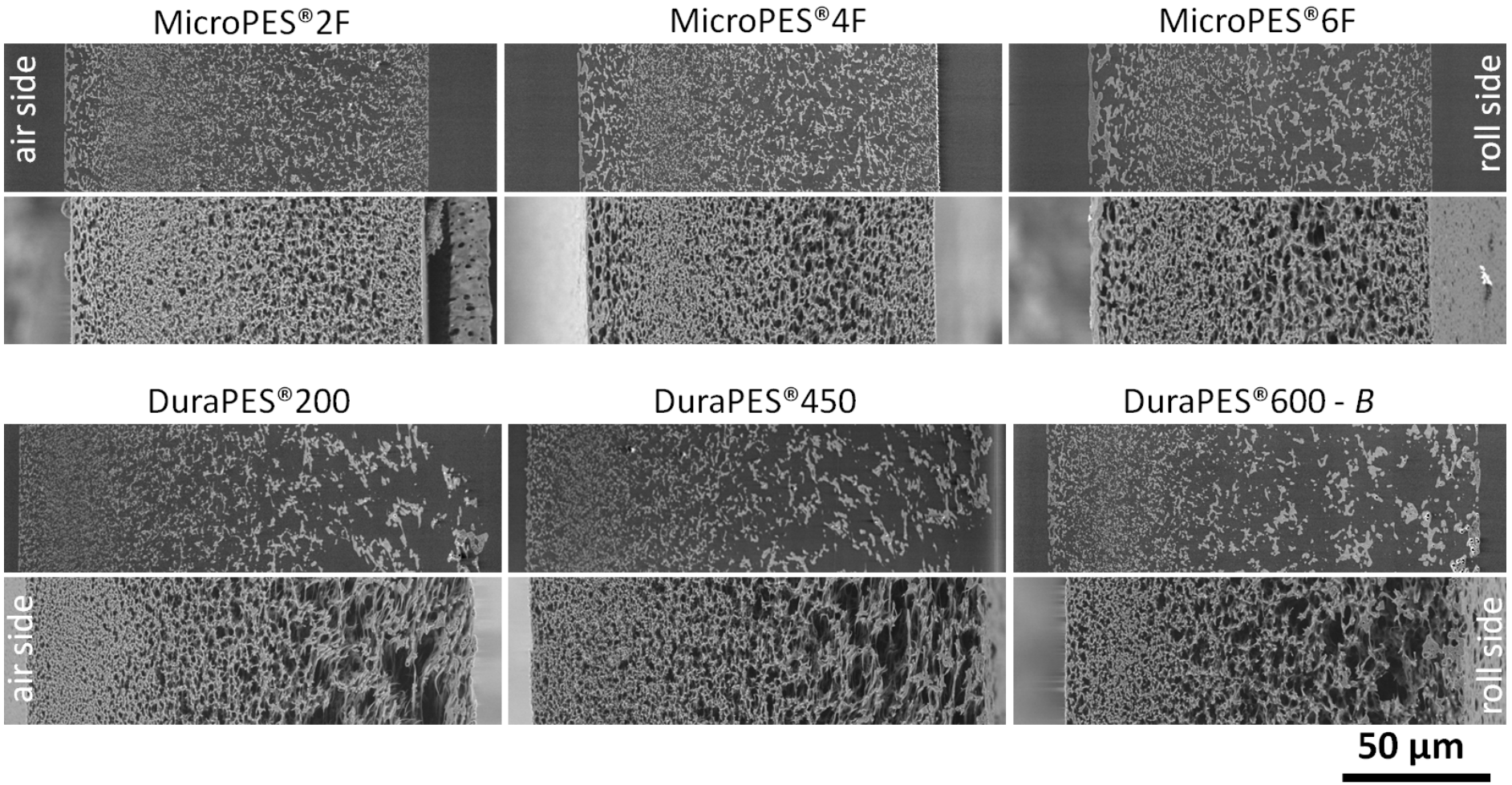

Fig. 30. SEM images (BSE) of the cross-sections of the investigated Membrana membranes. The left edge of the images belongs to the air side and the right edge to the roll side. The top image always shows the cross-section of the membrane embedded in resin (Specifix 40) and cut with an ultramicrotome at room temperature; the bottom image shows the cross-section of the same membrane prepared by cryo-ultramicrotomy after wetting in isopropanol (low vacuum mode, P = 0.3 Torr, electron energy = 5 keV).

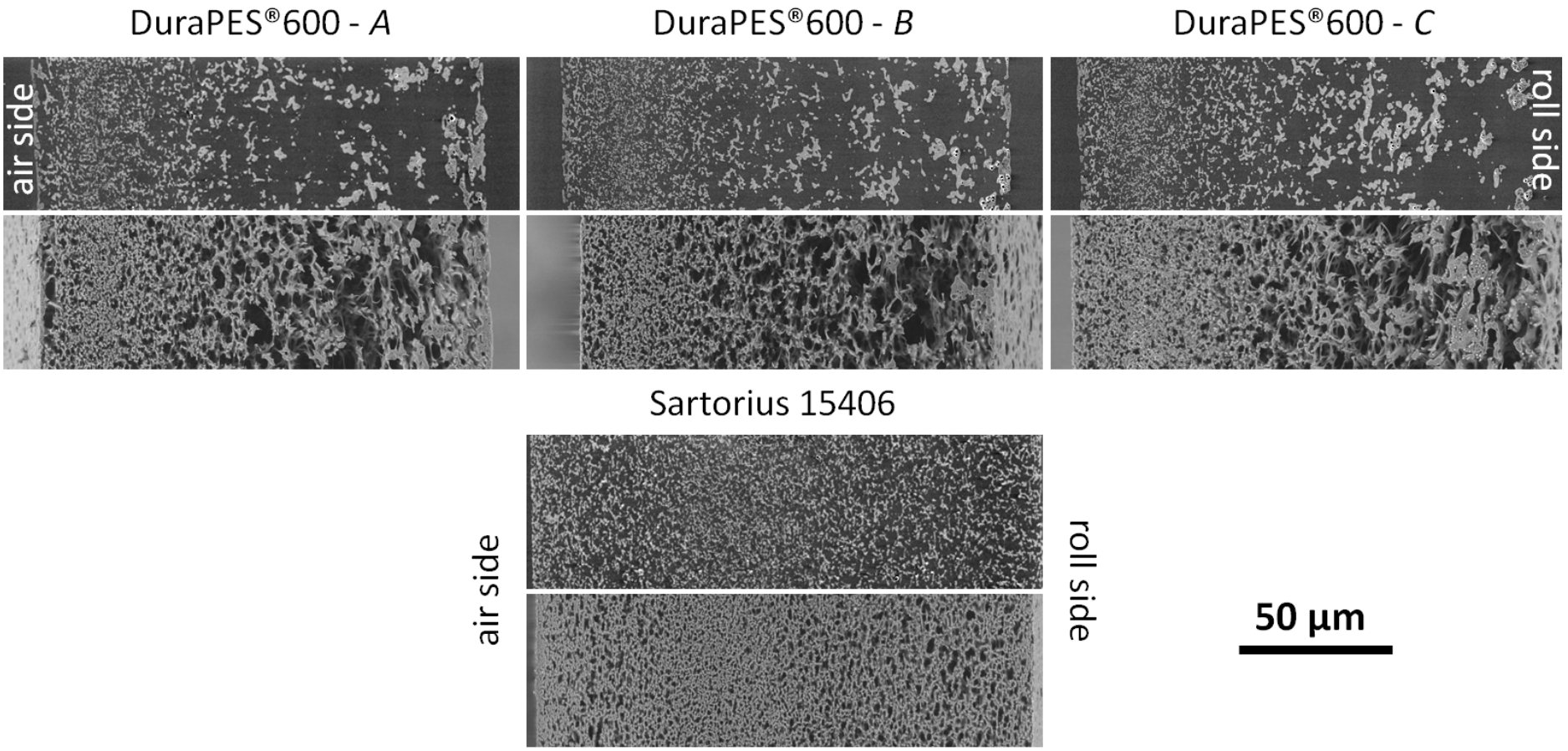

Fig. 31. SEM images (BSE) of cross-sections of the DuraPES®600 membrane recorded at the positions of the sample sheet marked in Fig. 24 and of the Sartorius 15406 membrane. The left edge belongs to the air side and the right edge to the roll side. The top image always shows the cross-section of the membrane embedded in resin (Specifix 40) and cut with an ultramicrotome at room temperature; the bottom image shows the cross-section of the same membrane prepared by cryo-ultramicrotomy after wetting in isopropanol.

(low vacuum mode, P = 0.3 Torr, electron energy = 5 keV).

Fig. 31 shows that the morphological variations visible on the surface of the DuraPES®600 as shown in Fig. 25 are indeed limited to the support layer.

Table 4. Nominal thickness, thickness after cryo ultramicrotomy, embedding in Specifix 40 and thickness change due to embedding for the membranes studied.

Membrane type	Nominal thickness [µm]	Thickness cryo cut [µm]	Thickness Specifix 40 RT cut [µm]	Thickness change [%]
MicroPES®2F	110 ± 10	119	124	+ 4
MicroPES®4F	110 ± 10	118	122	+ 3
MicroPES®6F	110 ± 10	114	117	+ 3
DuraPES®200	140 ± 10	152	159	+ 5
DuraPES®450	140 ± 10	156	157	+ 1
DuraPES®600A	140 ± 10	146	148	+ 1
DuraPES®600B	140 ± 10	136	146	+ 7
DuraPES®600C	140 ± 10	154	150	– 3
Sartorius15406	approx. 150	162	167	+ 3

Small thickness variations along the membrane are always to be expected. But cross-sections prepared by different procedures necessarily originate from different parts of the membrane. Therefore, it is rather difficult to determine whether thickness differences are due to swelling caused by embedding in resin. In most cases, however, a thickness increase of a few percent was observed due to the embedding procedure - which is in agreement with the observation described in section 3.1.2.1.

3.1.3 Chemical characterization of the membranes

The main component of the membranes used in the investigations is PES. As already mentioned in chapter 2, additives are generally used to create a hydrophilic surface. All residual solvents are washed off the membrane after passing the coagulation bath. Nevertheless the chemical composition of the membranes was checked using Fourier transform infra-red spectroscopy (FTIR). This study used a Bruker Equinox 55 / Hyperion 3000 FTIR spectrometer with ATR objective (MIRacle from PIKE Technologies with diamond crystal). A detailed description of FTIR can be found in [53,54].

The membranes DuraPES®600 / 200, MicroPES®2F / 4F and Sartorius 15406 were investigated. Fig. 32 shows the resulting spectra. As expected, all spectra show nearly the same typical PES spectrum (Fig. 32g) and no other revealed components with a concentration above the detection limit. The preparation procedure using ISP did not result in a change in the chemical composition (Fig. 32b).

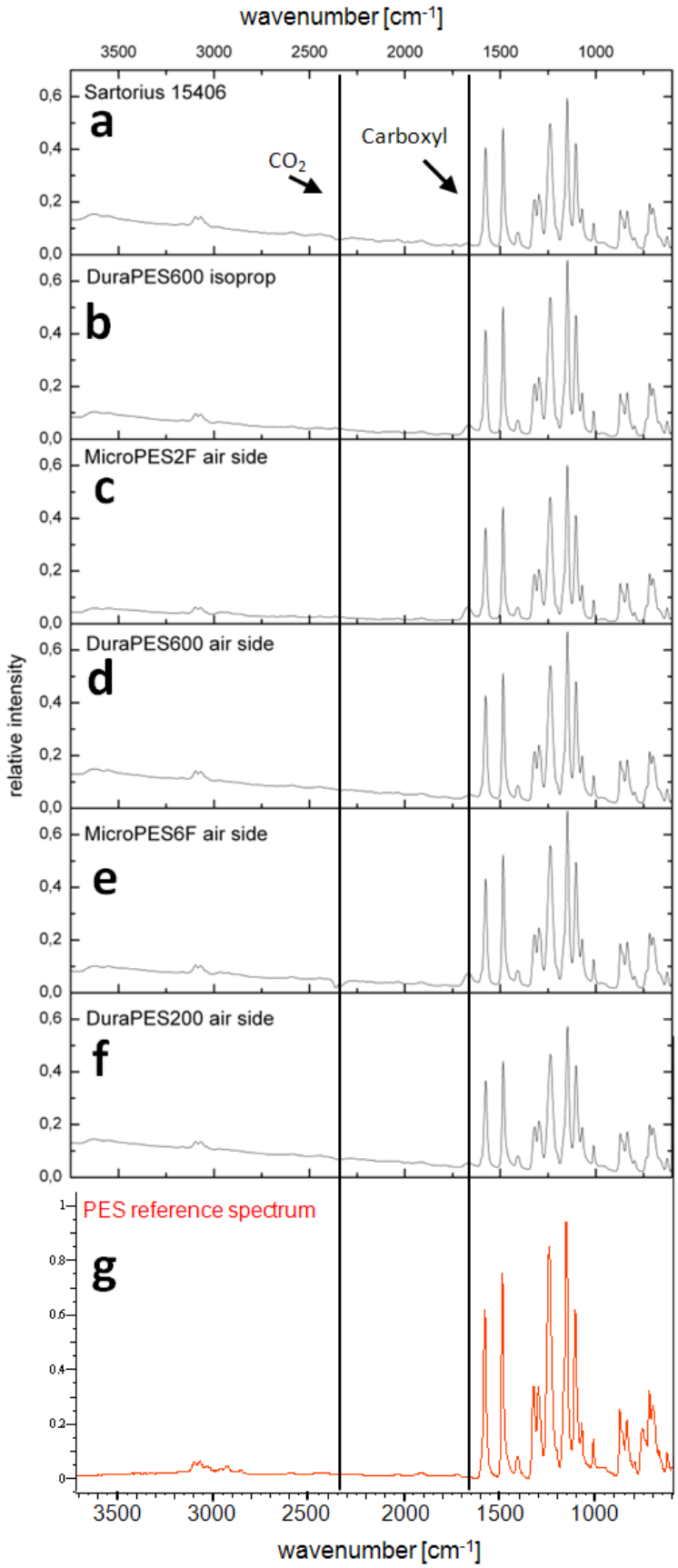

Fig. 32. FTIR spectra of the membranes studied (a, c-f), DuraPES®600 membrane after wetting in isopropanol and subsequent cryo preparation (b), PES reference spectrum (g)[2].

[2] Database: KnowItAll from Bio-Rad Laboratories Inc.

3.2 *In situ* ultramicrotomy (Serial block face SEM- SBFSEM)

Serial sectioning and imaging of the residual block face for gaining 3D information of the sample was first introduced by Leighton [55]. As the ESEM technology was not available at that time, the sample was coated with an Au-Pd layer after each cut to avoid surface charging when observing the block face under high vacuum conditions. The sputtering process was not performed inside the sample chamber and so the process was not implemented automatically. Many years later Denk and Horstman [11] developed a serial sectioning system using an automated *in situ* ultramicrotome mounted at the door of the specimen chamber of an environmental scanning electron microscope, eliminating the need for specimen coating.

This finally enabled fully automated and unattended serial sectioning and imaging. Nevertheless intervention by the operator is sometimes necessary. Due to electrostatic forces the slices are first collected at the back of the diamond knife, but sometimes debris fall back onto the block face. As a consequence the images of the respective block faces cannot be used for 3D reconstruction.

If thin slices are investigated with TEM, the structures of the slice of the given thickness are imaged. This is different from serial block face imaging in the ESEM, where the electrons penetrate the specimen, with the penetration depth depending on the sample density and electron energy (see also section 2.3.1.4). The penetration depth determines the information depth, which should coincide with the slice thickness. If the information depth is larger than the slice thickness, the images contain information from several slices, making a sound 3D reconstruction impossible. Therefore the electron energy must be sufficiently low to enable correct 3D reconstruction. One must also be aware that in case of cubic voxels the slice thickness also determines the resolution in all directions. The effect of using too high electron energies was shown by Denk in [11].

The optimum microscope parameters for imaging can be found by using Monte Carlo simulations. But Fig. 33 also provides direct proof that the parameters for subsequent 3D reconstruction are chosen correctly. The left figure shows three image planes perpendicular to each other and in relation to the incident electron beam and the cutting direction. Image sharpness and accuracy in detail is comparable in all three planes (Fig. 33, right). The images normal to the cutting direction were obtained by 3D reconstruction.

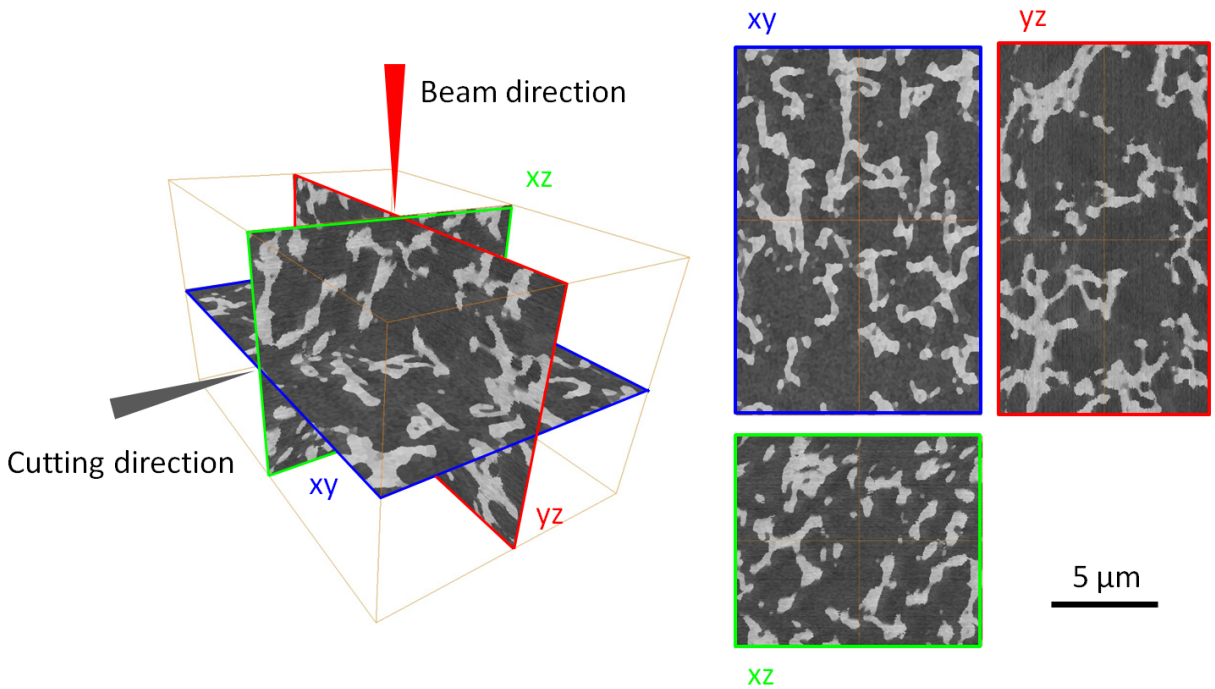

Fig. 33. Left: Image planes in relation to the electron beam and the cutting direction; right: images in beam direction (xz and yz - obtained by 3D reconstruction) and perpendicular to the beam (xy - SEM image). They all show the same sharpness and accuracy in detail.

The maximum sample dimensions and the specimen holders of this special microtome differ from those of commercial microtomes, thus requiring extra steps in sample preparation and sample mounting.

3.2.1 Sample preparation for *in situ* ultramicrotomy

The sample is first fixed on a special holder which has the form of a rivet. The small dimensions of both the rivet and the diamond knife (cutting width: 1.2 mm) requires a special sample preparation. The embedded sample (as described in section 3.1.2.1) must be cut to a size of approx. 0.5 mm × 0.5 mm × 0.5 mm using razor blades or microtome trim knives. Subsequently this small cube must be cut off from the rest of the sample with a razor blade and fixed on the top of the rivet using a gel adhesive (UHU Supergel Sekundenkleber). The sample transfer to the rivet is very critical due to the small sample size. In the next step, the specimen must be cut using a conventional microtome in order to achieve a flat specimen surface. Finally the rivet is mounted in the *in situ* ultramicrotome. Fig. 34a shows the block face (1), the diamond knife (2), and the debris forming during the cutting process (3). The other figures show the sample cube fixed at the top of the rivet (Fig. 34b) and a top view of the sample cube (Fig. 34c).

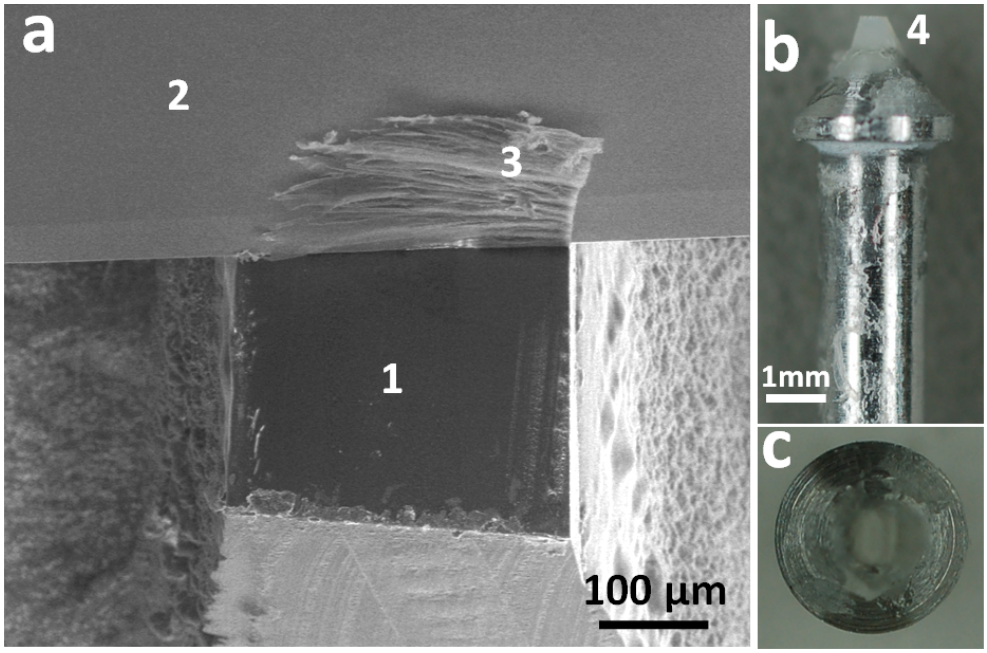

Fig. 34. View of the sample and microtome knife used for in situ *ultramicrotomy. a: a slice of the specimen (1) is cut by the diamond knife (2), with (3) showing the emerging debris; b: embedded sample (4) fixed at the top of the rivet; c: top view of (b).*

3.2.2 The Gatan 3View™ ultramicrotome

In this work serial sectioning was carried out using the Gatan 3View™ ultramicrotome (Gatan GmbH, Munich, Germany), mounted in the specimen chamber of an ESEM Quanta 600 FEG (FEI, Eindhoven the Netherlands). The experimental setup is illustrated in Fig. 35a. The sample stage allows moving the rivet in x and y direction to find the region of interest. Due to the fixed z position of the diamond knife, the WD is fixed at 6.7 mm. The slice thickness can be adjusted in a range from 20 nm to 200 nm. A motor drive (from Physik Instrumente - PI) provides accurate and reproducible sample feed and thus also slice thickness.

Backscattered electrons were used for imaging. They were detected with a special BSE detector positioned directly under the pole piece featuring an increased detection performance at low electron energies (below 5 keV). The enlarged detection area, compared to the original FEI detector, enables shorter dwell times, but also reduces the field of view to approximately 1mm.

As the sample is electrically non-conductive the microscope is operated in the low vacuum mode. Water vapor was used as the imaging gas. The water vapor atmosphere minimizes charging as described in section 2.3.2. But residual charges can still lead to bright artifacts which can be corrected by image processing (see section 3.4.1). All parameters used for slicing and imaging, such as water vapor pressure, primary electron energy, slice thickness etc. are listed in Table 10.

3.2.2.1 Mounting and sample adjustment

The height distance (z direction) between sample surface and diamond knife must be adjusted at the open microscope door with the help of an additional light microscope. For this purpose the flat sample surface is illuminated with light, and the reflecting parts of the diamond knife edge (visible at the block face) are observed with the light microscope. The sample is moved in z direction until the knife edge and the reflection of the knife edge at the block face are close to each other. After this manual adjustment the automatic feed can be used. An adjustment routine of the 3View™ controlling software DigitalMicrograph™ (DM) moves the sample sequentially in z direction, until the knife edge position and the sample position are at the same level. Afterwards the additional light microscope can be removed and the sectioning and imaging process can begin.

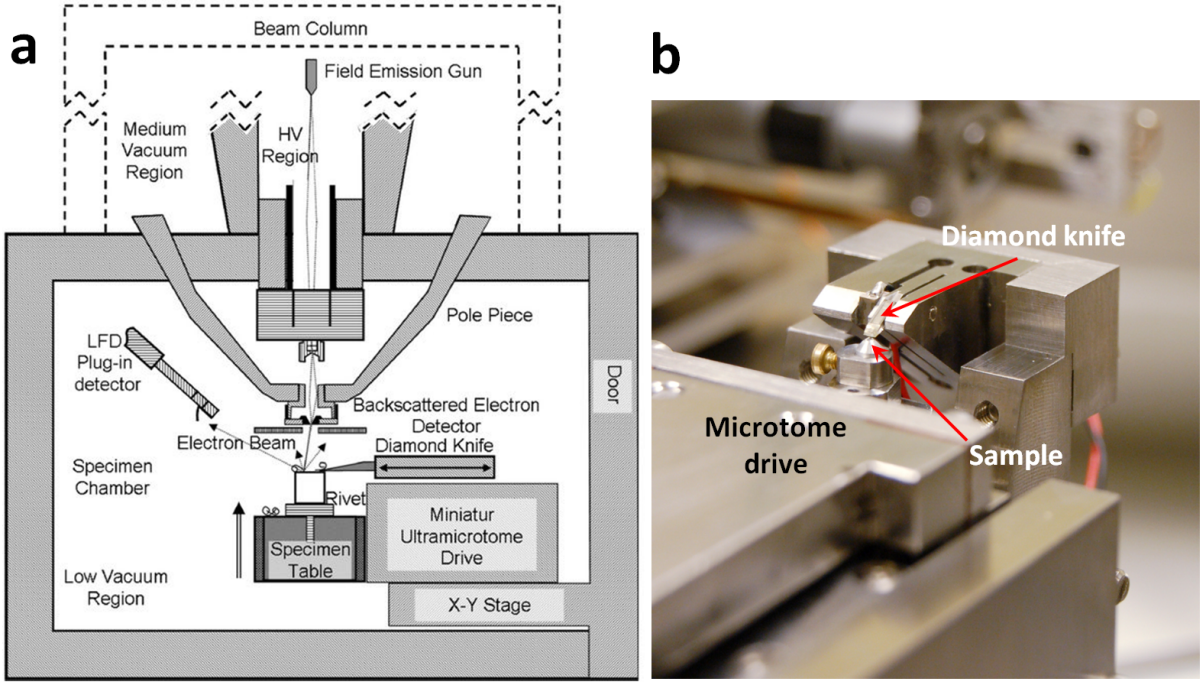

Fig. 35. a: sketch of the Gatan 3View™: an ultramicrotome is mounted at the door of the microscope, b: view on the diamond knife and the sample; adapted from [56].

3.3 Experimental setup for wetting and drying of the membranes

The specimen chamber of a conventional SEM is operated in high vacuum (< 10^{-4} Torr). The introduction of wet samples into the sample chamber of such an instrument would cause a breakdown of the vacuum. It was Danilatos who developed a low vacuum SEM which enables the investigation of liquid samples [57]. The chamber pressure in the instrument (ESEM Quanta 600 FEG from FEI) used for the investigations is limited to a range of 0.1 to 20 Torr. To restrict on the one hand condensing of water to the sample and on the other hand to decrease the dew point and minimize skirting in general cooling of the sample is necessary. A sample temperature of 3° to 5°C has been found to be an optimal operating parameter, with the phase transition taking place at a chamber pressure of 5.5 to 6.5 Torr (Fig. 36). As mentioned in section 2.3.2.4, the skirt effect results in a tradeoff between the signal-to-noise ratio and both gas amplification and WD.

Special Peltier cooling stages are commercially available for sample cooling (Fig. 37a). The sample is placed into a cup, which is cooled by the Peltier element and is available in different shapes. The cooling stage enables fast and flexible cup replacement, because the cups are only loosely placed on the actual specimen stub of the cooling stage. However, the thermal contact between cup and cooling stage is not optimal. The temperature measured at the cooling stage is thus lower than that at the specimen. Moreover most available cups are only suitable for powders or granular samples. The temperature gradient between cup and sample causes the water to condense first at the cup walls and only subsequently wet the sample. Massive samples (membranes, paper, foils etc.) must be mounted at the rim of the cup and then appropriately bent to contact the bottom of the cup. But in this way a reproducible wetting of the specimen is not possible. This problem can be avoided by using a water injection system. The water can be injected onto the sample at a predefined position using a capillary [58]. However, the sample as well as the injected water must be cooled to avoid water vapor formation. Taking the mentioned aspects in account a development of a new cooling stage is required. The new experimental setup should meet the following requirements:

- adequate membrane fixation and cooling,
- reproducible wetting / drying of the membrane,
- simultaneous and unhampered drying at both surfaces,
- accurate temperature measurements at the membrane surfaces,
- appropriate dimensions to fit into the microscope chamber.

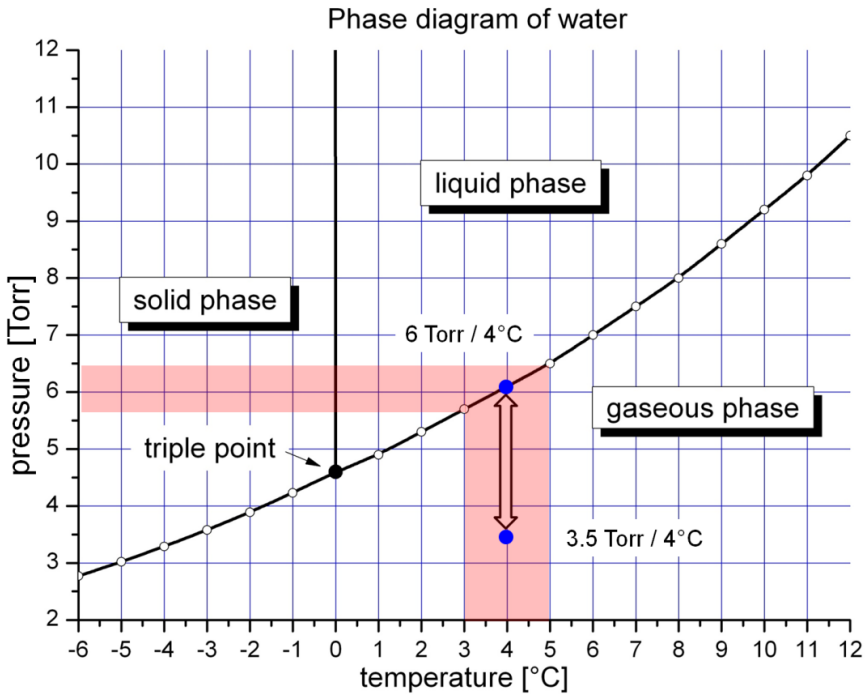

Fig. 36. Phase diagram of water, the optimal operating range is marked in red.

The main steps of the experimental progress are as follows:

- cooling to a predefined temperature (to 4°C),
- increasing the chamber pressure above the dew point (1 Torr to 6 Torr) to start water condensation,
- wetting of the membrane,
- decreasing of the chamber pressure below the dew point (6 Torr to 3.5 Torr),
- drying of the membrane and continuous image recording of the membrane surface.

The temperature profile at both membrane surfaces is recorded throughout the process.

3.3.1 Development of the experimental setup

The first very simple setup for the investigation of the wetting and drying behavior of membranes using a commercially available Peltier cooling stage is shown in Fig. 37a. To enable a reproducible double sided drying of the membrane, however, a new experimental setup had to be developed. The original cooling stage was thus replaced by a modified one as illustrated in Fig. 34b.

Water condenses at a special membrane holder (orange part in Fig. 37b), which is contacted directly to the cold side of the Peltier element and thus enables wetting of the membrane fixed at the cooling area. But the rest of the holder also gets wet and so too much additional water (outside of the cooling area) condenses. As a consequence the resulting evaporation heat caused substantial additional cooling of the system and the temperature of the cooling stage could therefore not be kept stable. Nevertheless, first (not reproducible) experiments enabled the observation of the drying process at the membrane surface.

To overcome these problems two small separate Peltier elements were used for the build-up of a new cooling stage. The cooling surface of the Peltier elements measures 6 mm × 6 mm and the element itself consumes 1.3 W power., Brass cooling clamps were fixed at the top of both elements using a thermally conductive adhesive (RS components Nr. 850-984). The hot sides of the Peltier elements were cooled by a heat sink, similar to that used in the original cooling stage provided with the microscope. Additionally, the distance of the cooling clamps can be changed stepwise by using different holes (Fig. 37c).

Due to the size and especially thickness of the membrane samples, the amount of water stored in the wetted membrane and the limited space between the detector and the sample surface, which is mainly determined by the WD, only micro thermocouples could be used for temperature measurements at the membrane surface. A detailed discussion of these measurements can be found in section 3.3.2.

The ends of the thermocouples had to be connected to the measuring equipment via a feed-through flange and special connectors (thermo connectors). The thermocouple itself (placed on a support) and a corresponding thermo connector were placed onto a Teflon holder. The handling of these so called thermo-sensor devices (Fig. 38a and Fig. 37d marked 3 and 4) was much more convenient than the thermocouple alone. Later the thermo-sensor device was fixed between two rails, facilitating precise positioning of the thermocouple at the membrane surface. (Fig. 37e - red arrows).

Cooling clamps for vertical membrane fixation were also developed (Fig. 37d marked 1 and 2) to enable the observation of the drying process at the membrane cross-section.

Moreover, each cooling clamp was also fixed between two rails. This has two advantages: first, the distance between the cooling clamps can be changed and so different sizes of membrane samples can be investigated. Second, the membrane can be clamped taut by adjusting the clamps as shown in Fig. 39b and c. This avoids movement or bending of the sample during the wetting / drying process and reduces the risk of losing the mechanical contact between the membrane surface and the micro thermocouple.

A further development was made concerning the cooling clamps themselves: Instead of two parts, they consisted of a monolithic part with a 0.3 mm horizontal or vertical slit (see Fig. 38 and insert in Fig. 40). The dimensions are 6 mm × 6 mm × 4 mm for the horizontal slit and 6 mm × 6 mm × 6 mm for the vertical slit. The membrane is clamped into the slit with a brass plate, making the connection between the cooling clamp and the membrane easier and repeatable. The temperature of the cooling clamps is controlled by a thermal resistor (Pt 100 from RS components) with a size of 3 mm × 2 mm × 1 mm mounted inside the monolithic block (Fig. 38 marked with B). A thermocouple (T Type COCO 005) mounted at position A in Fig. 38 measured the cooling clamp temperature. The thermocouples and the thermal resistor were first electrically insulated and then fixed to the cooling clamps. The cooling clamps themselves are electrically grounded with a spring contact to the microscope stage (marked with E in Fig. 38) in order to protect the sensitive inputs of the temperature logger from electric shocks.

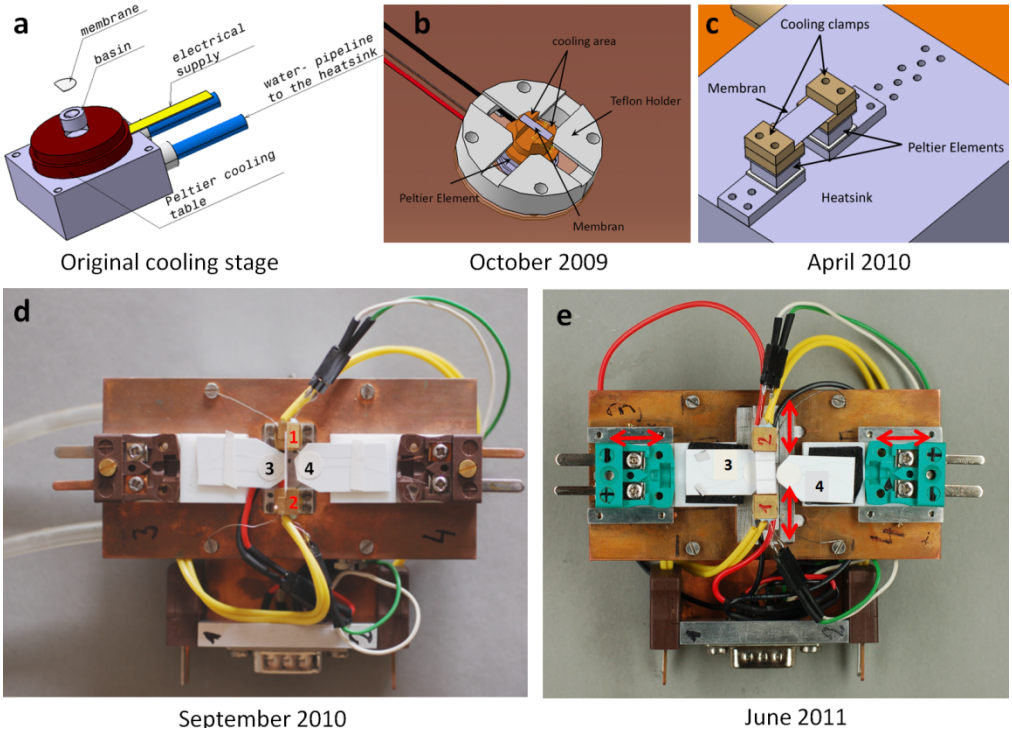

Fig. 37. Development of the experimental setup. a: original cooling stage delivered by FEI, b: modified cooling stage for double sided drying, c: first experimental setup using two clamps, d: experimental setup with clamps for vertical membrane mounting, electrical connectors and thermo-sensor device (3 and 4), e: final experimental setup with movable clamps and thermo-sensor device positioning (red arrows).

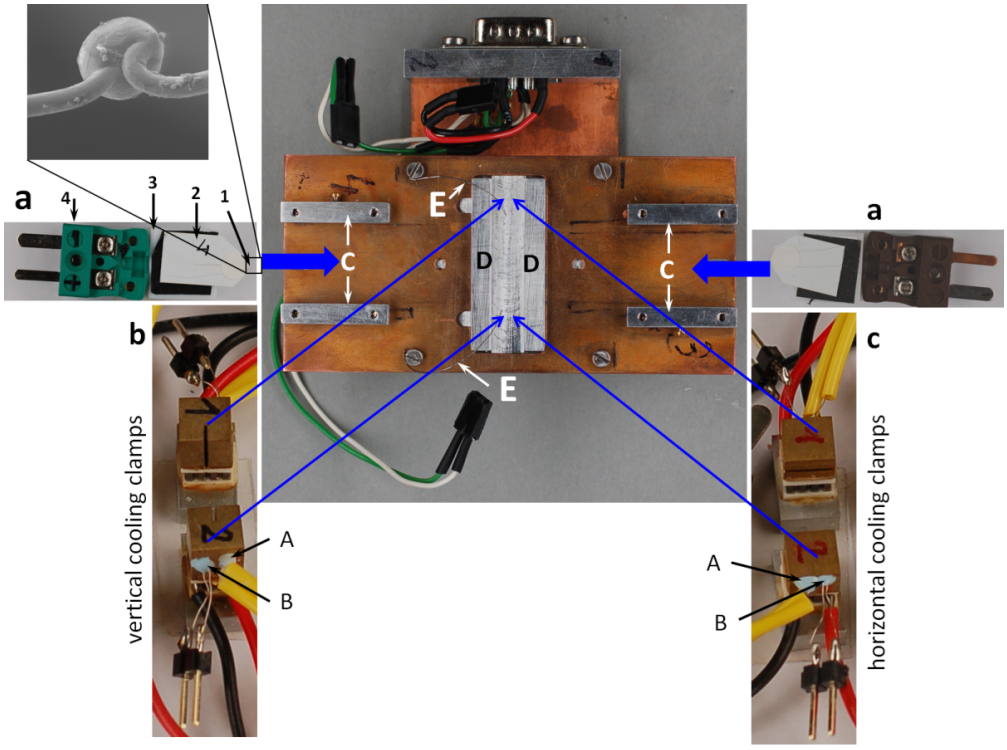

Fig. 38. Detailed view of the final experimental setup. a: adjustable thermo-sensor devices consisting of micro thermocouple (1) and support (2), Teflon holder (3) and thermo connector (4); movable cooling clamps for vertical (b) and horizontal (c) membrane fixation with Pt 100 thermal resistor (mounted at position B) and additional thermocouple (position A).

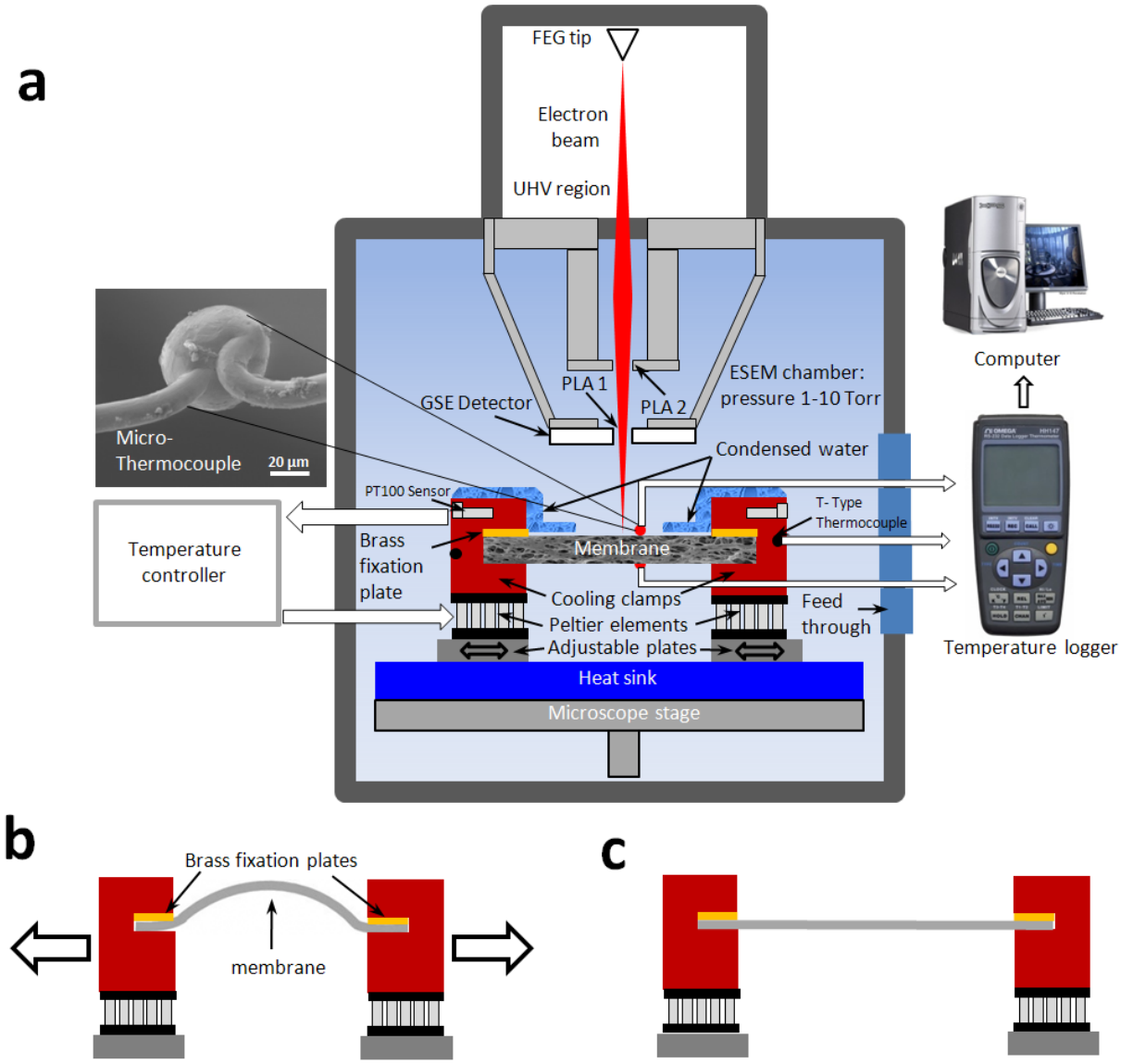

Fig. 39. Sketch of the experimental setup. a: cooling stage mounted inside the microscope chamber, b: flat sheet membrane mounted between two cooling clamps, c: the membrane can be tightened by adjusting the clamp positions; adapted from [4].

The cooling clamps for vertical membrane fixation are larger than those used for horizontal fixation. More water condenses on them as a result, which also influences the pumping procedure. Fig. 40 shows the chamber pressure as a function of time. The drying sequence is started by reducing the pressure in the specimen chamber from 6 to 3.5 Torr, which is below the dew point. This causes evaporation of water from the cooling clamps, resulting in a subsequent pressure rise.

The chamber pressure is controlled by a needle valve. Opening of the valve (ChEV) connects the pump (PVP2) and the sample chamber and so the pressure decreases (see also Fig. 18d path 5).

The clamps for vertical membrane mounting require one additional opening-closing sequence of the needle valve ChEV, which can be clearly seen in the pressure profile.

Therefore, if vertical cooling clamps are used, the drying process of the membrane needs more time than in the case of horizontal membrane mounting. This fact has to be considered in the discussion in section 5.4.

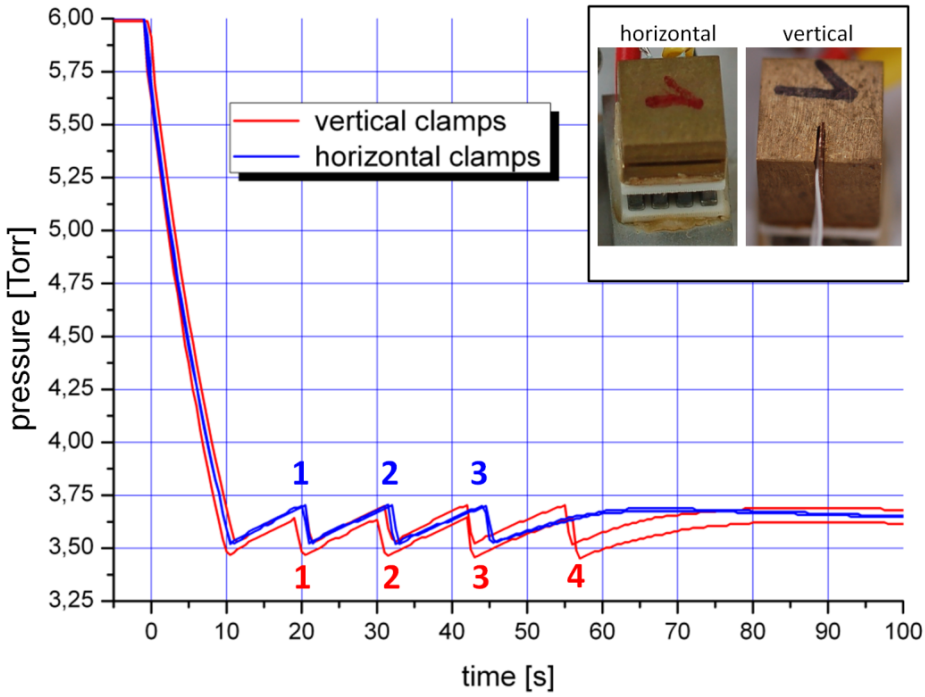

Fig. 40. Pumping sequence using cooling clamps for vertical (red curve) or horizontal (blue curve) membrane mounting: chamber pressure as a function of time after decreasing the pressure from 6 Torr to 3.5 Torr.

The sketch in Fig. 39 shows the experimental setup mounted on the stage of the microscope. The wires of the thermocouples were passed to the temperature logger instrument (HH147 from Omega® Newport) via a feed-through (Fig. 41). The contacts of the feed-through were made from the same alloys as those used for T type and K type thermocouples (listed in Table 7). This avoids unwanted electrical potentials due to temperature differences at the feed-through flange, which would distort the measurements. The temperature logger is connected to the computer by a USB port. The Peltier elements and the temperature of the cooling clamps were controlled by a control system already installed in the microscope for its original Peltier cooling stage.

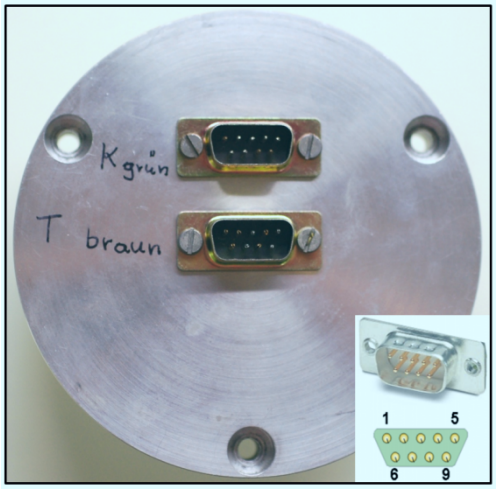

Pin	Type	Color / Polarity	Type	Color / Polarity
	Upper Sub-D connector		Bottom Sub-D connector	
1	free use - copper contact		free use - copper contact	
2	K	White –	T	Brown +
3		Green +		White –
4	K	White –	T	Brown +
5		Green +		White –
6	K	White –	T	Brown +
7		Green +		White –
8	free use - copper contact		T	Brown +
9				White –

Fig. 41. Flange with feed-trough for the connections of the thermocouples (left); Pin assignment of the connectors (right).

3.3.2 Temperature measurements

Accurate temperature measurement at the membrane surface is a big challenge. Micro thermocouples manufactured by Omega® Newport were used for this purpose. The types and dimensions of the micro thermocouples used in the experiments are listed in Table 5. The dimensions of the thermocouple heads and contact wires were obtained from the images shown in Fig. 42.

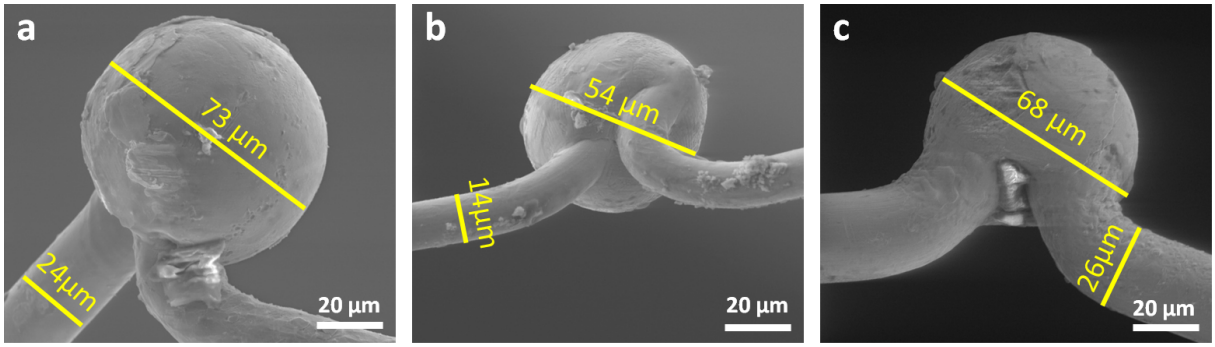

Fig. 42. SEM images (SE) of various micro thermocouples; a: T type thermocouple COCO 001, b: K type thermocouple CHAL 0005, c: K type thermocouple CHAL 001.

Table 5: Dimensions of the micro thermocouples used.

Type	D [µm]	d [µm]	Type
CHAL 0005	54	14 (12)[3]	K
COCO 001	73	24 (25)[3]	T
CHAL 001	68	26 (25)[3]	K

The smallest available device is a K type thermocouple (CHAL 0005). The handling of such a small device is not easy, however, and so the larger T type thermocouple (COCO 001) was used for the first experiments. In principle both thermocouple types (K or T type) should be suitable for the temperature range used. The thermocouple was fixed by using a thermally conductive adhesive (from RS Components), see Fig 43a. However, the adhesive penetrates deeply into the thin membrane, thus measuring not just the surface temperature, but an average value of a layer of a certain thickness. But the temperature measurements should provide information about the layer composition of the membrane, which would not be possible in this case. While this method of contacting is also not really reproducible, it nevertheless provides a rough idea of the membrane surface temperature behavior. As expected, the membrane temperature decreases during the wetting process. To achieve a repeatable temperature measurement, the use of an adhesive was abandoned and the micro thermocouple was only pressed against the membrane surface by its own flexible contact wires (Fig. 43b).

[3] Values in brackets provided by the manufacturer

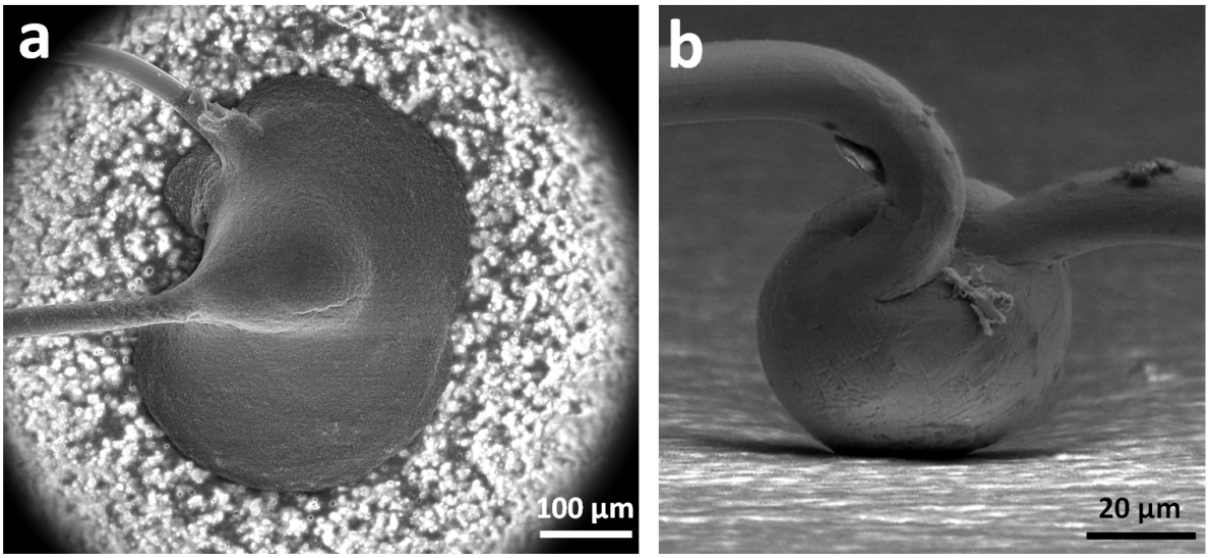

Fig. 43. Contacting of micro thermocouples at the membrane surface. a: micro thermocouple COCO 001 fixed to the membrane surface by a thermo adhesive; b: micro thermocouple CHAL 0005 contacting the membrane surface without adhesive, only by pressure exerted by the flexible wires.

Table 6: Properties of the thermocouple types used [59].

	Temperature range [°C]	IEC color	Sensitivity [µV/°C]	Alloy1 / Polarity	Alloy2 / Polarity
T Type	–250 to +350	brown	43	copper (+)	Constantan® (–) (55% Cu, 45% Ni)
K Type	–200 to +1250	green	41	Chromel® (+) (90% Ni, 10% Cr)	Alumel® (–) (95% Ni, 2%Mn, 2%Al, 1%Si)

The measurements revealed significant differences in the temperature profiles recorded during the wetting and drying of membranes using K and T type thermocouples of nearly the same size (Fig. 44). The possible reasons for the main differences in the temperature profiles will be discussed in the following, while a detailed description of the temperature profiles themselves can be found in sections 3.3.3 and 5.3.

The K type thermocouple measurements showed that the temperature decreases from about room temperature to approximately 4 to 5°C (Fig. 44 - temperature pair 2, CHAL 001) during the wetting process. This value indicates an accurate temperature measurement, as the thermal equilibrium is at the chamber pressure used (6 Torr), and therefore the temperature of the water, is consistent with that temperature value (see also the phase diagram in Fig. 36).

In the measurements using T type thermocouples (of nearly the same size) the temperature reaches a stable value of approximately 7°C to 9°C (Fig. 44 - temperature pair 1, COCO 001). The temperatures are generally higher than those measured with the K type thermocouples, whereas the temperature profile during the drying process corresponds to that measured with K type thermocouples. No significant temperature change is observed at the air side of the membrane, irrespective of the type of thermocouple used (curves marked 1 in Fig. 44), whereas the temperature measured at the roll side changes significantly in both cases and also shows a similar trend (curves marked 2 in Fig. 44).

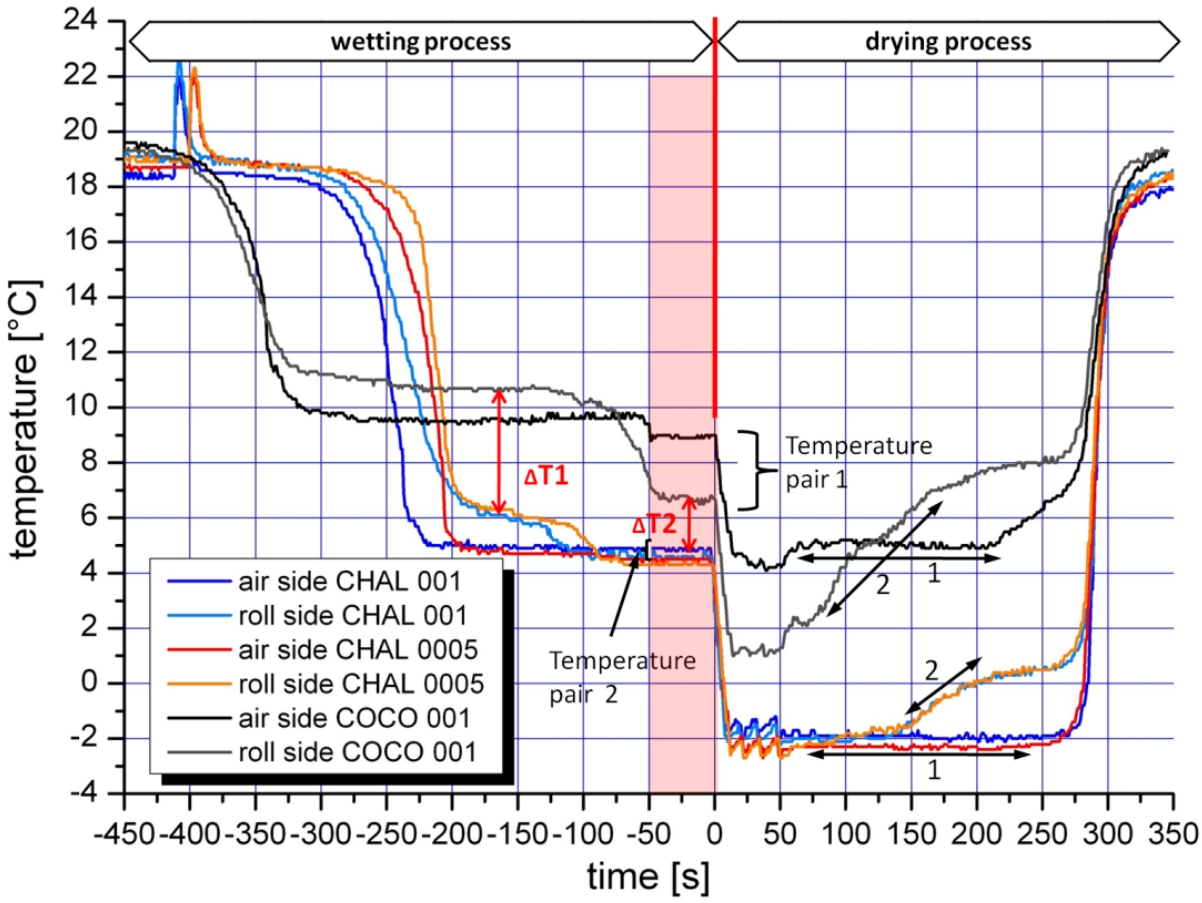

Fig. 44. Temperature profiles recorded during the wetting and drying of the DuraPES®200 membrane using K type (CHAL 001, CHAL 005)) and T type (COCO 001) thermocouples.

The main reason for generally measuring higher temperatures using T type thermocouples is the high thermal conductivity of copper used in this type of thermocouple. As shown in Table 7, the thermal conductivity of copper is approximately twenty times better than for the other alloys listed. The thermal diffusivity is defined as [60]:

$$\alpha = \frac{\lambda_{th}}{\rho\, c_p}, \qquad \textbf{(26)}$$

with λ_{th} the thermal conductivity, ρ the sample density and c_p the specific heat capacity.

Thermal diffusivity is also much higher for copper than for the other alloys. This influences the temperature measurements, both the quantitative values and the profile of the time-dependent temperature characteristic (Fig. 44). Completely wetted membranes show a temperature gradient close to the membrane surface, because the microscope specimen chamber and also the water vapor are at room temperature, while the wetted membrane has a temperature of 4°C (Fig. 45). This results in a heat flux to the thermocouple head via the wires, causing a temperature rise at the head of the thermocouple. The measured temperature is therefore higher than the actual temperature at the membrane surface. This effect is less pronounced for the K type thermocouples due to the much lower thermal conductivity of the alloys used. To confirm this hypothesis, the thempertaure gradient along the wires of the different termocouples was simulated using finite element methods (FEM).

Table 7: Relevant properties of the alloys used for T and K type thermocouples [60].

Material	Thermal conductivity λ_{th} [W/mK] (at RT)	Specific heat capacity c_p [J/kg K]	Thermal diffusivity α [mm²/s]
Constantan®	22.7	390	6.38
copper	401.0	385	112.30
Alumel®	29.2	464	7.34
Chromel®	17.3	450	4.68

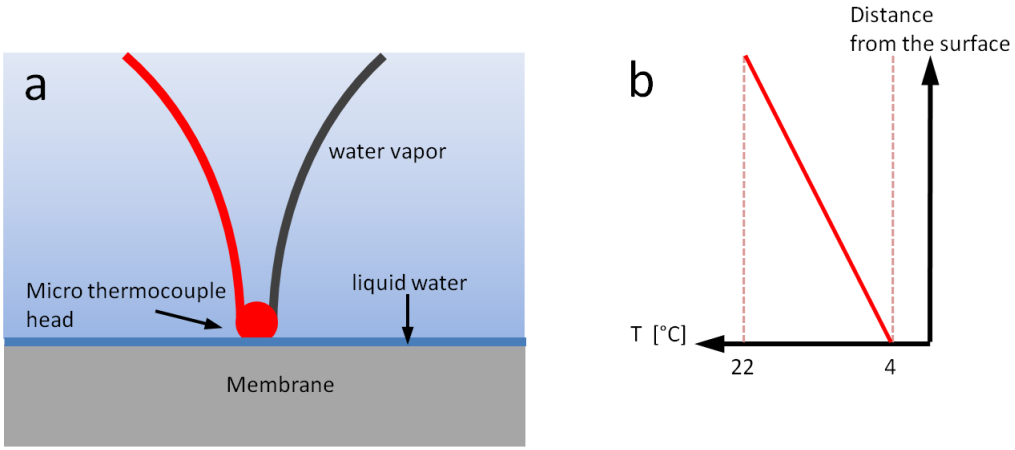

Fig. 45 a: Schematic of thermocouple contacting the surface of the wetted membrane; b: qualitative temperature profile as a function of the distance from the membrane surface

3.3.2.1 Finite element simulations

The exact thermodynamic conditions at the membrane surface are not known in detail. This is due to the permanent pumping process via the PLA (path 2 and 3 - Fig. 18b) and convection of the water vapor, preventing the formation of an equilibrium state above the membrane surface. However, the effect of the thermal conductivity of the thermocouple wires on the temperature measured can be estimated by use of a simplified static thermodynamic model.

A wetted membrane at a temperature of 4°C contacted by the thermocouple was assumed for the simulation. A corresponding model was created using the ANSYS design modeler (see Fig. 46 a).

This corresponds roughly to the real experiment at the state marked in red in Fig. 44. But the influence of the chamber gas was neglected in the simulations. The dimensions for the thermocouple were taken from Table 5.

The dimensions of the membrane were 10 mm × 5 mm × 0.15 mm (not completely shown in Fig. 46a). The membrane material itself was neglected for the simulation of a completely wetted membrane. This is acceptable as the membrane volume porosity is in the range of 75%. Thus only the properties of water were used for the wetted membrane (thermal conductivity of water: 0.019 W/mK). The properties of the contact wires were taken from Table 7. The thermal conductivity of the thermocouple head was defined as an arithmetic mean value of the thermal conductivity of the respective contact wires. The contact area between the membrane and the thermocouple was dot like.

As the distance of the thermocouple head from the support is approximately 3.6 mm (see Fig. 38a) the same value was chosen for the lengths of the simulated wires.

To complete the model and run the simulation, boundary conditions had to be specified. Therefore the temperature at the wire ends was set to 22°C (temperature of the support), and the temperature at the edges of the membrane sheet was set to that of the cooling clamps, namely 4°C.

A more detailed description about FEM using ANSYS can be found in [61]. The results from the static thermodynamic calculations are shown in Fig. 46b and c as well as in Table 8. The calculated

temperature of the thermocouple head is 12.43°C for the T type thermocouple and 5.8°C for the K type thermocouples. Thus the calculated temperature values are higher than the experimentally observed values for both types (Fig. 44). This is due to the neglect of dynamic processes such as convection of the surrounding gas, water flow etc. However, the strong influence of the thermocouple type on the temperature measurement can be clearly seen. As expected, the calculated thermal flux and thus the difference between the measured value of the temperature at the membrane surface and its actual value is highest for the thermocouple with the copper contact wire.

Table 8. Results from the FEM calculation.

	Thermal flux contact wire A [10^5 W/m^2]	Thermal flux contact wire B [10^5 W/m^2]	Temperature at the thermocouple head [°C]	Measured temperature [°C] (Fig. 44)
T type (COCO 001)	11.11 (copper)	0.38 (Constantan®)	12.43	7-10
K type (CHAL 001)	1.40 (Alumel®)	0.75 (Chromel®)	5.80	4.5

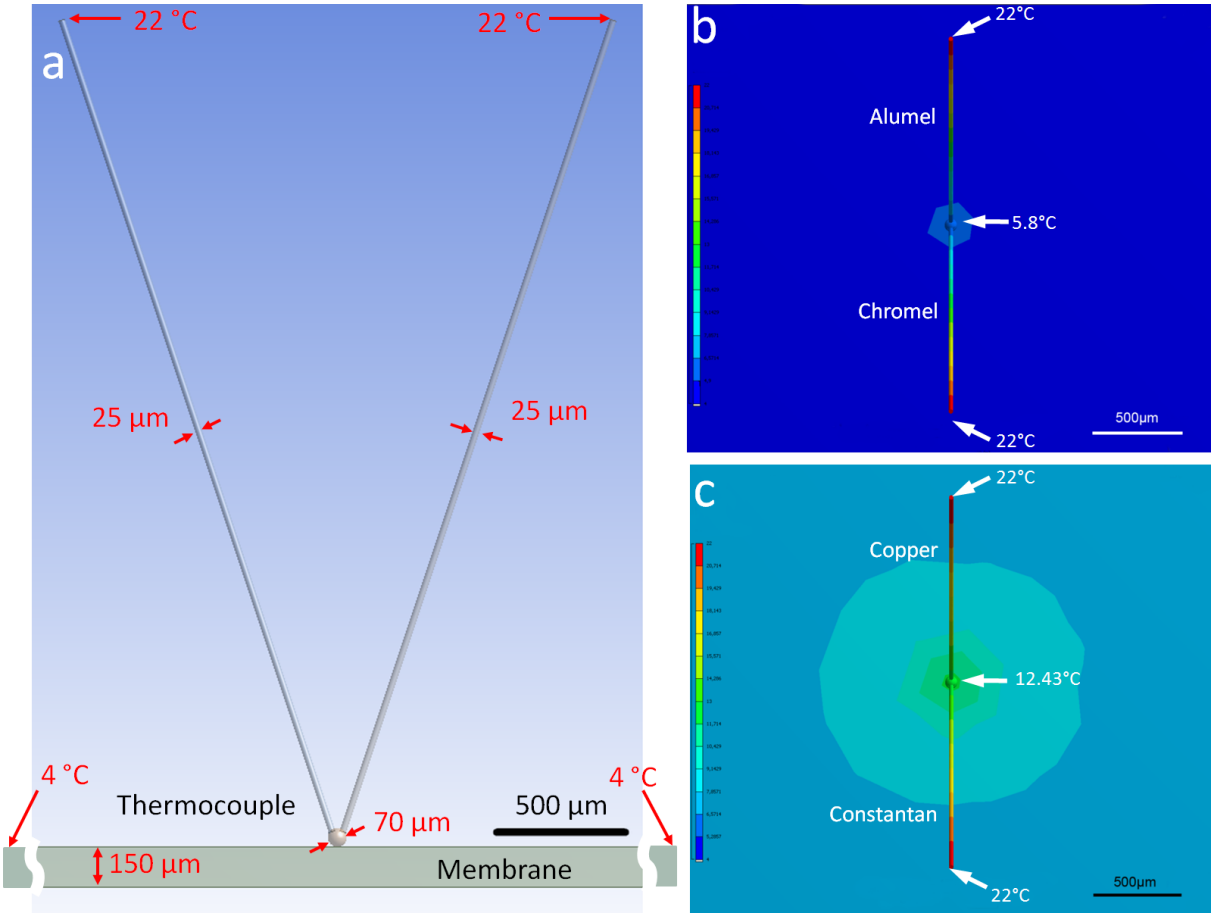

Fig. 46. Thermodynamic analysis of the "wetted membrane - thermocouple" system using FEM simulations. a: model used for the analysis, b: temperature distribution using a K type thermocouple, c: using a T type thermocouple.

The thermal conductivity of copper is not the only problem encountered when using T type thermocouples. As copper is more flexible than Constantan the copper wire bends when the thermocouple is pressed against the membrane surface. As a consequence, sometimes the surface is contacted only by the wire and not by the thermocouple head.

The best and repeatable results were achieved using the smallest K type thermocouples CHAL 0005. All results discussed in the following sections were achieved using this type of thermocouple. Fig. 47

shows the micro thermocouples attached to both membrane surfaces. The DuraPES®450 membrane was mounted in vertical position enabling observation of the drying process of the cross-section discussed in section 5.4.

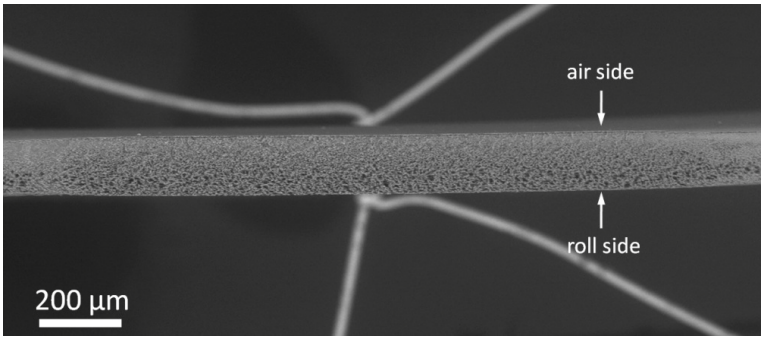

Fig. 47. Cross-section of the DuraPES®450 membrane mounted in vertical position. Two micro thermocouples (CHAL 0005) contact the membrane at both surfaces. The focus plane was set to the membrane cross-section so the thermocouples appear not sharp.

3.3.3 Cycle of the wetting and drying experiment [4]

Before the start of the experiment, the microscope was set to HV mode (sample chamber pressure below 10^{-4} Torr) and the temperature of the cooling clamps was set to 22°C. This ensures a completely dry membrane (see also phase diagram in Fig. 36). Subsequently three purging cycles (see section 2.3.2.2) were performed in order to establish a pure water vapor chamber atmosphere of 1 Torr [62]. For this purpose the chamber pressure is changed several times between 1 and 8 Torr. After the last pumping cycle a stable water vapor atmosphere is reached, which forms the initial state of the experiment (Fig. 49 - period A).

At the start of the experiment the temperature of the cooling clamps was set to 4°C and the pressure in the specimen chamber to 1 Torr. The heat conductivity of the membrane is extremely poor. The decrease in temperature at the membrane surfaces (midway between the clamps where the thermocouples are placed) from room temperature (22°C) to approx. 18°C is thus caused only by the thermal conductivity of the water vapor atmosphere. This was verified by temperature measurements at different distances to the cooled clamps at a water vapor pressure of 1 Torr at the level of the membrane, but with the membrane itself removed (Fig. 48).

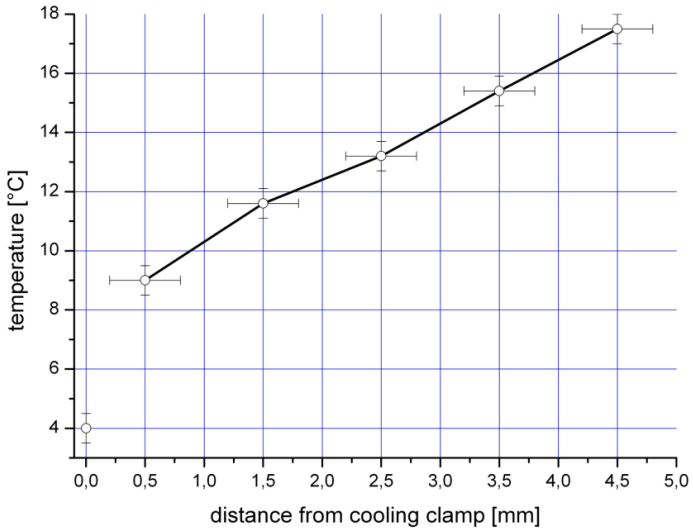

Fig. 48. Temperature as a function of the distance from the cooling clamp, measured at 1 Torr water vapor atmosphere at the level of the membrane, but membrane removed.

A thermally stable state is reached after around 160 seconds (Fig. 49 - period B). Then the wetting process is initialized by increasing the water vapor pressure from 1 Torr to 6 Torr (Fig. 49 - period C), which is above the dew point of water at this pressure.

As a direct consequence of the pressure jump, water condenses at the cooling clamps and begins to penetrate into the membrane structure. The membrane surface temperature decreases, but no water is visible in the surface pores (Fig. 49a*), indicating that only the small pores of the inner separation layer are filled with water (Fig. 49 - period D). The temperature of a wet membrane is mainly determined by its water content, due to the fact that the volume of water is much greater than that of the membrane matrix (see section 4.4.2 below), and that water has a much higher heat capacity (4.19 J/g) than polyethersulfone (1.45 J/g) [36]. At the end of period D both membrane surfaces are getting wet and the temperatures reach a stable value (period E, Fig. 49b*). As the water condensation at the cooling clamps is stochastic, the wetting (slope at period D) of the membranes is not exactly repeatable. For this reason and because wetting occurs not through the surface but through the membrane cross-sections, which is not the case in normal operation, the final discussion will concentrate on the drying process. However, the final temperature indicating a wet and stable (equilibrium) state of the system always reaches the same value (approx. 4°C) when the experiment is repeated. This value indicates an accurate temperature measurement, as the thermal equilibrium at 6 Torr is at that temperature value (see also Fig. 36). After 560 seconds, the drying process is initialized by reducing the pressure from 6 to 3.5 Torr (Fig. 49 and see also Fig. 36), which is below the dew point. Evaporation of water at the membrane surfaces starts and the resulting evaporation heat causes the surface temperatures to fall to –2°C. The membrane surface is still covered with water during period F (Fig. 49c*). At the beginning of period G the pores start to dry, followed by a subsequent increase in surface temperature, which is also an indication of the presence of dry large pores beneath the surface of the roll side.

The drying of surface pores on the roll side during period G can be seen very clearly (Fig. 49d*-f*). The resulting images allow the measurement of the number and size distribution of the dry pores as a function of time. During period G a dry membrane surface becomes visible, but the temperature has not yet reached the starting value, which is clear evidence that water is still present inside the membrane, mainly in the separation layer with its many small pores and narrow pore size distribution. In period G (at the temperature plateau) the separation layer and other small pores in the rest of the membrane are still drying. Once the rest of water inside the smallest pores has vanished the surface temperature increases very rapidly (Fig. 49 - period H) to the value measured at the end of period B. The shape of the characteristics at period G and the slope at period H as well as the break point positions vary for membranes with different structures but are characteristic of each membrane type. This will be discussed in more detail in section 5.3. In combination with the images from the membrane surface, the temperature measurements provide information about the drying behavior not only at the surface but also inside the membrane. Finally, the temperature of the cooling clamps was set to the starting value of 22°C, and the temperature at the membrane surface also returned to the starting value (Fig. 49 - period K).

As can be seen from Fig. 49, the temperature characteristics for the two membrane surfaces differ from each other, which is due to the asymmetry of the membrane structure. Repeating the experiment with the membrane turned upside down produced nearly the same results. The temperature characteristics are discussed in detail in section 5.3.

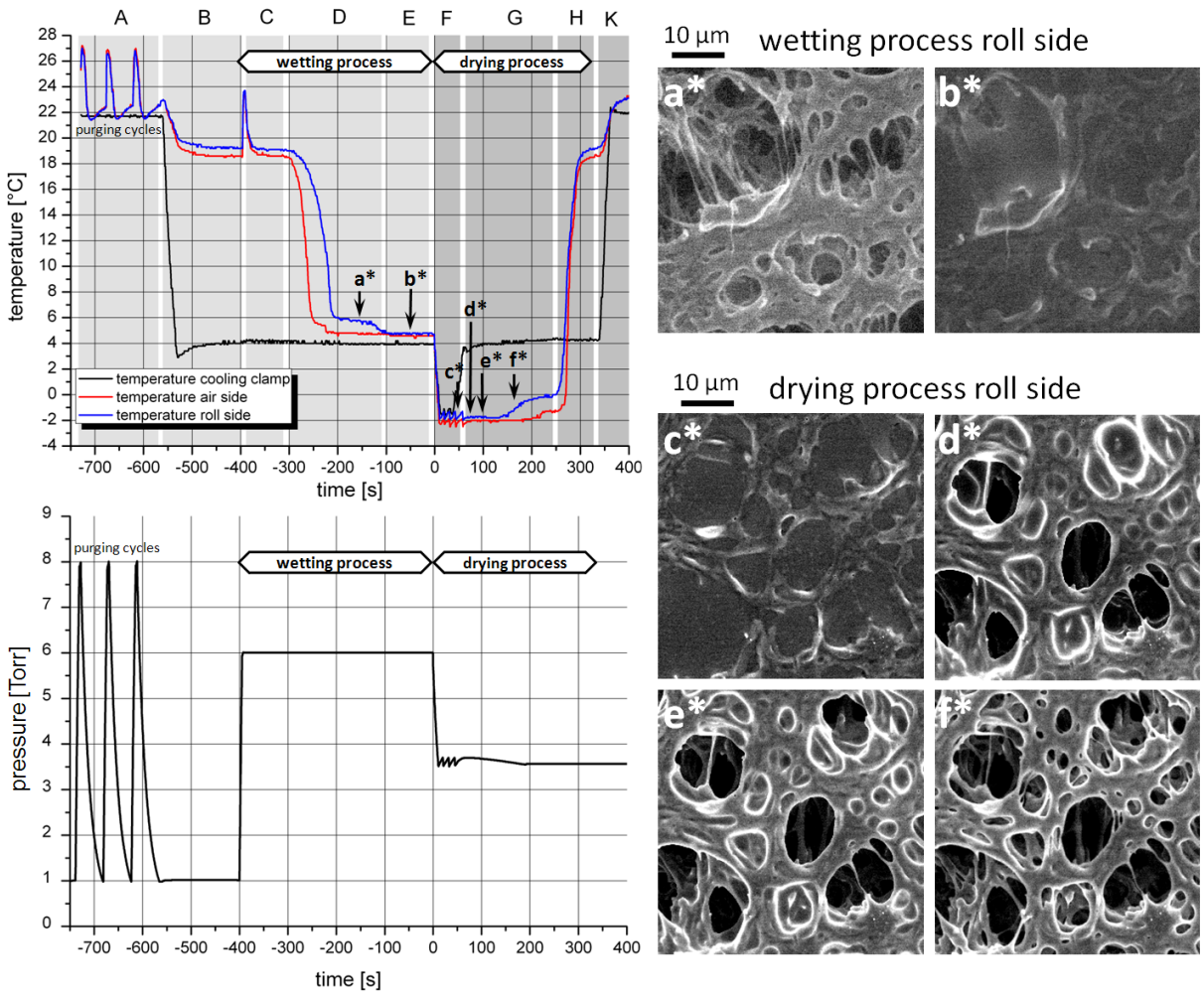

Fig. 49. Left: Temperature characteristic (top left) and chamber pressure (bottom left) recorded during the drying and wetting of the DuraPES®600 membrane, right: images of the membrane surface recorded during drying and wetting, with the times marked in the temperature characteristic on the top left: a: dry state of the membrane surface, b*: fully wetted membrane surface, c*: wet state at the beginning of the drying process, d*-f*: drying of the pores; adapted from* [4].

The drying of the membrane can only start after the cooling clamps themselves have dried. As long as they are wet the membrane will also stay wet because water is drawn into the membrane due to capillary forces. Therefore the wetting and drying behavior of the cooling clamps was also investigated. The SEM images in Fig. 50a-k document the condensation and evaporation of water at one of the cooling clamps, with the temperatures at the surfaces of the respective cooling clamp and the membrane shown in the top right diagram of Fig. 50. The condensation of water started immediately after increasing the pressure to 6 Torr (Fig. 50b). The SEM images in Fig. 50c-e document the droplet formation at the cooling clamp. In the same period the membrane surface temperature began to decrease until it reached almost the same temperature as the cooling clamp. The SEM images in Fig. 50e-k document the drying of the cooling clamps. 40 - 50 seconds after the pressure decrease the surface of the cooling clamp is already dry (Fig. 50j and k). This confirms that the cooling clamps have to be completely dry before the surfaces of the membrane start drying (compare points in time of Fig. 49d* and Fig. 50j). During the wetting process of the cooling clamps water flows from the cooling clamp to the membrane. This flow stops when the cooling clamps have dried completely, initiating the drying process of the membrane.

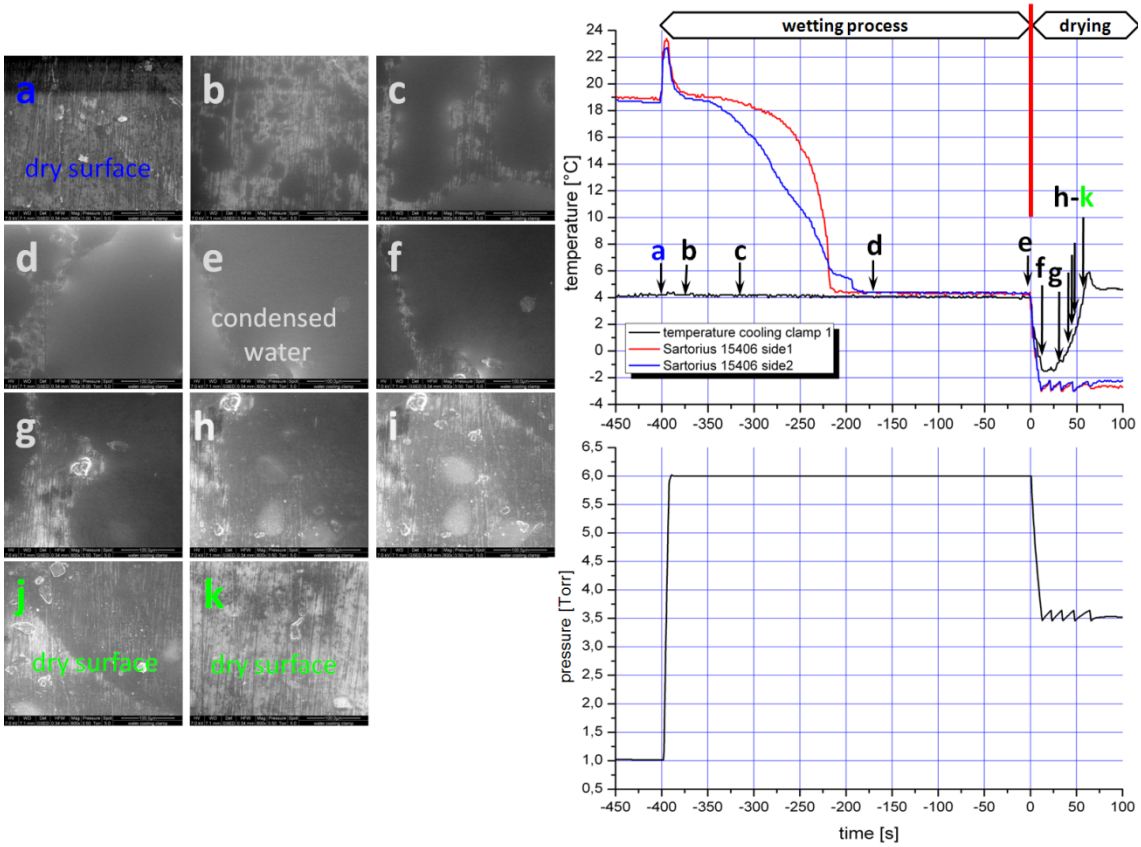

Fig. 50. Wetting and drying of the cooling clamps. Left: a: dry surface of the cooling clamp at the beginning of the experiment, b: start of water condensation at the cooling clamp, c-e: further condensation of water at the cooling clamp, f-i: vaporization of the water, j-k: dry cooling clamp. Right, top: temperature at the membrane surface, bottom: chamber pressure.

3.4 **Image processing**

Most SEM images recorded are not directly usable for image analysis. Segmentation of the raw images is hardly possible without preceding image processing due to image noise, low contrast or charging artifacts.

Segmentation is necessary, however, in order to obtain binary images for 3D reconstruction or feature analysis. As the segmentation process has a strong impact on the resulting data, image preprocessing (noise and background filtering) is very important. The present work often required manipulation of a whole stack of images using MATLAB scripts. 3D reconstruction was performed using the software package AVIZO®Fire, which also enables the calculation of morphological parameters such as specific surface area, or volume porosity. To determine the paths along the pores through the membrane structure a 3D distance transformation of the binary image stack was applied. AVIZO®Fire 7.0 also offers the calculation of the absolute permeability of the reconstructed porous structure and the maximal possible trans-membrane flow (TMF).

AVIZO®Fire also features an alternative segmentation editor, which allows segmentation of the images by region growing. This feature was used for semi-automatic segmentation of dry pores visible in images recorded during the wetting / drying experiments. The respective results are presented in section 5.2.

3.4.1 Background filtering and segmentation [3]

Changes in the brightness of the background of the images can be caused by charging artifacts, as already mentioned in section 3.2.2. But an inhomogeneous background can prevent a reliable segmentation. The affected image stacks were thus first filtered by a median filter to remove noise; an open filter [63] was subsequently used to get rid of the inhomogeneous illumination. The result of the open filtering is an image of the inhomogeneous background only (Fig. 51b), which can be subtracted from the original image (Fig. 51a). Afterwards, the images are transformed into binary images via threshold segmentation (Fig. 51c and d). The threshold level was calculated by Otsu's method [64]. This method calculates the optimal threshold level on the basis of the image histogram featuring a bimodal structure. As the contrast between the bright membrane matrix and the dark resin is sufficiently high, the histogram shows a very clear bimodal structure, and so the threshold level is uncritical. A description of this procedure can also be found in [63]. The final stack of binary images of the backup layer and the membrane surface was then used for the creation of a 3D model using AVIZO®Fire (see section 4.3).

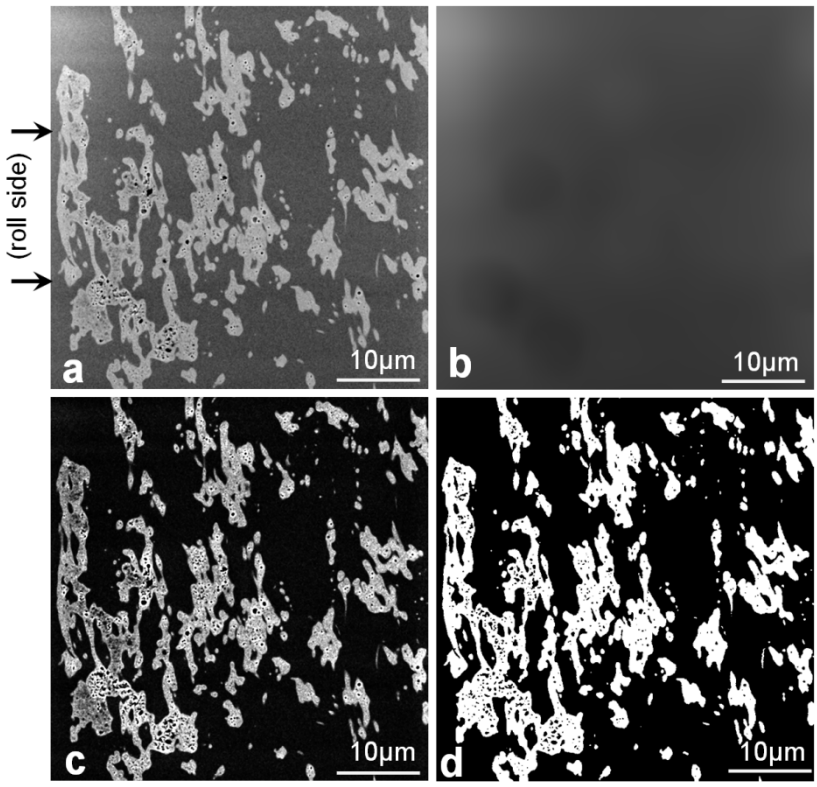

Fig. 51. a: Backup layer of the DuraPES®450 membrane including the roll side; b: background of image a after open filtering, c: image b subtracted from image a, d: image after threshold segmentation of image c; adapted from [3].

Conventional threshold segmentation has a global effect on the whole image. For segmentation of particular regions, the conventional threshold segmentation method was therefore replaced by region growing segmentation [63,65]. First seed pixels had to be marked manually (red crosses in Fig. 52a). The region growing algorithm selects the largest connected area that contains the seed pixel itself and all pixels with gray values lying inside a user-defined range. That method allows dry pores, which due to shadow effects appear darker than the pores still filled with water to be reliably segmented. Unwanted dark areas are not marked with seed pixels and are therefore not segmented - red arrows in Fig. 52b.

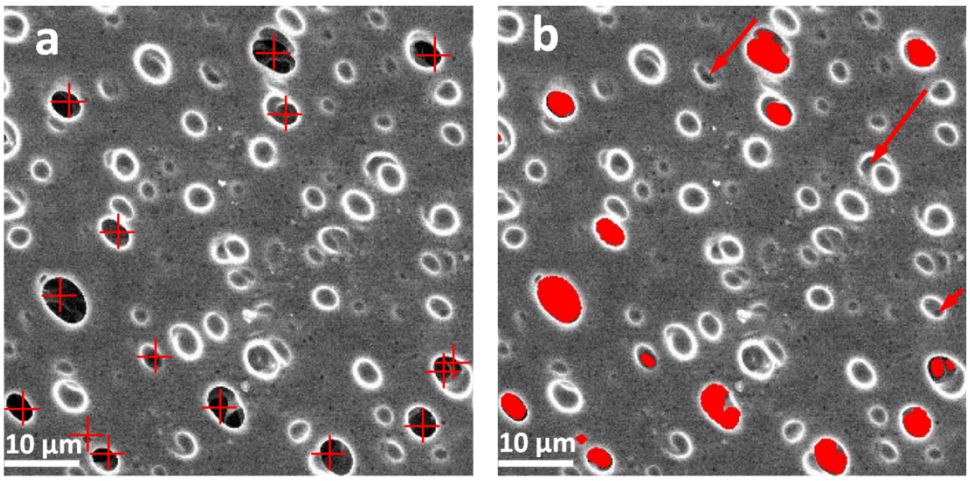

Fig. 52. Segmentation with region growing segmentation. a: Seed pixels are marked with red crosses; b: segmented pores (red areas) and not segmented pores (red arrows).

3.4.2 Noise filtering

Shorter dwell times are required to avoid irradiation damage of the specimen, especially at high magnifications. This leads to noisy images, which are not directly usable for threshold segmentation due to peak broadening in the histogram (Fig. 53a and c). An adaptive nonlocal filter was therefore used for noise reduction [66]. In contrast to conventional linear filters, this filter takes care of the local extremes. The filter changes the pixel gray levels to values which are more representative of the region to which they belong. Pixels located at the border of two regions, however, are not representative of either. A gray level value which is offset to the interior region is used in this case. The offset and offset direction are calculated using a vector field described in more detail in [66]. The resulting image looks “pre-segmented” and shows a clear bimodal histogram (Fig. 53b and c), which makes further threshold segmentation much easier.

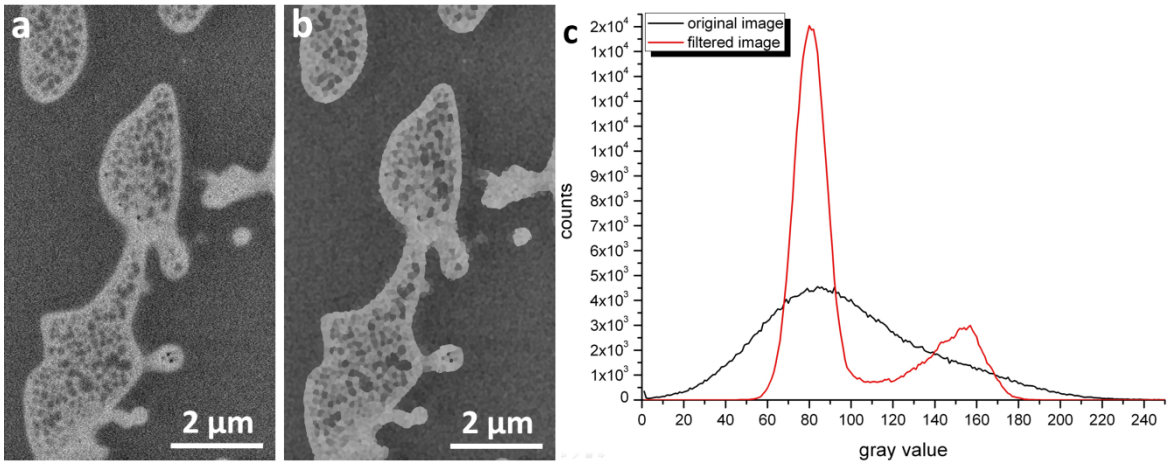

Fig. 53. Effect of the adaptive nonlocal offset filter. a: original image of the sub-porous structure of the DuraPES®600, b: adaptive nonlocal offset filterd image, c: histograms of images a and b.

3.4.3 Feature analysis

Morphological parameters of the segmented areas (features) can be analyzed using the MATLAB imaging processing toolbox. The equivalent diameter of each segmented pore was calculated for each image. The equivalent diameter is the diameter of a circle with the same area as the pore at the membrane surface [5]. In this way, the pore size (equivalent diameter) distribution can be obtained for each image (the results are documented in section 5.2).

4 The 3D structure of microfiltration membranes

The present work delivers static (morphological) as well as dynamic (behavior in the presence of water) information about the membrane. The first part will deal with the analysis of the membrane structure using both 2D images and 3D reconstructions.

The specific surface area, volume porosity, connectivity, distribution of the lengths and diameters of the pores as well as the tortuosity are decisive parameters determining membrane filtration performance. Because of the asymmetric structure of the membranes these parameters vary along the cross-section. This provides the basis for computing profiles of parameters listed in Table 9 as a function of the distance from the surface. The 3D reconstructions were also used for fluid simulations as described in section 4.4.4.

4.1 The asymmetric membrane profile

To obtain a profile of a certain parameter along the cross-section of the membrane the respective parameter values had to be calculated at different positions of the cross-section. For this purpose the membrane cross-section was divided into *"local"* sections. Within each section an average value of the parameter of interest was determined. The parameters which were actually calculated in this work are listed in Table 9.

As certain parameters change very strongly at the interface between the support and the separation layer, the profiles also allow the determination of the position and thickness of the different layers (e. g. support and separation layer).

The mean free path length parallel as well as perpendicular to the flow direction is introduced for the 2D case. The mean free path length in flow direction is the mean length which a particle can move before it must stop at a pore wall. The mean free path length perpendicular to the flow direction limits its size.

The idea of the mean free path length was introduced by Ziel et *al.* [8]. They used single TEM images of the membrane cross-section for obtaining a profile of the mean free path length perpendicular to the flow direction as well as the fraction of the pore area. This fraction is defined as the ratio of the pore area (dark appearing resin) to the total area of the respective section, and can be used to estimate the actual local volume porosity (in 3D). A homogeneous and isotropic structure is a pre-condition for this approach. In this case the principle of Delesse is valid [67]:

$$p_A = p_V, \qquad (27)$$

with p_A the fraction of the pore area (2D) and p_V the volume porosity (3D).

Although the membrane structure is extremely asymmetric along the cross-section, isotropy can be assumed within a certain *"local"* section if the sectioning is chosen properly and the section thickness is small enough. The results presented in section 4.4.2 show that the approach is appropriate.

As the membrane resistance increases with increasing inner surface area due to the flow friction of the fluid at the pore walls, the specific inner surface area can be used as a quantitative parameter for the membrane resistance, which is much more difficult to calculate. But both parameters were calculated in this work and in fact show the same quantitative behavior. The results and further discussion can be found in sections 4.2 and 4.4.4.

Table 9. Membrane parameters determined from both 2D images and 3D reconstructions.

2D	3D
Mean free path length parallel to the flow direction (see Fig. 54a)	Volume porosity: p_V ((28), see section 4.4.2)
Mean free path length perpendicular to the flow direction (see Fig. 54b)	Specific surface area: $A_{spec.}$ ((29), see section 4.4.2)
Fraction of the pore area: p_A ((30), see section 4.2)	Membrane resistance: R_m (see section 4.4.4)
	Pore connectivity (see section 4.4.1)
	Pore diameter (see section 4.4.1)
	Tortuosity (see section 4.4.3)

$$p_V = 1 - \frac{V_{Polymer}}{V} = \frac{V_{Pore}}{V}, \quad \textbf{(28)}$$

with $V_{Polymer}$ the volume of the membrane matrix, V_{Pore} the pore volume and V the section volume.

$$A_{spec.} = \frac{A_{Polymer}}{V}\ [\mu m^{-1}], \quad \textbf{(29)}$$

with $A_{Polymer}$ the inner surface and V the section volume.

$$p_A = \frac{A_{Pore}}{A}, \quad \textbf{(30)}$$

with A_{Pore} pore area and A the section area.

4.2 Parameter profiles obtained from 2D images

The profiles of the mean free path length were measured perpendicular as well as parallel to the membrane surface as shown in Fig. 54. The red lines in Fig. 54a mark the *"local"* sections. The mean length of the white horizontal lines gives the free path length in flow direction. The mean path length was calculated at intervals of 10 µm for each investigated membrane; the corresponding profiles are shown in Fig. 56a-c.

To calculate the mean free path length perpendicular to the flow direction, the membrane cross-section was also divided into equidistant sections as shown in Fig. 54b. The white vertical lines in the leftmost section represent the local free path length perpendicular to the flow direction. The mean value of all possible lines within the red marked section give the mean path length perpendicular to the flow; the resulting profiles are shown in Fig. 56d-f. A comparison of the different profiles shows that the mean free path length perpendicular to the flow direction is smaler than that parallel to the flow direction. This is an indication of a non-isotropic membrane structure. As a consequence the Delesse principle is not valid exactly, but is nevertheless a good approach, as will be demonstrated in section 4.4.2 below.

Two general problems concerning microscopic characterization and subsequent image processing should be discussed at this point:

- variations of the membrane parameters along the membrane sheet
- influences of the gray value chosen for thresholding

In a first step, 4 images of the cross-section (insert in Fig. 55 section 1 - 4) were recorded at different positions (at several cm intervals) of the membrane sheet (MicroPES®4F). The respective histograms show nearly the same characteristics and a gray level threshold of 100 was found for all 4 sections using Otsu's method [64]. The profiles of the free mean path lengths show almost no variations (Fig. 56a). Thus the membrane structure seems to be very homogeneous across the whole sheet.

Different threshold values were used for the segmentation of the image of one cross-section of the Sartorius 15406 membrane. A threshold level of 106 was found using Otsu's method. Two further threshold levels below (90) and above (122) this value were also used for segmentation. The differences in the resulting characteristics for the mean free path length parallel to the flow direction are shown in Fig. 56c. Strong variations of the threshold value cause relatively modest variations in the resulting parameter profiles. This is due to the clear bimodal histogram structure. For all other profiles presented in Fig. 56 Otsu's method was used to determine the threshold value used for segmentation.

The mean free path length profile parallel as well as perpendicular to the flow, as expected, shows a minimum at the separation layer for all studied membranes (Fig. 56a-c and d-f). In contrast, the profile of the fraction of the pore area shows no minimum at the separation layer for the DuraPES®450 membrane (Fig. 56h). This result was verified later on by measuring the volume porosity profile in 3D (see Fig. 65h below). However, a minimum of the porous fraction area profile at the separation layer was found for the Sartorius 15406 and MicroPES®4F membranes (Fig. 56g and i). But one must be aware that the surface layer at the two outmost sections, whose structure can differ from that of the interior, might distort the results. The results from these two layers could possibly be improved by choosing the boundaries of the respective sections close below the surface.

Because of the strongly asymmetric pore structure only few pores are visible on the roll side of the DuraPES®450 membrane, resulting in low statistical significance of any calculated values. Therefore calculations for the DuraPES®450 membrane were only performed to a depth of 90 µm (starting from the air side).

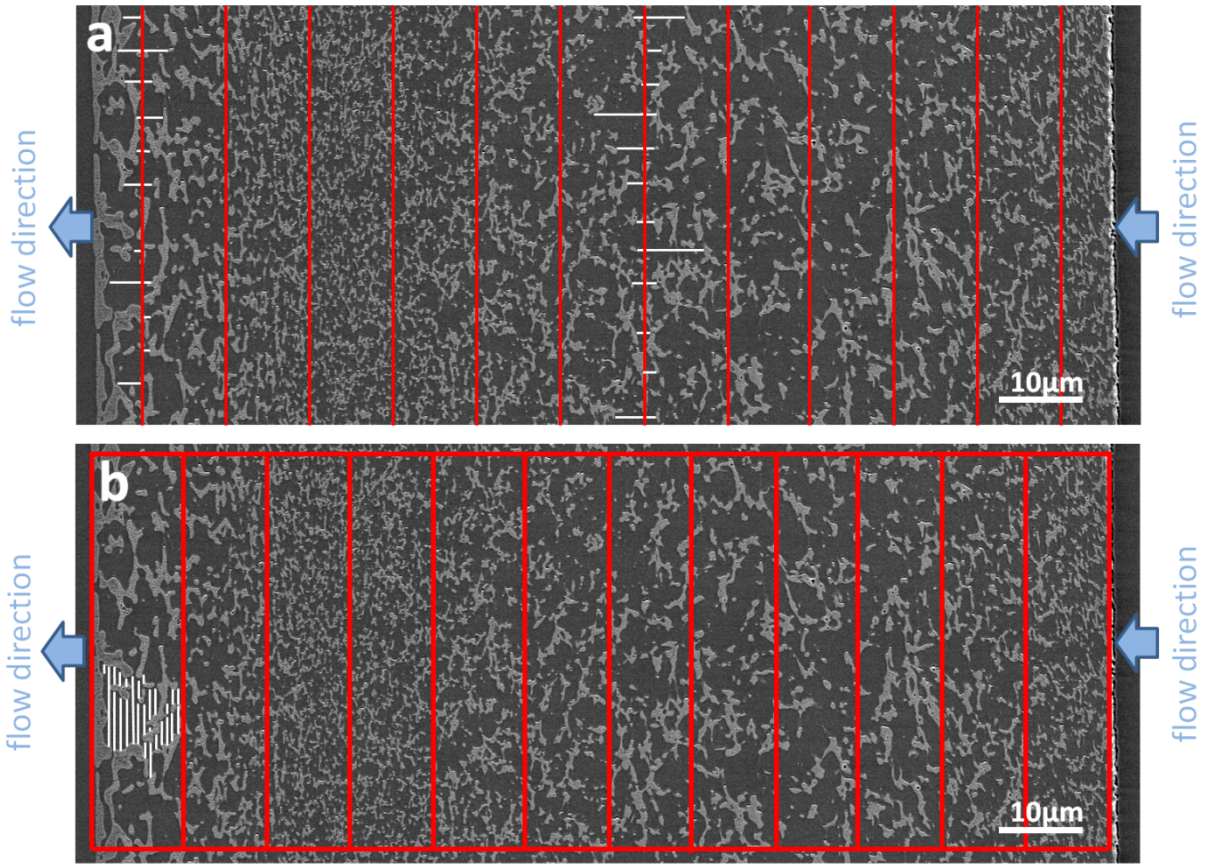

Fig. 54. Sketch of the determination of the 2D path length for the MicroPES® 4F membrane. a: parallel to the flow direction; b: perpendicular to the flow direction. White lines represent the local free path length parallel and perpendicular to the flow direction.

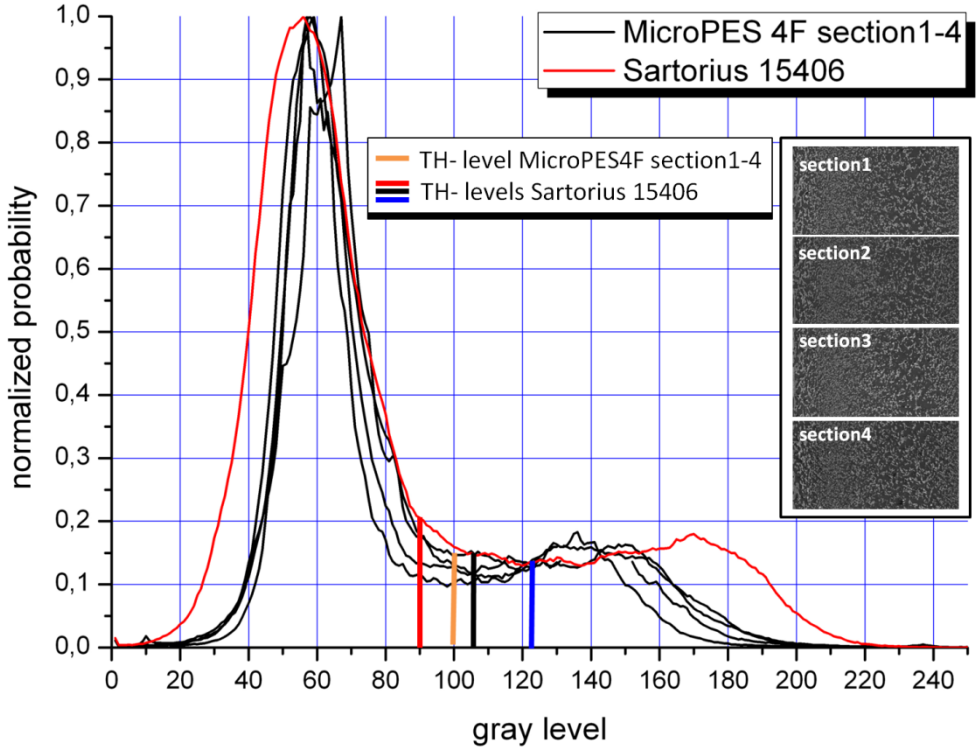

Fig. 55. Histograms of the cross-sections images of the MicroPES® 4F (sections1 - 4 - inserted) and Sartorius 15406 membrane. The threshold levels used for segmentation are marked.

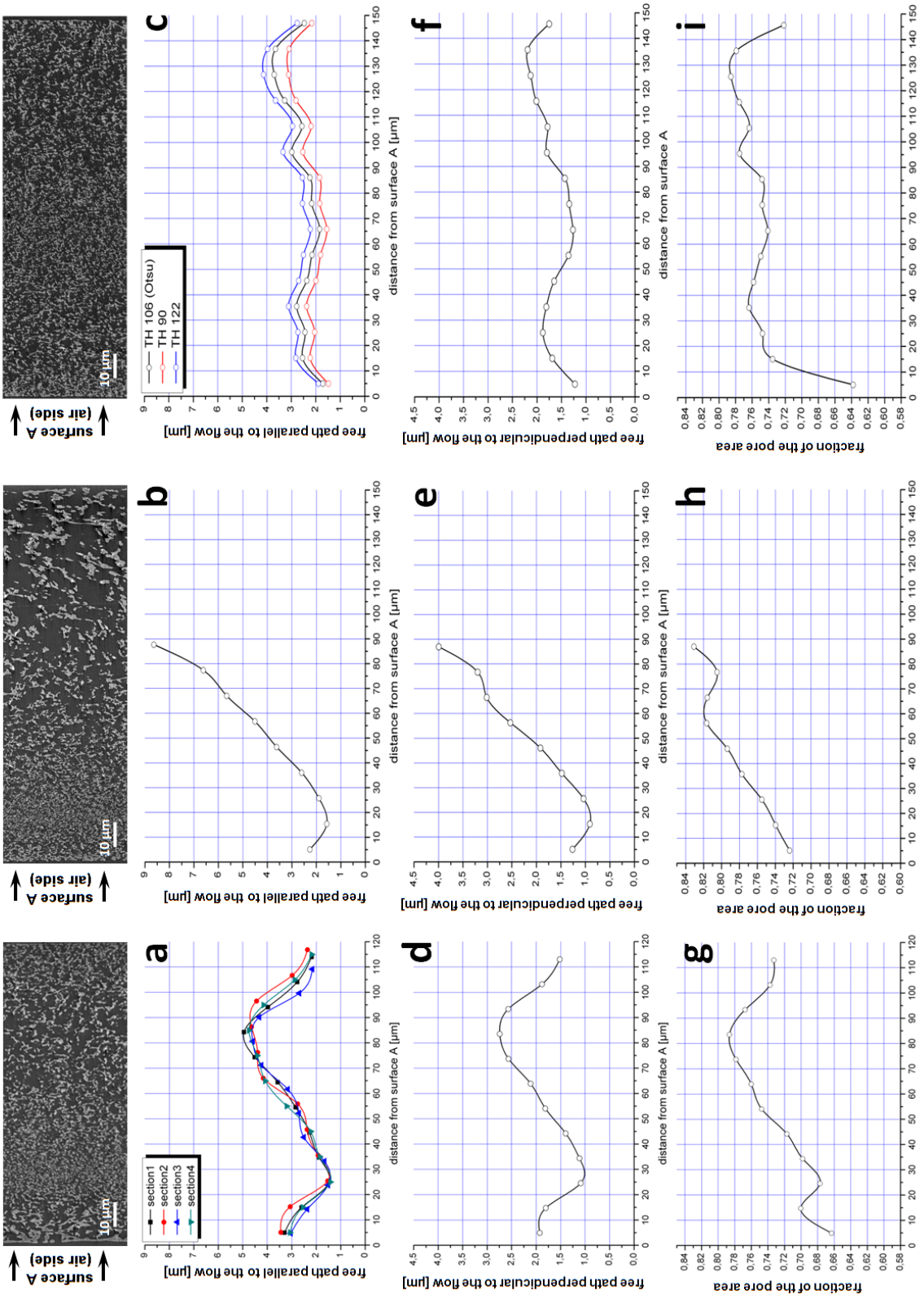

Fig. 56. Profiles of the free mean path lengths across the cross-section for the MicroPES®4F, DuraPES®450 and Sartorius 15406 membranes, determined from 2D images. a-c: mean free path lengths parallel to the flow direction; d-f: mean free path lengths perpendicular to the flow direction; g-i: fractions of the pore area. The 4 characteristics in Fig. 56a result from 4 different cross-sections. The 3 characteristics in Fig. 56c were calculated with 3 different threshold levels.

Single cross-section images can give quantitative information about the membrane asymmetry. Parameter profiles from the fraction of the pore area or the free mean path length are useful approaches for parameter profiles which in fact can only be obtained with high accuracy from 3D reconstructions. The resulting curves indicate the position of the different membrane layers and can additionally give an value for the width of these layers.

4.3 3D reconstructions

The full 3D reconstruction of the membrane structure required stacks of images of the complete cross-section (width 120 - 150 µm), necessitating a tradeoff between image resolution and size, acquisition time, and beam current. The resolution for image recording depends on the minimal size of the membrane structures. As the pore structure at the separation layer of the membranes investigated is in the 100 nm range the image pixel size must be at least a factor of two smaller. As a consequence pixel sizes of 25 to 30 nm were used for image recording of the membrane separation layers. Detailed studies of the sub-porous structure (smaller than 100 nm) at the DuraPES®600 surface required even smaller pixel sizes of 7.5 to 12 nm. Excessive dwell times lead to beam damage as shown in Fig. 71b. The big pores of the backup layer at the DuraPES®450 roll side, on the other hand, allow pixel sizes up to 160 nm.

Recording the whole membrane cross-section in one step at full resolution leads to long image acquisition times, which may result in stability problems during the serial sectioning and imaging procedure. To overcome these problems the complete membrane cross-section was divided into 3 sections (see Fig. 57) for each of which a separate image stack was recorded. Each section thus corresponds to an image stack (Stack#1 - Stack#3), with the stacks recorded successively. The position of the image stacks within the sliced membrane volume is sketched in Fig. 57. This is possible because the membrane is homogeneous and isotropic in z-direction. Irregularities of the interfaces between the stacks were neglected because the maximum volume of one 3D reconstruction (width 10µm) was still smaller than one of these 3 sections.

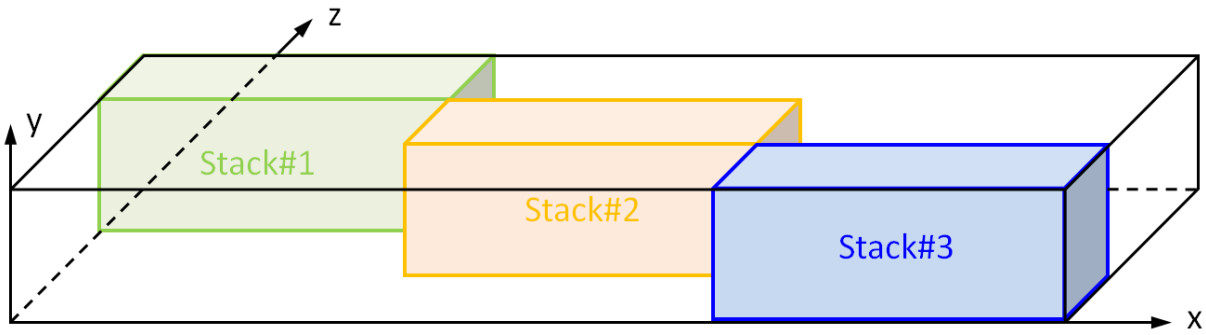

Fig. 57. Sketch of the position of the image stacks within the sliced membrane volume; the xy plane corresponds to the image plane. The membrane surfaces are parallel to the yz plane.

The numbers of images, the image resolution, and all important microscope recording parameters as well as the applied image processing tools are listed in Table 10. Pixels are called “voxels” in 3D context. The image resolution determines the voxel dimension in x and y direction, while the z direction indicates the slice thickness (see also Fig. 33). The voxel size, the image resolution as well as the number of the recorded slices determines the dimensions of the stacks.

4.3.1 Recording of the image stacks

In the case of the Sartorius 15406, the membrane cross-section with a width of 150 µm was divided into 3 sections (Fig. 58) of approximately 50 µm each. As explained above and shown in Fig. 58 - Fig. 60, the images of each stack were subdivided into further sections used for the calculation of parameter profiles. The whole cross-section of the Sartorius 15406 membrane was thus divided into 15

sections. As also shown in Fig. 58, the images of the outer two stacks stretched across the boundaries of the membrane and contained small strips of the resin in which the membrane was embedded (marked with a white *). This was necessary because otherwise part of the membrane boundary region could have moved out of the field of view due to sample drift during the slicing and imaging procedure. However no significant sample drift was observed.

The same stack sizes were also used for the MicroPES®4F membrane. The smaller thickness of only 120 µm, however, led to a stack-overlap as illustrated in Fig. 59. As a consequence only the two core sections of Stack#2 were used to complete the whole parameter profile.

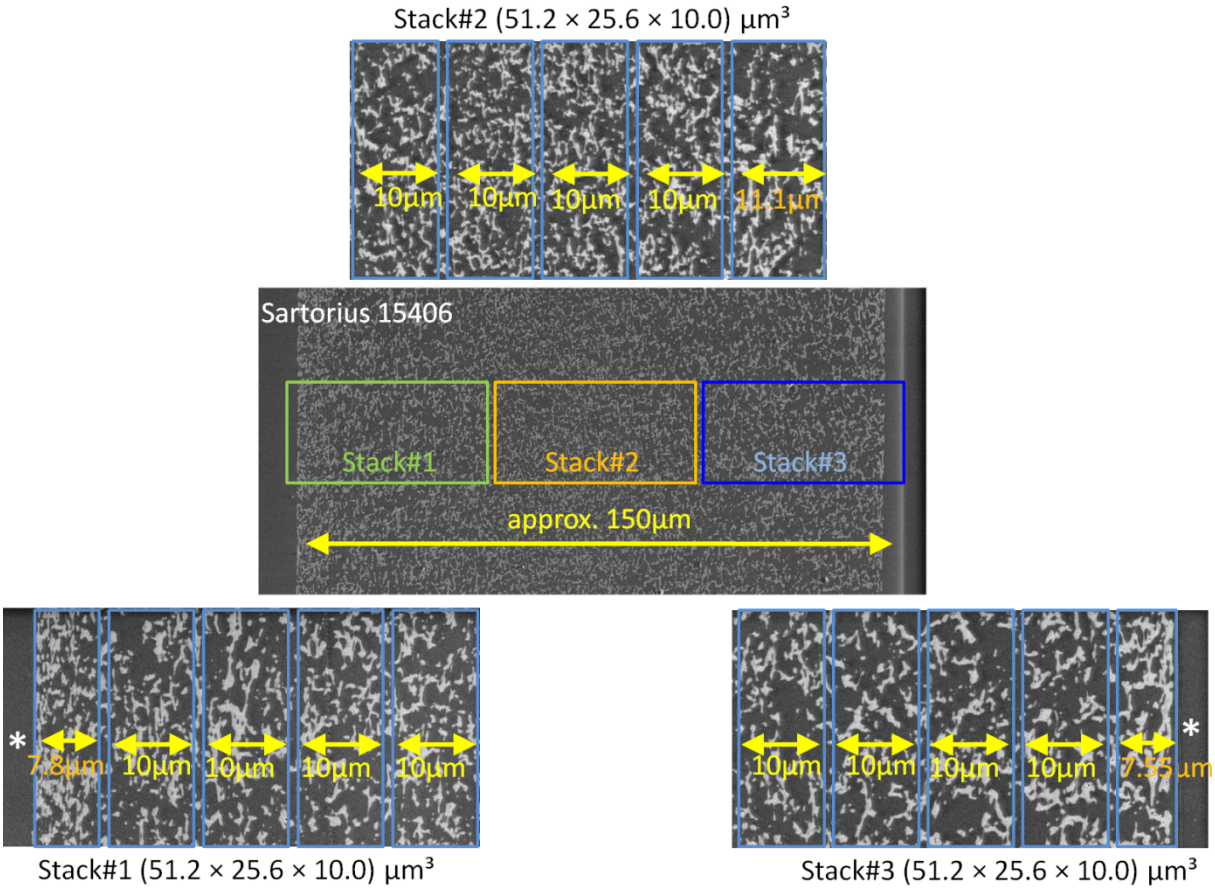

Fig. 58. Illustration of the division of the cross-section of the Sartorius 15406 membrane. The image at the centre shows the positions of the three image stacks recorded successively. The other three images show the division into subsections (by image processing) for the calculation of the profiles of various parameters across the cross-section.

Because of the strong asymmetric structure of the DuraPES®450 membrane 3 stacks of different resolutions and sizes were recorded (Fig. 60). After each cut the complete membrane cross-section was first recorded at low resolution (pixel size 160 nm - Stack#1). As the resolution of Stack#1 was definitely too low to image the fine structures of the separation layer, this layer was subsequently recorded with a smaller pixel size of 25 nm (Stack#3). Finally the images belonging to Stack #2 were recorded. Only the images of Stacks#2 and #3 were used for the calculation of the parameter profiles. Due to the small number of very big pores in the backup layer on the roll side no statistically significant parameters could be calculated from this part of the membrane.

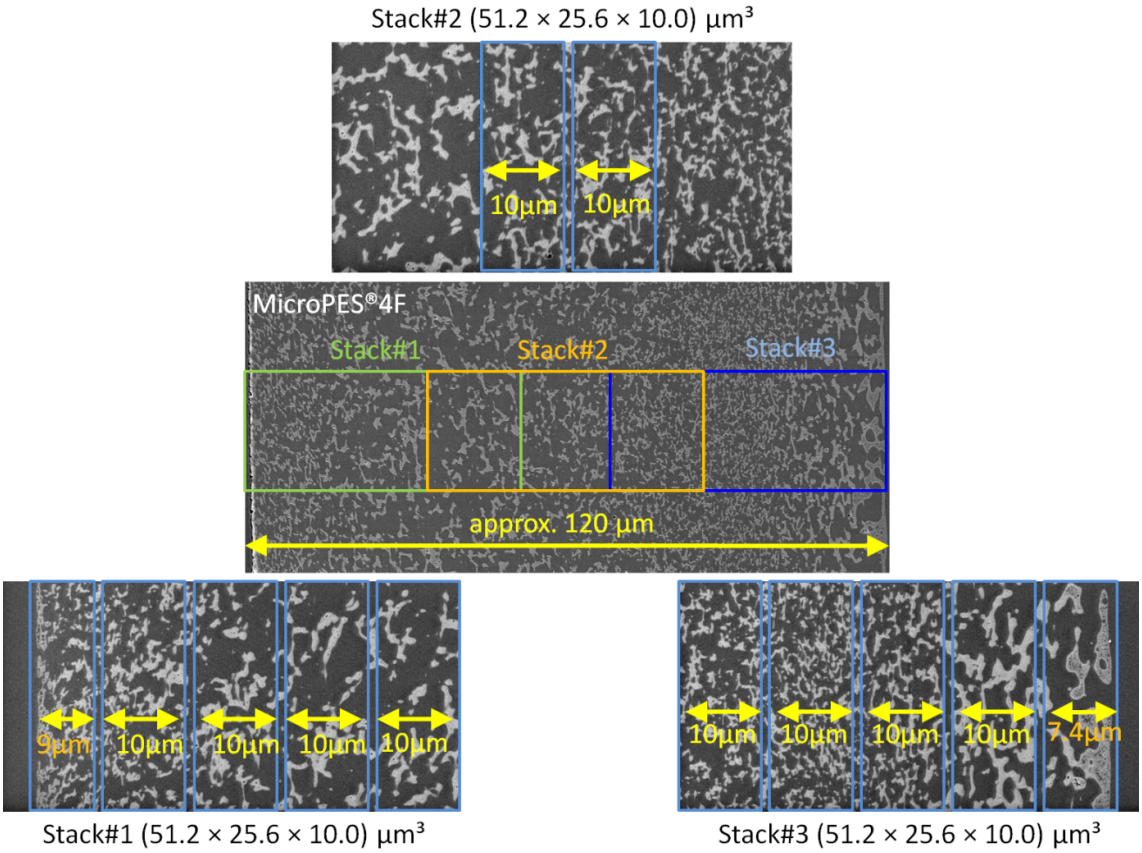

Fig. 59. Illustration of the division of the cross-section of the MicroPES®4F membrane. The image at the center shows the positions of the three image stacks recorded successively. The other three images show the division into subsections (by image processing) for the calculation of the profiles of various parameters across the cross-section. The images at the center overlap with those outside.

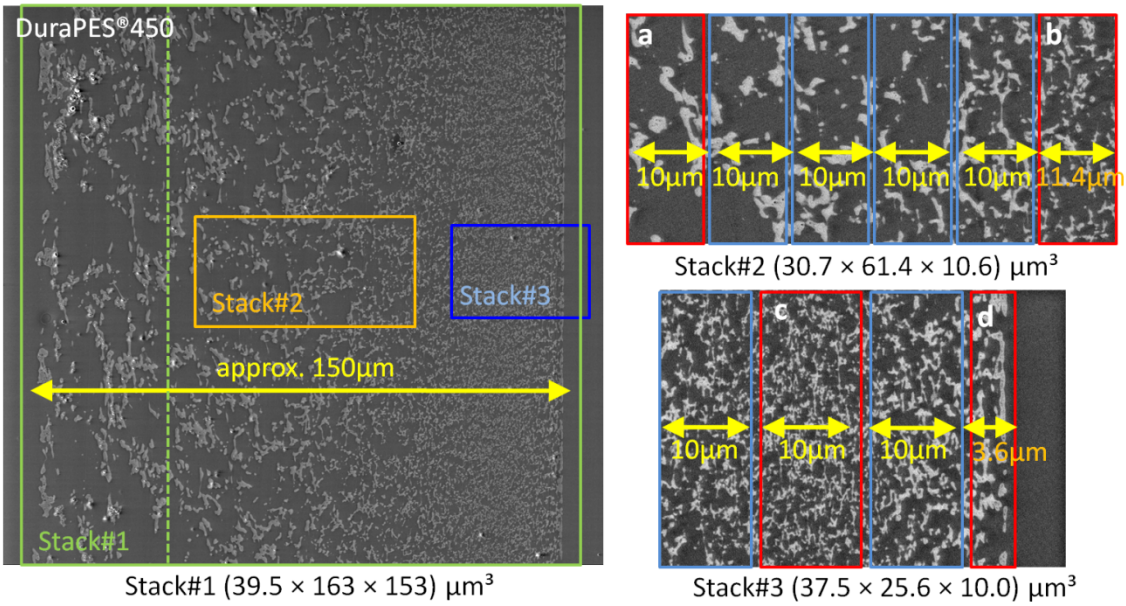

Fig. 60. Illustration of the division of the cross-section of the DuraPES®450 membrane. The image at the left shows the positions of the three images recorded successively. The images in Stack#1 comprise the whole cross-section. The two images at the right show the division into subsections of the images from Stack #2 and #3 (by image processing) for the calculation of the profiles of various parameters across the cross-section. The area to the left of the dashed line contains only very few big pores and was not used for the calculation of parameter profiles. The sections a - d were used for a 3D visualization of the inner membrane structure (see Fig. 62 below).

Table 10. Parameters used for 3D reconstruction of the membranes

	MicroPES®4F Stack#1-3	Sartorius 15406 Stack#1-3	DuraPES®450 Stack#1	DuraPES®450 Stack#2	DuraPES®450 Stack#3	DuraPES®600 Stack#1	DuraPES®600 Stack#2
Voxel size [nm]	25 ×25 ×50 (50 × 50 × 50)[4]	25 ×25 ×50 (50 × 50 × 50)[4]	160 × 160 × 100 (160 × 160 × 160)[4]	30 × 30 × 50 (50 × 50 × 50)[4]	25 × 25 × 50 (50 × 50 × 50)[4]	(12 × 12 × 50)	7.5 × 7.5 × 50
Image resolution	2048 × 1024 (1024 × 512)[4]	2048 × 1024 (1024 × 512)[4]	1024 × 1024 (961 × 284)[5]	1024 × 2048 (1229 × 615)[4]	1500 × 1024 (750 × 512)[4]	1024 × 1024 (490 × 824)[5]	1024 × 1024
Number of slices	200	200	395 (247)[4]	208	200	180	25
Stack dimensions [µm]	51.2 × 25.6 × 10	51.2 × 25.6 × 10	163.8 × 163.8 × 39.5 (153 × 45 × 39.5)[5]	60.5 × 30.25 × 10.4	37.5 × 25.6 × 10	(12.3 × 12.3 × 9) (5.9 × 9.9 × 9)[5]	(7.5 × 7.5 × 1.2)
Electron energy [keV]	4	4	5	4	4	4	4
Spot size	4	4	4	4	4	4	4
Pressure [Torr]	0.5	0.5	0.6	0.5	0.55	0.5	0.6
Image processing	Threshold level: 115	Threshold level: 132 (109), 118, 113	Background filtering Threshold level:112	Threshold level: 103	Threshold level: 120	Adaptive non-local offset filter Th-level:123	no image processing due to radiation damage
Integral dwell time [µs]	40 × 1 (40)	40 × 1 (40)	5 × 19 (95)	30 × 1 (30)	50 × 1 (50)	20 × 1 (20)	60 × 1 (60)
Acquisition time [h]	4.6	4.6	10.9	3.63	4.43	0.6	0.41
Knife speed [mm/s]	0.5	0.5	0.5	0.5	0.5	0.5	0.5
Original DM SBFSEM name	SBF242-240	SBF239-237	SBF130	SBF233/234	SBF230	SBF207	SBF206

[4] After resampling
[5] Cropped volume

4.3.2 Image filtering, segmentation and surface reconstruction

Once the images of a stack had been converted into JPEG format, the stack was loaded into the 3D visualization software AVIZO®Fire. Proper scaling of the resulting 3D reconstructions also required the input of the voxel size. Subdivision into sections (see Fig. 58 - Fig. 60), cropping of the volume, resampling and segmentation was also performed with AVIZO®Fire.

Resampling of the image resolution leads to cubic voxels and thus the same resolution in all three dimensions. The resulting voxel sizes after resampling are also listed in Table 10. As most of the images show a clear bimodal structure in the histogram, image segmentation was performed using global threshold level segmentation as described in section 3.4 using the AVIZO®Fire segmentation editor. In some cases, however, segmentation had to be preceded by filtering to reduce charging artifacts or noise (see Table 10). The description of the respective procedures was described in sections 3.4.1 and 3.4.2.

Segmentation yields a stack of binary images. This stack can be visualized in 3D as a so called LEGO model; the surface is not smooth but consists of discrete steps of the size of the voxels. This reconstructed model can be used as input for finite element simulations. Software packages like ANSYS or ABAQUS offer the possibility to calculate the thermal conductivity, influences of applied mechanical stress etc. In the present work the flux as well as the membrane resistance as a function of the distance from the surface were calculated using the AVIZO®Fire 7.0 extension XLab Hydro. The results will be discussed in section 4.4.4.

A smooth surface, however, can be created using the AVIZO®Fire surface generator tool. This tool triangulates the discrete steps and forms a realistic surface. A detailed description of the method can be found in [65]. The morphology of the DuraPES®450, the MicroPES®4F and the Sartorius 15406 membrane surfaces is well known from SEM images (see also section 3.1.1). In order to test the whole segmentation and reconstruction process, the reconstructed surface model was thus compared with such single SEM images. Fig. 61 shows single SEM images of both the air and roll sides of all three membranes and the corresponding 3D surface reconstructions. The morphology of the reconstructed surfaces and the SEM image sections show similar structures of the same scale, indicating that no significant distortion or other artifacts have been introduced by the cutting, imaging and reconstruction process. The reconstructed models give an impression of the morphology and the surface roughness of the membrane, and also provide a view into the interior structure of the membrane. A quantitative, statistical evaluation (e.g. of the pore size distribution) is not possible because of the small reconstructed section. This test verifies that the inner membrane structure will also be reconstructed properly, which is important for the exact calculation of the 3D parameters from the reconstructed models [3].

Fig. 62 shows the reconstruction of different layers of the DuraPES®450 membrane. The 3D reconstructions correspond to the red sections in Fig. 60. The complex, narrow pore structure of the separation layer (Fig. 62c), the wide pore structure of the intermediate layer (Fig. 62a and b) as well as the surface on the air side (Fig. 62d) are clearly visible. One data point of the parameters listed in Table 9 was calculated for each reconstructed section. The section width gives the spatial resolution of the respective parameter profile.

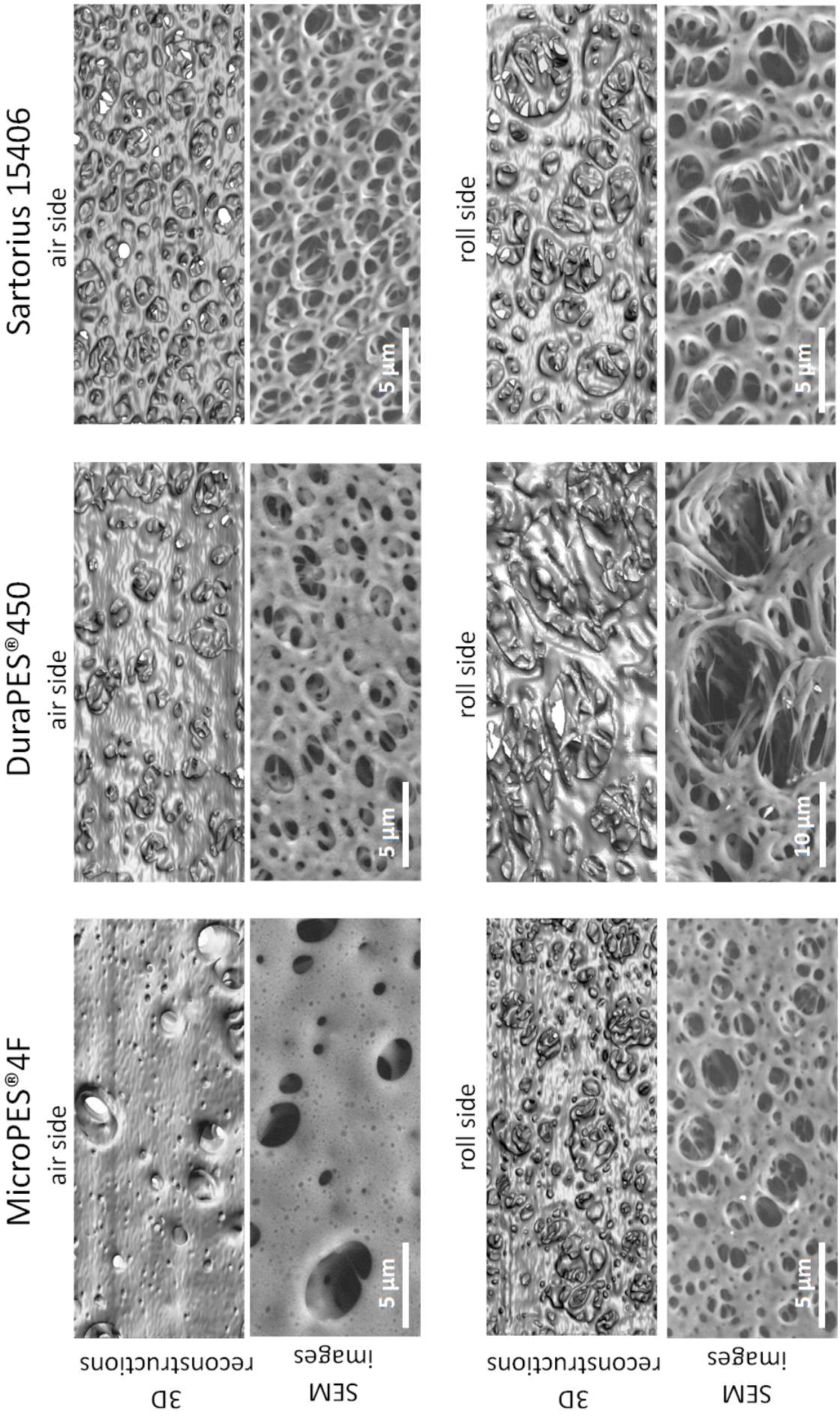

Fig. 61. Comparison of single SEM images (BSE) and the corresponding reconstructed surfaces. (SEM images: low vacuum mode; P = 0.5 Torr, electron energy = 5 keV)

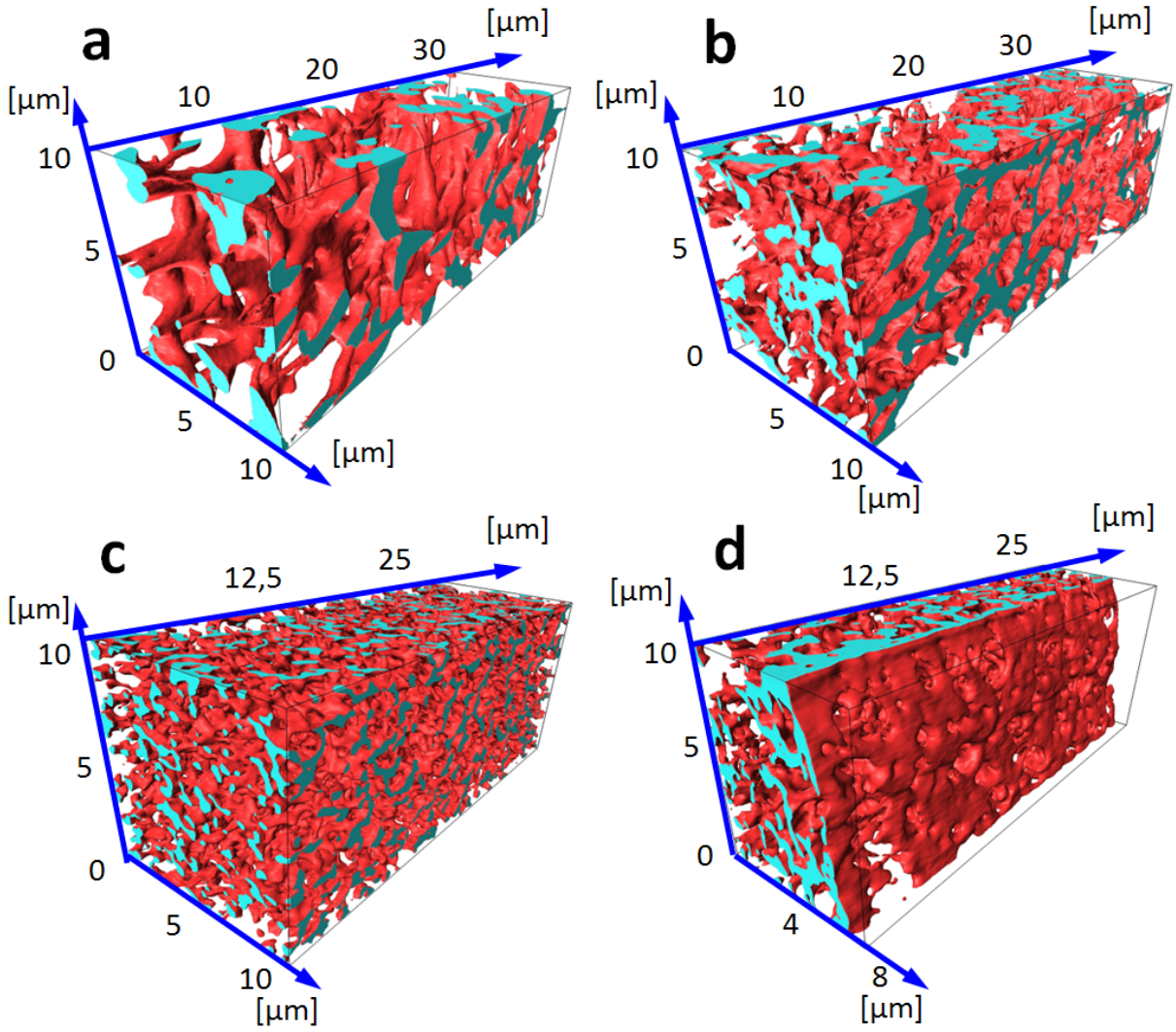

Fig. 62. 3D reconstructions of different layers of the DuraPES®450 membrane; a: support layer; b: intermediate layer; c: separation layer; d: air side of the membrane. The 3D reconstructions were based the red marked sections in Fig. 60. Each of these 3D reconstructions gives one data point for the respective parameter profiles (Fig. 64, Fig. 65, Fig. 67 and Fig. 70).

4.4 Parameter profiles obtained by 3D reconstruction

There are several reasons why 3D reconstructions are advantageous compared to single 2D images. They enable the calculation of parameter profiles which are more representative than those obtained in 2D, and some parameters like the inner surface, membrane resistance, tortuosity and many others can only be determined from 3D models. Some of these parameters can be verified experimentally, e.g. the volume porosity (see section 2.2.5), while other parameters, e.g. the connectivity of the pores (section 4.4.1 - below) are not directly accessible experimentally. But experiments nearly always deliver only a mean value, in contrast to the spatially resolved parameter profiles calculated from the 3D reconstructions.

4.4.1 Pore diameter and connectivity [3]

The pore network inside the membrane is quantified for the calculation of further parameters such as the connectivity and pore diameters. For this purpose a 3D chamfer distance transform of the 3D model was carried out [63]. In the binary images the pixel value of the membrane material is one and that of the free space in between zero. For each pixel with value zero the distance to the nearest pixel with value one is calculated. The greater the distance, the brighter the area (Fig. 63b). Subsequently, a skeleton filter is applied to the transformed structure. The skeleton filter removes pixel by pixel in the

bright areas until only the central pixel is left, but avoids a disruption of the structures [63]. The result is a network which corresponds to the pore network of the membrane (Fig. 63c). Moreover, the distance to the pore walls can be visualized by a so called tube network model, where the pore diameters are represented by the diameters of the tubes.

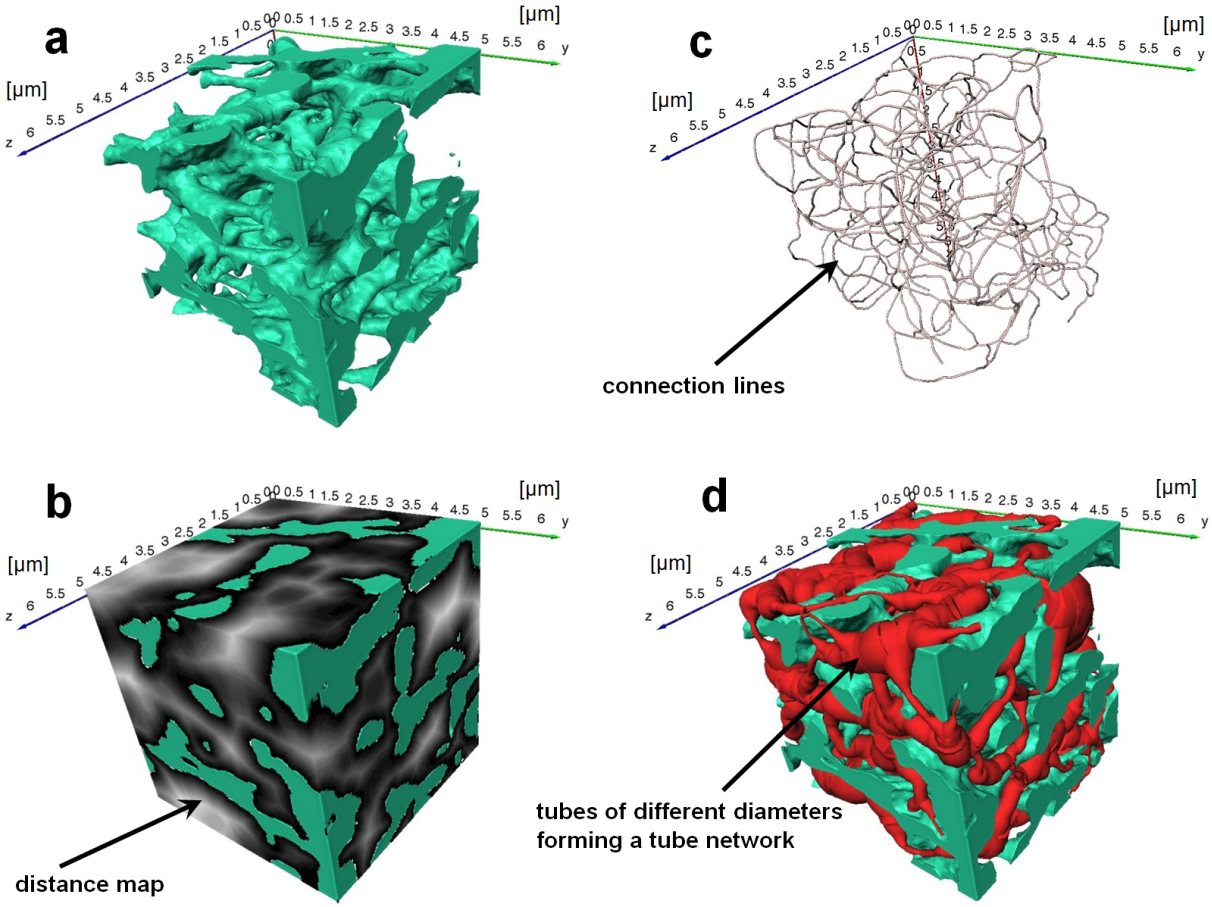

Fig. 63. Main steps of pore network calculation demonstrated on a part of the separation layer. a: reconstructed 3D model, b: distance map, c: pore network calculated from Fig. b, d: tube network model representing the pores; adapted from [3].

The AVIZO®Fire software provides all these procedures and the respective data can be saved in ASCII format for further calculations. Parameters such as the number of connections between the pores or the pore diameter distributions can be evaluated using MATLAB™. The membrane sectioning process was similar to that described in section 4.3.1. Therefore each data point of the diagram in Fig. 64 results from a 3D network model similar to that shown in Fig. 63c.

Because the pores on the roll side of the DuraPES®450 membrane are extremely large (see also Fig. 61), too few of them can be found in the respective image stack so that the values calculated for this region are not statistically significant. Therefore the calculation of the pore diameter and connectivity was performed only to a depth of 100 µm (see Fig. 64.) The number of the connection lines of the pore network model is a function of the pore density. The highest pore density is also an indicator of the position of the separation layer. Fig. 64d and h show the number of connections as a function of the distance from the surface A. The number of connections is normalized to a volume of 2000 µm³. The pore density in the separation layer of the DuraPES®450 membrane is much higher than that in the separation layer of the MicroPES®4F membrane. This is also in agreement with the higher inner specific surface area (see Fig. 65d and e).

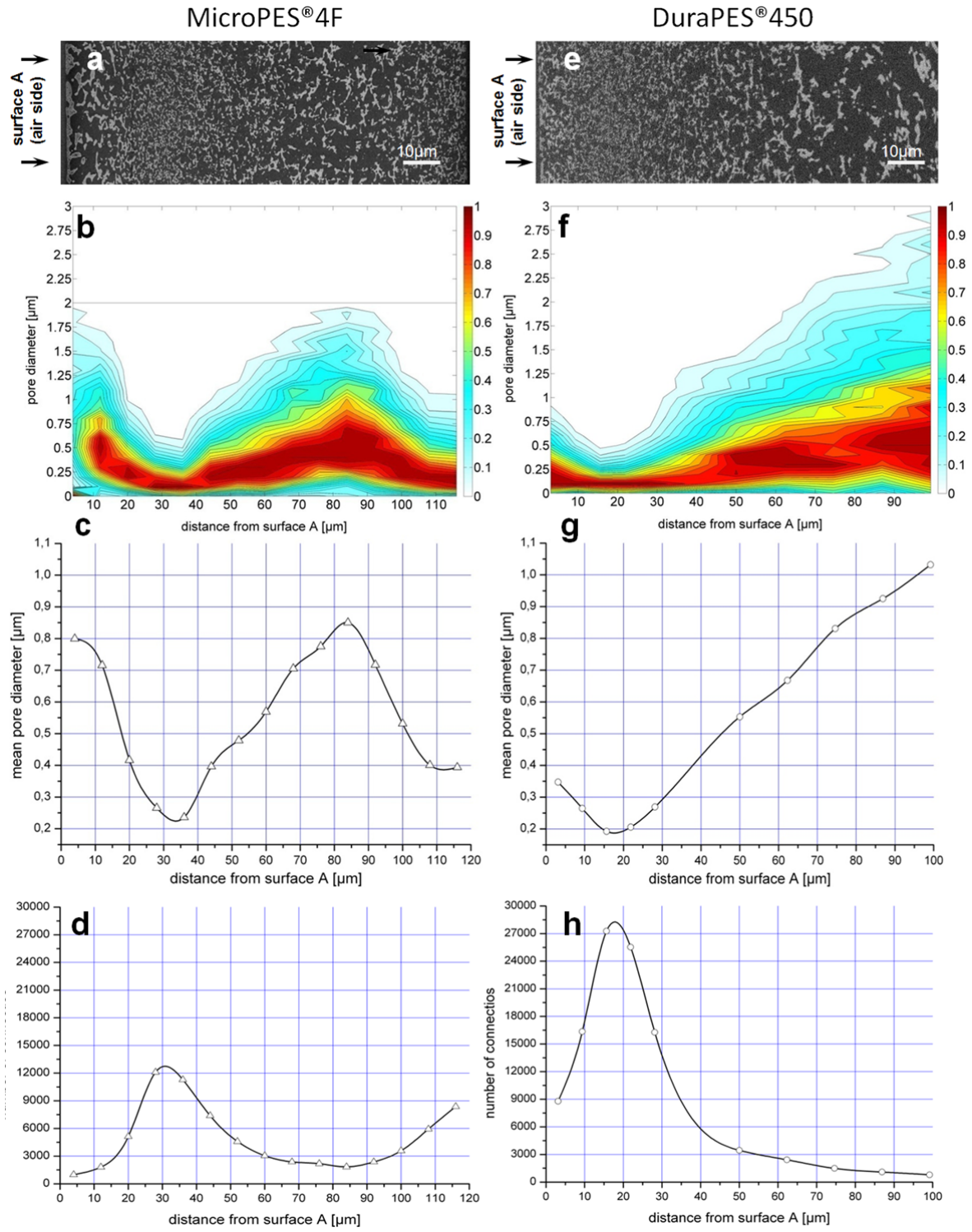

Fig. 64. a, e: SEM (BSE) images of cross-sections of the MicroPES®4F and DuraPES®450 membranes; b, c, f, g: mean pore size and pore size distribution as a function of the position at the cross-section for the respective membranes; the color bars to the right of Fig. b and f give the normalized probability of the occurrence of the pore diameters. d, h: number of connections between pores as a function of the position at the cross-section; adapted from [3].

The mean pore diameters were also obtained by calculating a tube network model. Each pore is represented by a tube as shown in Fig. 63d. The diameters of all tubes at a specific distance from the membrane surface, i.e. in one of the partitions, give the respective pore diameter distribution. The diagrams in Fig. 64b and c and Fig. 64f and g are a summary of all pore diameter distributions of the different partitions of the membrane cross-sections. The probability of finding a specific pore diameter

at a certain position (partition) inside the membrane (e.g. in the separation layer) is plotted in color. The positions of the separation layers show no pore diameters larger than approximately 0.60 µm. These results are consistent with those of the specific surface area plot (Fig. 65d and e) and with the plot of the number of connections (Fig. 64d and h).

The investigations have shown that the smaller the pore diameter, the higher the specific area and also the number of connections, and - as will be shown in section 4.4.4 - also the membrane resistance. As a consequence the profiles of the specific surface area, the number of connections and the membrane resistance have the same characteristics.

4.4.2 Specific surface area and volume porosity [3]

The specific surface area was determined for each section using equation (29) and plotted as a function of the distance from surface A (Fig. 65d-f). As expected, the maximum of the internal surface area was found in the separation layer of the membranes (marked 1). The minimum of the internal surface area for the MicroPES®4F membrane (marked 2) lies in the backup layer 40 µm from the roll side. The same would be expected for the DuraPES®450 membrane. No data points were calculated beyond a depth of 90 µm, however, due to the low statistical significance already mentioned above. Similar to the MicroPES®4F membrane, the Sartorius 15406 shows two minima in the specific surface area. Both are located approximately 30 µm beneath the surface (marked 2). In any case the relative difference between maximum and minimum is much higher for the inner surface area than for the volume porosity. The asymmetric pore structure of all three membranes can be clearly seen.

The volume porosity was also calculated for each section using equation (28) and plotted as a function of the distance to surface A (Fig. 65g-i). The values vary between 0.66 and 0.78 across the cross-section for all three membranes. This variation is much smaller than would be expected from a rough look at the images of the cross-section, but could be due to a corresponding variation in the wall thickness of the pores. Mean values are necessary to compare the results with experimental data achieved by porosimetry as described in 2.2.5. The calculated mean volume porosity (from the data points in Fig. 65g-i) for all three membranes is listed in Table 11 and compared to experimentally measured values in Fig. 69b. The values for the mean volume porosity obtained from the 3D models are generally in good agreement with the experimentally measurements. The main reason for potential mismatch lies in the segmentation (thresholding) procedure.

The minima of the volume porosity profiles of the MicroPES®4F and Sartorius 15406 membranes (marked with 1 in Fig. 65) indicate the position of the separation layer. No significant minima of the volume porosity were found for the DuraPES®450 membrane. The fraction of the pore area (equation 30) is a 2D approach for the volume porosity and was therefore additionally plotted in Fig. 65g-i (blue dashed lines). The same qualitative trend can be observed for all three membranes, and the differences in the qualitative values are smaller than 10%. This confirms the applicability of the principle of Delesse in these cases.

Additionally, two different threshold levels (109 and 132) were used for the segmentation of Stack#1 (first 50 µm of the profile) of the Sartorius 15406 membrane. The results in Fig. 65i demonstrate that this change in the threshold value causes greater differences in the calculated volume porosity than a change from 2D images to 3D models. But the maximum difference is still not much higher than 10%.

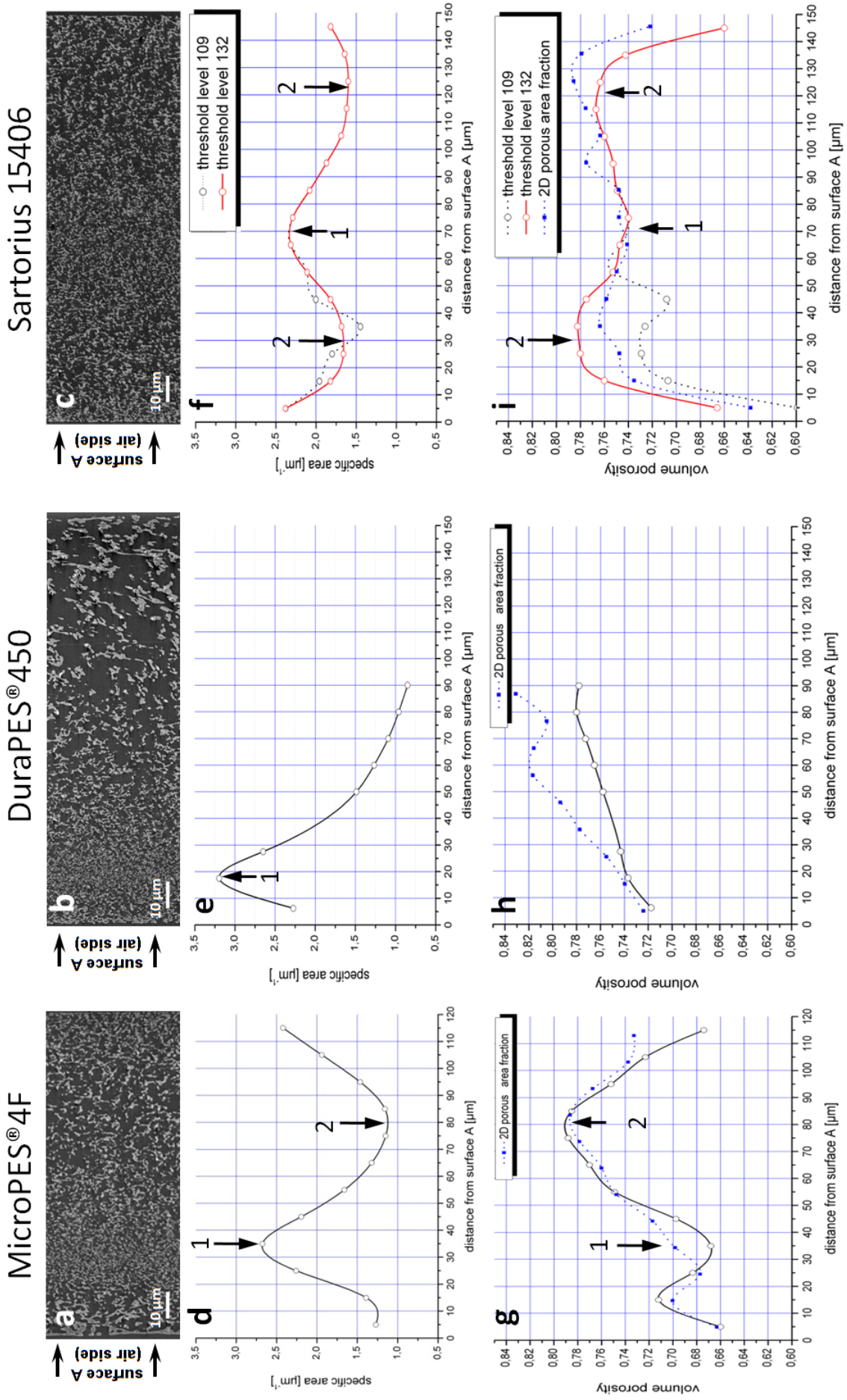

Fig. 65. a - c: SEM images (BSE) of the MicroPES®4F, DuraPES®450 and Sartorius 15406 membrane; d - f: specific surface area as a function of the distance from the air side for the respective membranes; g - i: volume porosity as a function of the distance from the air side for the respective membranes, with a comparison of the profiles of the fraction of the pore area obtained from 2D images.

4.4.3 Tortuosity

Tortuosity is defined as the ratio between membrane thickness and the average path length of a pore from one surface to the opposite surface [68]. AVIZO®Fire 7.0 provides a tool for the calculation of the path length through a porous structure, which was used to calculate tortuosity. The function of this tool is demonstrated by the example of a single sphere, which represents a simple porous medium.

Fig. 66a shows the sphere (radius 200), the longest (L_1 - red) as well the shortest (L_z - blue) path along the z direction. The colored map (xy plane) in Fig. 66b represents the length of all paths in z direction, with the longest path located at position A (centre of the sphere - yellow); the shortest paths are obviously found outside the sphere (white). The tortuosity is the mean value of all these paths divided by the length in z direction:

$$tor = \frac{\overline{L_1}}{L_z} \geq 1 \,. \qquad \textbf{(31)}$$

The same approach was used to calculate the local tortuosity of the membrane structure. Fig. 66c shows a map representing the path lengths in z direction trough a 10 µm thick membrane section. White areas represent direct paths (around 10 µm) and colored areas tortuous “winding” pores.

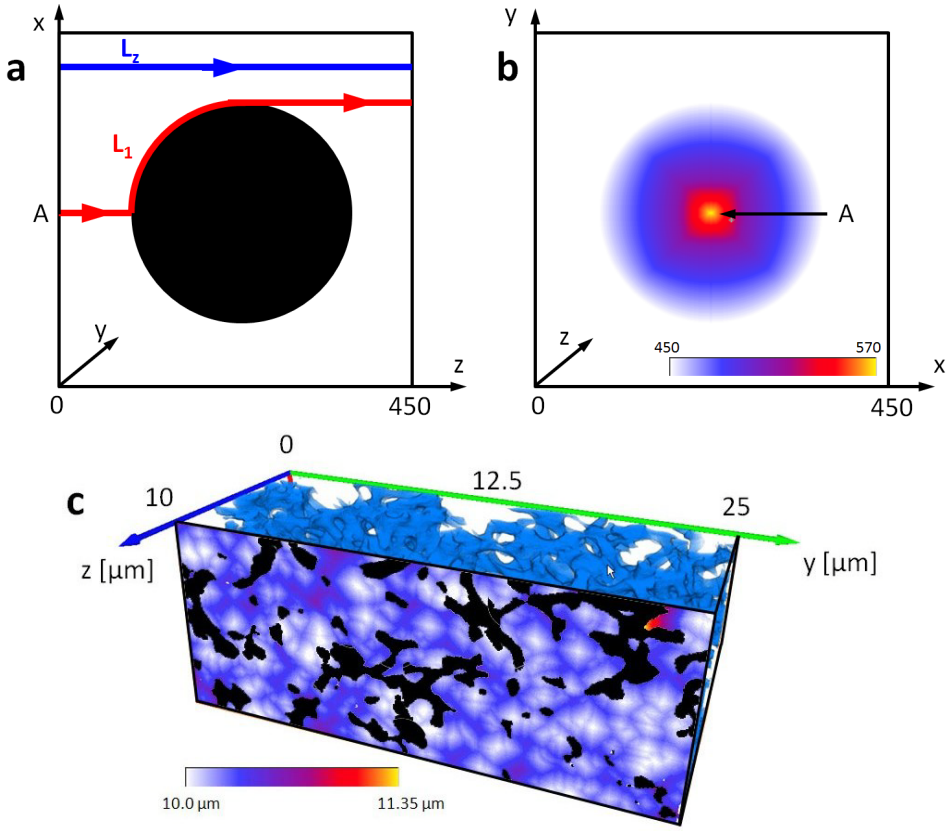

Fig. 66: Tortuosity calculation. a: longest path around a sphere (L_1 - red) and shortest path (L_z - blue); b: colored map representing the path lengths in z direction around a sphere; c: colored map representing the path lengths in z direction within the membrane structure.

Because the voxel size in 3D reconstructions of the membranes is 50 nm, this kind of tortuosity calculation is valid for particles size of 50 nm. Fig. 67 shows the results of the calculations. The highest tortuosity for all membranes was found at the membrane surface. MicroPES®4F and Sartorius 15406 also showed pronounced local maxima at the positions of the respective separation layers (marked with a 1 in Fig. 67d and f). A clear tortuosity minimum was found in the backup layer of the

MicroPES®4F (marked with a 2) around 40 µm from the roll side. The DuraPES®450 membrane shows no clear tortuosity maximum at the separation layer.

The tortuosity maximum on the membrane surfaces may be an artifact. It may be caused by the already mentioned fact that the structure on the direct membrane surface is very different from that of the interior, which could contribute to these ambiguous results.

But it still must be proven whether the mathematical routines used for these calculations still give reliable results for such extremely complex systems as these membranes.

These calculations thus represent only the starting point for a more in-depth investigation of tortuosity.

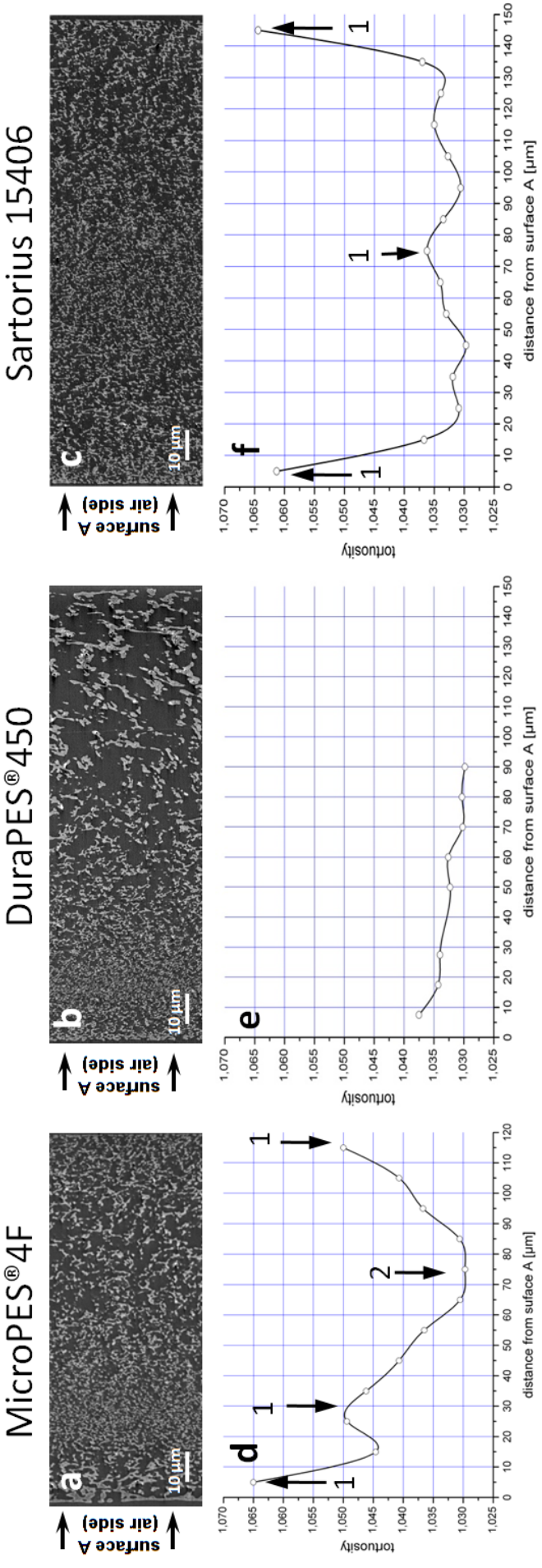

Fig. 67. Profiles of the MicroPES®4F, DuraPES®450 and Sartorius 15406 membrane. The local tortuosity is plotted as a function of the distance from the air side. The SEM images (BSE) at the top show cross-sections of the respective membranes.

4.4.4 Fluid simulations and membrane resistance profiles [69]

All parameters studied so far characterize the asymmetric membrane structure, but none of these (except the volume porosity) can be measured directly. Membrane manufacturers, however, are very interested in the maximum possible flux, the so called pure water or trans-membrane flow (TMF), and possibilities for its optimization. It is obvious that a local high specific surface area leads to strong friction between the fluid and the membrane matrix, and as a consequence limits the maximum flux. Of course, the larger the pores the higher the flux, as shown by the Hagen-Poiseuille law assuming cylindrical pores:

$$Q = \frac{dV}{dt} = \frac{r^4 \pi}{8 \eta l} \, (P_A - P_B) \, , \qquad \textbf{(32)}$$

with Q the volume flow, V the volume, P_A, P_B the pressures at the membrane surfaces, r the pore radius, η the fluid viscosity and l the cross-section length.

The law of Darcy (33) [70] determines the maximum flux at a certain pressure gradient, assuming a non-compressible and laminar fluid:

$$q = -\frac{k}{\eta} \boldsymbol{\nabla} \cdot \boldsymbol{P} \, . \qquad \textbf{(33)}$$

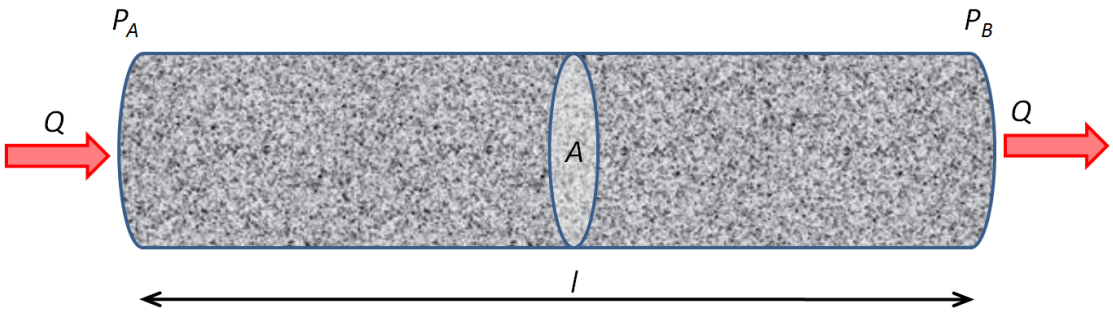

Fig. 68. Sketch of a porous material, with l its length and A its cross-section.

One-directional flow, as shown in Fig. 68, is determined by the pressure difference ($P_A - P_B$), the length l, the cross-section area A, the fluid viscosity η and the absolute permeability k:

$$Q = -\frac{k}{\eta} \, A \, \frac{(P_A - P_B)}{l} \, , \qquad \textbf{(34)}$$

with $= \frac{Q}{A}$, the flux ,

$$q = -\frac{k}{\eta} \, \frac{(P_A - P_B)}{l} \, . \qquad \textbf{(35)}$$

The membrane resistance is defined as [71]:

$$R_m = \frac{l}{k} \, , \qquad \textbf{(36)}$$

and thus equation (34) can be written as:

$$q = \frac{1}{\eta} \frac{(P_A - P_B)}{R_m} \ . \qquad (37)$$

This equation is similar to Ohm's law $\left(I = \frac{U}{R}\right)$. However, the absolute permeability, which mainly determines the membrane resistance, is unknown. Yet this material specific parameter can be determined if the structure of the porous material is known. But the determination cannot be done directly! First the velocity field of the fluid must be calculated under defined boundary conditions. Once the complete velocity field is known the absolute permeability can be calculated by averaging over the velocity field. New finite element software like the AVIZO®Fire XLab Hydro package is able to solve the Navier-Stokes equations numerically. Neglecting the convection terms, assuming a steady state laminar flow [72] and an incompressible Newtonian fluid, the Navier- Stokes equations have the form:

$$\boldsymbol{\nabla} \cdot \boldsymbol{v} = 0 \qquad (38)$$

$$\eta \nabla^2 \boldsymbol{v} - \boldsymbol{\nabla P} = 0 \ . \qquad (39)$$

To solve the equations, periodic boundary conditions have to be applied. A common boundary condition for this problem is the so called non-slip condition at the fluid-solid interface. At the interface boundary (in the present case at the pore walls) the fluid velocity is zero:

$$\boldsymbol{v} = \mathbf{0} \ . \qquad (40)$$

The image stack - consisting of binary images - determines the boundary conditions for the equations and so the membrane structure determines the resulting velocity field. In any case the image stack used must be representative of the whole membrane structure.

The solution of these equations gives the complete velocity field of the porous structure. As the present membrane structure is very complex, the calculated velocity field is extensive as well. In most cases, only the resulting membrane flux is of interest. The solution of the Navier-Stokes equation, however, does not give a (single) parameter describing the membrane flux. A volume averaged form of the Navier-Stokes equations is thus used to spatially smooth the equations by averaging them on a defined volume. After transformation the above equations are valid both for the fluid phase (within the pores) and the solid phase. The complete procedure is described in [73]. As a consequence of the transformation the Navier-Stokes equations are modified in a way that derivatives of the velocities and pressures are used, instead of the velocities and pressures themselves:

$$\boldsymbol{\nabla} \cdot \overrightarrow{\boldsymbol{D}} = \mathbf{0} \qquad (41)$$

$$\eta \nabla^2 \overrightarrow{\boldsymbol{D}} - \boldsymbol{\nabla d} = \overrightarrow{\mathbf{1}} \ , \qquad (42)$$

with $\overrightarrow{\boldsymbol{D}}$ the tensor representing the spatial deviation of $\boldsymbol{v}$ and $\boldsymbol{d}$ the spatial deviation of $\boldsymbol{P}$ and $\overrightarrow{\mathbf{1}}$ the unit tensor. Solution of the above equations and calculation of a mean value of $\overrightarrow{\boldsymbol{D}}$:

$$\overrightarrow{\boldsymbol{k}} = \frac{1}{V} \int_V \overrightarrow{\boldsymbol{D}} \, dV \ , \qquad (43)$$

finally gives the permeability tensor $\overrightarrow{\boldsymbol{k}}$.

The $\overrightarrow{\boldsymbol{k}}$ tensor was calculated for all sections (see Fig. 58 - Fig. 60) along the cross-section of the MicroPES®4F, DuraPES®450 and Sartorius 15406 membranes using the AVIZO®Fire XLab Hydro

package. The calculations were performed on a Dell® workstation equipped with two 6 core Xeon processors running at 3 GHz and 48 GBytes of RAM. The calculation time for one 10 µm width section was between 0.5 and 5 hours, depending on its structure. All resulting permeability tensor values are listed in Table 12. The color of the background belongs to the respective stacks as shown in Fig. 58 - Fig. 60. As transverse flow is neglected, only the k_{xx} elements of the absolute permeability tensor are of interest and were used for calculation of the local membrane resistance R_{xx} using (36). The other tensor elements (k_{xy} and k_{xz}) are at least one order of magnitude smaller. The membrane resistance profiles as a function of the position at the cross-section are additionally plotted in Fig. 70. They clearly show a maximum at the separation layer of each membrane (marked with 1). As expected, the resistance minimum is found at the support structures. The profiles have the same qualitative characteristics as the profiles of the specific surface area in Fig. 65d-f. This is due to the friction at the pore walls. The overall membrane resistance (R_m) can be calculated by summing up the local membrane resistance values along the cross-section:

$$R_m = \sum_i R_{xx_i} = \sum_i \frac{l_i}{k_{xx_i}}, \qquad \textbf{(44)}$$

with l_i the local section width, R_{xx} the local membrane resistance and k_{xx} the local permeability.

The DuraPES®450 membrane required interpolation as well as extrapolation of the data points to achieve a profile curve along the complete cross-section (Fig. 70e). The real resistance profile can be different, especially in the extrapolated range (90 to 150 µm). This can be the reason for the mismatch with the experimental data.

Table 11 shows the calculated values for the membrane resistance R_m and the resulting TMFs calculated with (37). The value of the viscosity of water at 20°C is 0.001 pas·s.

Table 11: Comparison of membrane resistance, TMF and volume porosity values provided by the manufacturer, measurements[6] and simulations.

	Overall membrane resistance R_m [µm^{-1}]	TMF [ml/(min cm² bar)]	TMF [µm/s]	Volume porosity [%]
MicroPES®4F				
Manufacturer data [49]		> 60	> 10000	
Measured[6]		80.5	13420	76.7
Results fluid simulations / 3D reconstructions	6430	93.0	15550	72.3
DuraPES®450				
Manufacturer data [49]		> 75	> 12500	
Measured[6]		86.1	14350	78.3
Results fluid simulations / 3D reconstructions	4880	123.0	20490	75.6
Sartorius 15406				
Manufacturer data [50]		46	>7670	
Measured[6]		53.3	8880	77.0
Results fluid simulations / 3D reconstructions	7820	77.0	12790	74.6

The simulated (red), measured[6] (blue) and manufacturer's (black) trans-membrane flow (TMF) values are shown in Fig. 69a. In all cases the simulated values are higher than the measured values. The values provided by the manufacturer are minimum values; in all cases the measured values were higher.

The best agreement between simulation and experiment was observed for the MicroPES®4F membrane. The reason for the largest mismatch (DuraPES®450) may be due to the extrapolation which was performed assuming a nearly constant membrane resistance value on the roll side (90 - 150 µm), which is definitely not correct. For a better result, a larger volume on the roll side has to be reconstructed to get a statistically significant number of pores. Last but not least, errors in the segmentation procedure can have a substantial influence on the calculated values of the membrane resistance.

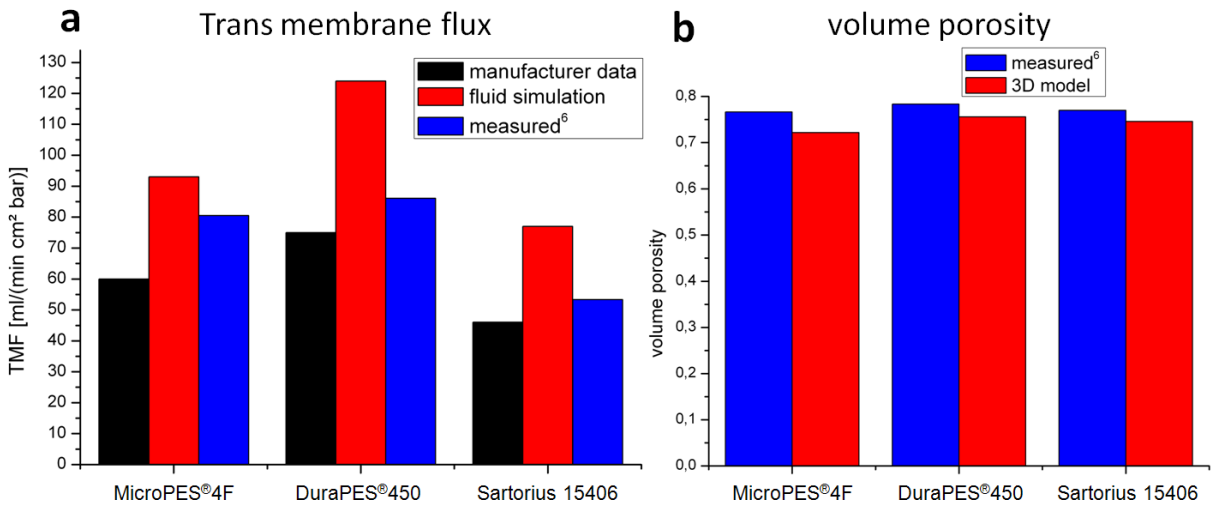

Fig. 69. Trans-membrane flow (TMF) and volume porosity of the membranes. (black: manufacturer data, red: results from the fluid simulation / 3D model, blue: measured[6] values).

[6] The measured values were determined by the manufacturer at parts of the same membrane sheet used for these investigations using experimental setups similar to that described in sections 2.2.5 and 2.2.7.

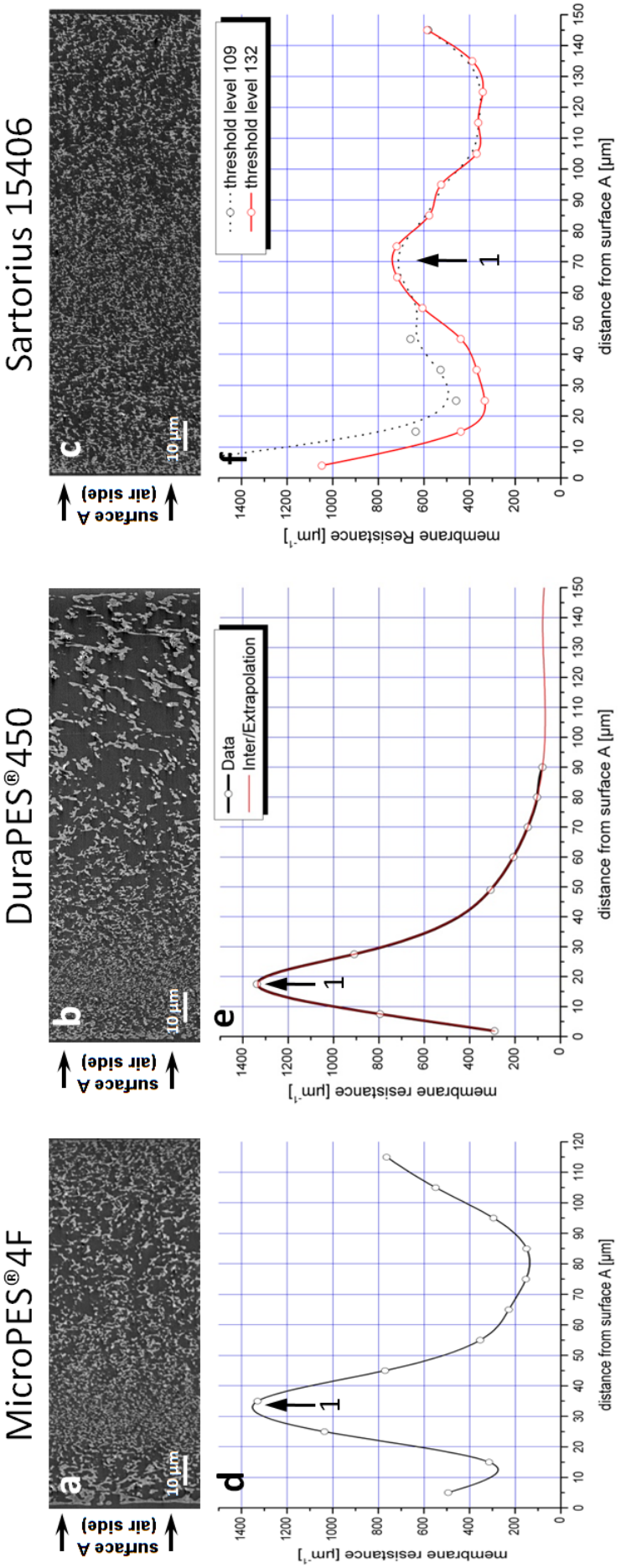

Fig. 70. The resistance R_{xx} of the MicroPES®4F, DuraPES®450 and Sartorius 15406 membranes as a function of the distance from the air side. The SEM images (BSE) at the top show cross-sections of the respective membranes.

Table 12: Permeability tensor values and membrane resistances calculated with equation (36)

Position [µm]	k_{xx} [µm²]	k_{xy} [µm²]	k_{xz} [µm²]	R_{xx} [µm^{-1}]	k_{xx} [µm²]	k_{xy} [µm²]	k_{xz} [µm²]	R_{xx} [µm^{-1}]	Position [µm]	k_{xx} [µm²]	k_{xy} [µm²]	k_{xz} [µm²]	R_{xx} [µm^{-1}]
	MicroPES®4F				Sartorius 15406					DuraPES®450			
5	0.0181	0.0015	-0.0014	493	0.0074	-0.0001	0.0002	1048	1.8	0.0124	0.0005	0.0042	290
15	0.0318	0.0006	0.0007	314	0.0227	0.0012	0.0005	438	7.5	0.0126	-0.0001	0.0006	795
25	0.0096	$<10^{-4}$	0.0003	1036	0.0304	-0.0001	0.0013	333	17.5	0.0075	$<10^{-4}$	0.0002	1338
35	0.0075	0.0002	0.0002	1329	0.0272	-0.0001	$<10^{-4}$	369	27.5	0.0110	-0.0004	0.0006	909
45	0.0129	0.0004	0.0005	770	0.0228	-0.0003	0.001	439	49	0.0369	0.0001	0.0009	308
55	0.0283	0.0002	0.0006	353	0.0165	0.0009	0.0004	607	60	0.0483	$<10^{-4}$	0.0041	207
65	0.0439	-0.0013	0.0015	228	0.0139	0.0008	0.0004	717	70	0.0696	0.0019	-0.0006	144
75	0.0656	-0.0019	-0.0010	152	0.0139	0.0007	0.0005	719	80	0.0977	0.0061	0.0065	102
85	0.0664	-0.0064	0.0020	150	0.0173	0.0002	0.0003	577	90	0.1274	0.0069	0.0081	78
95	0.0338	0.0005	-0.0017	295	0.0212	0.0005	0.0012	525					
105	0.0182	-0.0014	-0.0008	548	0.0270	0.0008	0.0025	370					
115	0.0103	-0.0004	-0.017	764	0.0276	0.0013	0.0028	362					
125					0.0292	0.0005	0.0015	342					
135					0.0258	0.0014	0.0011	388					
145					0.0129	0.0001	0.0010	586					

Stack#3
Stack#2
Stack#1

4.5 Porous structure of the membrane matrix

The smallest pores of the DuraPES® and MicroPES® membranes are found in the separation layer. However, detailed cross-section images of the membrane surface and beneath revealed an even finer nano-sized sub-porous structure within the membrane matrix.

The sub-porous structure (pore size around 100 nm, marked B) can be clearly seen in Fig. 71a. It appears both on and beneath the membrane surface, in places where the pore walls exceed a certain thickness. This is the case on the air side of the MicroPES® membranes, and on the roll side of the DuraPES® type.

Dark areas in Fig. 71a, marked with red arrows, indicate regions where the resin has not filled all these nano-sized pores. Most of the pores within the sub-porous structure are filled, however, which points out that these pores within the membrane matrix should be connected to the main pores of the membrane. This was verified by a 3D reconstruction of the air side of the DuraPES®600 (old version) membrane at high magnification.

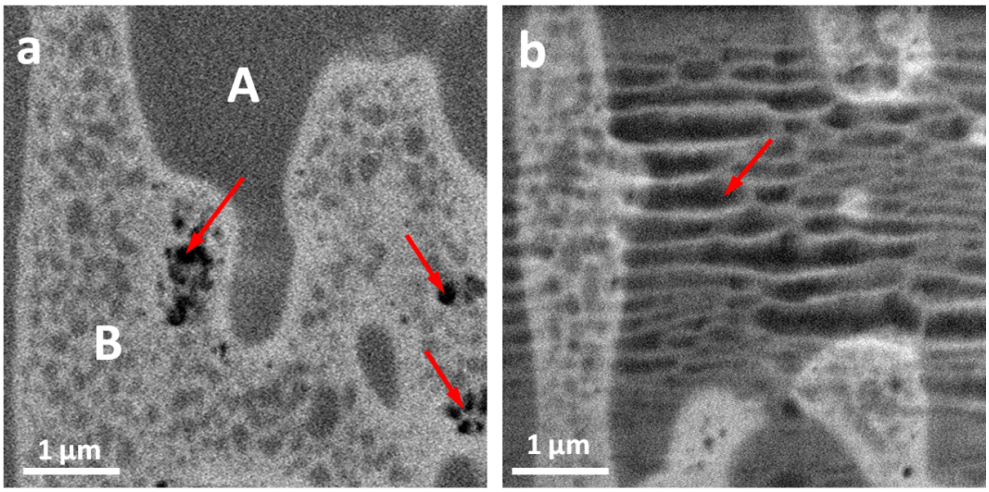

Fig. 71. a: Sub-porous structure in the DuraPES®600 membrane (Stack#1) with (A) membrane pore and (B) membrane matrix with the sub-porous structures; b: irradiation damage caused by SEM imaging, using image acquisition parameters as listed in Table 10 (Stack #2).

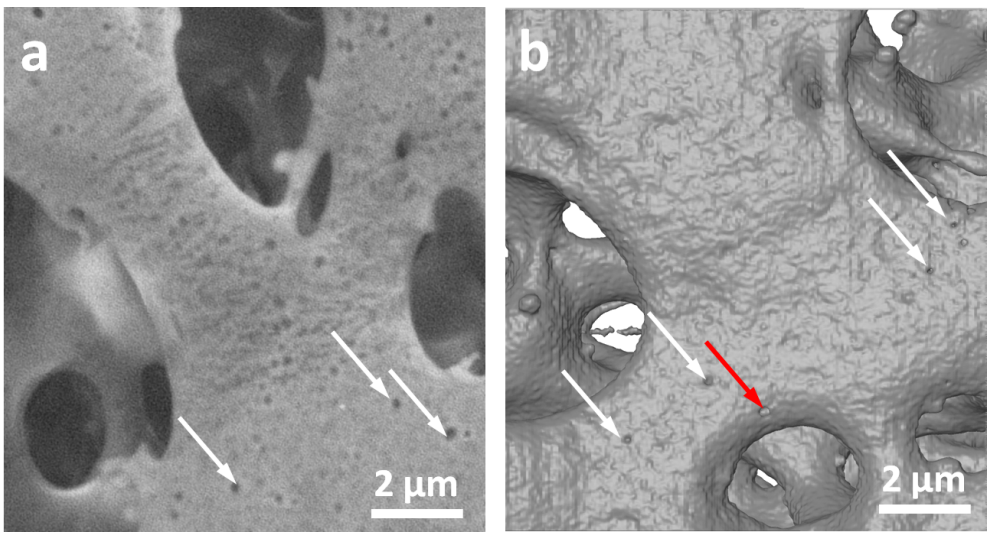

Fig. 72. Comparison of a single SEM image (a) and the corresponding reconstructed surface of the DuraPES®600 membrane (b). Small pores are marked with arrows, the red arrow marks a connection to the nanoporous structure as shown in Fig. 73.

(SEM image: BSE, low vacuum mode, P = 0.5 Torr, electron energy = 5 keV)

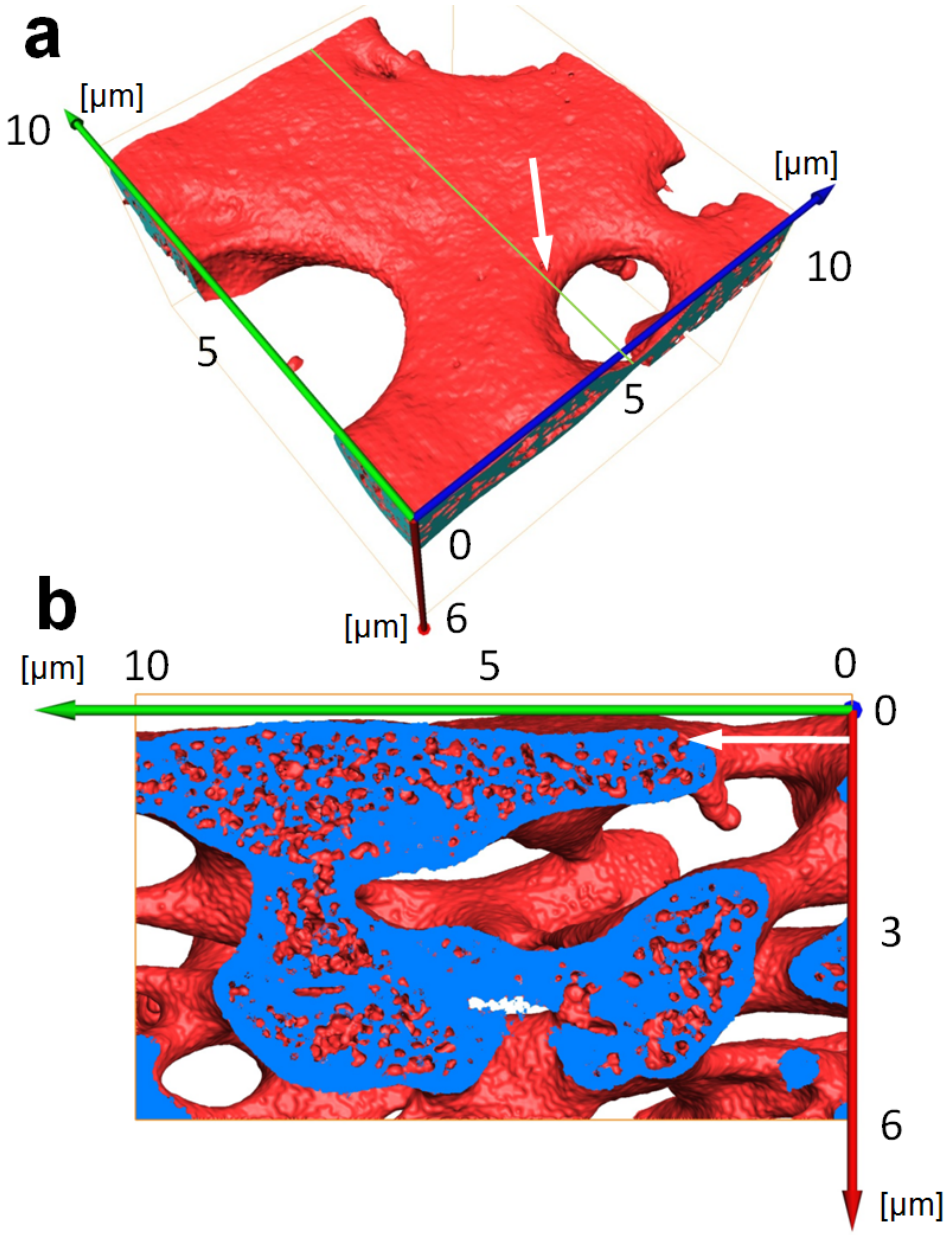

Fig. 73. a: 3D reconstruction of the surface of the Dura®PES600 membrane showing small pores (white arrow); b: ortho-slice view of the reconstruction at the position of the green line in a, a connection of the regular large pores and sub-porous structure of the membrane matrix (white arrow) is visible.

Fig. 73a shows the surface morphology within the surface pores of the Dura®PES600 membrane. In some positions small pores are visible (white arrow) indicating a possible connection to the inner sub-porous structure. One connection was verified using an ortho-slice view (Fig. 73b). The white arrow marks the connection between the two pore networks. A comparison of the reconstructed membrane surface with a single SEM image of a similar area seems to confirm that all marked pores are possible connections to the porous structure within the membrane matrix (Fig. 72). The pore size of this structure is, however, at the resolution limit of the microscope. Using higher magnifications and longer acquisition times causes strong irradiation damage as shown in Fig. 71b. The acquisition parameters for both images in Fig. 71 are listed in Table 10. Further detailed studies of the nano-scale sub-porous structure could be performed by transmission electron microscopy tomography (TEMT) [74,75]. Due to the limited resolution of the SBFSEM, the sub-porous structure was neglected in the data analysis described in section 4.4 as this nanoporous network should not really affect the filtering behavior of the membranes.

4.6 Further improvements and outlook

Although the results of 3D reconstruction are generally in good agreement with measured values, further research and improvements are necessary in terms of image acquisition and sample preparation. The samples used in the present work deliver sufficient contrast between resin and matrix material due to the sulfur content of the membrane matrix. Generally the image acquisition time should be kept as low as possible. Staining of the membrane material, if possible, can help to increase contrast and reduce image acquisition times. Staining the resin instead of the sample (negative staining) can also be a proper solution when staining of the membrane makes it too brittle for cutting. In some cases the membrane surface was not exactly aligned perpendicular to the cutting plane. This was due to bending of the membrane sheet during embedding (Fig. 74a). Features at the cross-section (separation layer, membrane surface) can thus show a shift during ultramicrotome slicing and imaging and lead to distortions in the parameter profiles. To avoid bending, the membrane has to be fixed not only at the bottom of the basin, but also to an additional support aligned perpendicular to the cutting plane (Fig. 74b).

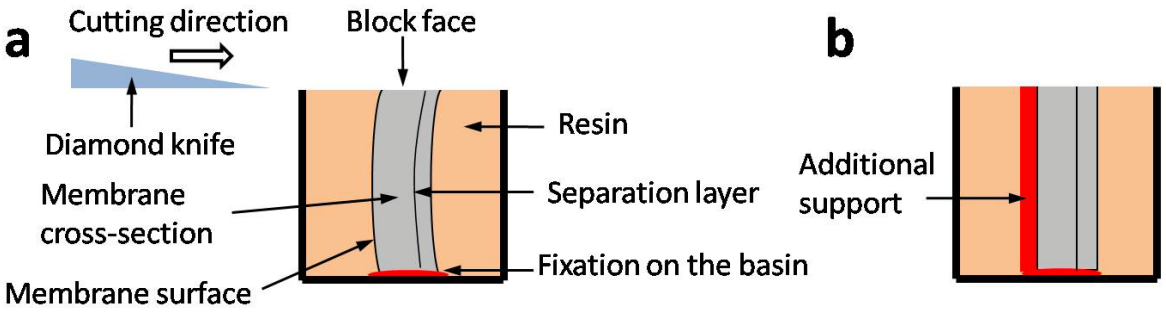

Fig. 74. Sketch of the embedded membrane. a: bending of the membrane occurs during embedding; b: an additional support can guarantee a perpendicular alignment of membrane surface and cutting plane.

4.7 Conclusions

Membrane manufacturers continuously vary the process parameters in the development of new membranes to obtain a membrane pore structure with the desired properties, e.g. higher flux or lower fouling tendency. The properties of the newly designed membranes can be measured with various methods as described in section 2.2. On the other hand, computer software packages like GEODICT (GEOmetric - preDICTion) offer the possibility to simulate a 3D model of a porous structure from a single 2D image and subsequently calculate the properties of the modeled structure (e.g. the flux). These data are then used as input parameters to modify the simulated model so as to get information about how to modify the membrane structure to optimize specific properties. This is a very time efficient approach, but the simulated model can vary significantly from real ones.

More realistic 3D models of a porous material (in this work: microfiltration membranes) can be reconstructed by automated ultramicrotomy in a low vacuum scanning electron microscope. The material properties can be reliably calculated from these reconstructions and compared with the measured properties of the real material (see section 4.4.4). The results can thus provide a sound input for the adaptation of the fabrication process, as was shown by Wiegmann [76] at the WFC11 in Graz.

New 3D microscopic techniques like 3View™ will play a major role in the field of computer aided membrane engineering (Fig. 75) and in the long run will additionally used parallel to conventional 3D reconstruction methods like X-ray computer tomography (XCT), which is currently limited to a resolution of around 0.5 µm.

The main aspects and challenges of 3D reconstruction by automated ultramicrotomy can be summarized as follows:

1. Sample requirements

   The sample must be able to be cut with a diamond knife and should provide sufficient contrast for SEM imaging. If this is not the case, staining of either the membrane material or the resin will be necessary. The instrument used for this work did not provide specimen cooling (*in situ* cryo-ultramicrotomy). However, the method as it is explained in this work, can be applied for materials like paper, biological samples, polymer blends [77], wood etc. Moreover ductile metals (aluminum) can also be investigated by using the 3View™ tool [78].

2. Slice and view

   Slice and view can already be operated in a fully automatic mode and does not represent a critical part of the process, at least for well sliceable samples. Nevertheless, tools like 3View™ are not routine methods, and so monitoring of the data acquisition process is still essential. Errors from debris or thermal fluctuation causing drift problems can occur any time. Transmission electron microscopy tomography (TEMT) is a complementary method which can be additionally used to get information at the nanoscale and thus obtain a complete overview of the sample structure at all orders of magnitude. Hard materials require sectioning and imaging by focused ion beam instruments (FIB).

3. Image filtering

   The main tasks of image filtering are the reduction of noise and the removal of background inhomogeneities.

4. Segmentation

   Segmentation is one of the most critical parts of the complete process. A lot of segmentation routines are available [63-65]. In some cases, however, manual segmentation may be necessary, especially in the case of biological samples.

5. 3D reconstruction

   3D reconstruction and surface generation is generally trouble-free as long as the computer is equipped with a proper graphic card and sufficient memory. Slice alignment routines which are implemented in most software packages worked very well. Generally the images of the stack are already aligned and require slight corrections only in case of drift during the slicing and imaging process.

6. Data extraction

   Software packages like AVIZO®Fire 7.0 allow the calculation of many morphological parameters, e.g. surface area, volume porosity and connectivity. In any case the data extracted from the 3D reconstruction provide more reliable (quantitative) information about the sample structure than provided by one single 2D image.

7. Finite element methods

   The application of finite element methods (FEM) to realistic, representative 3D models completes the investigations. In this work fluid mechanical properties like membrane flux and membrane resistance are calculated and compared with measured data. Finite element methods are not limited to fluid mechanical simulations but can also be used for the calculation of e.g. mechanical properties (stress, etc.), demonstrating the high potential of microscopic 3D methods.

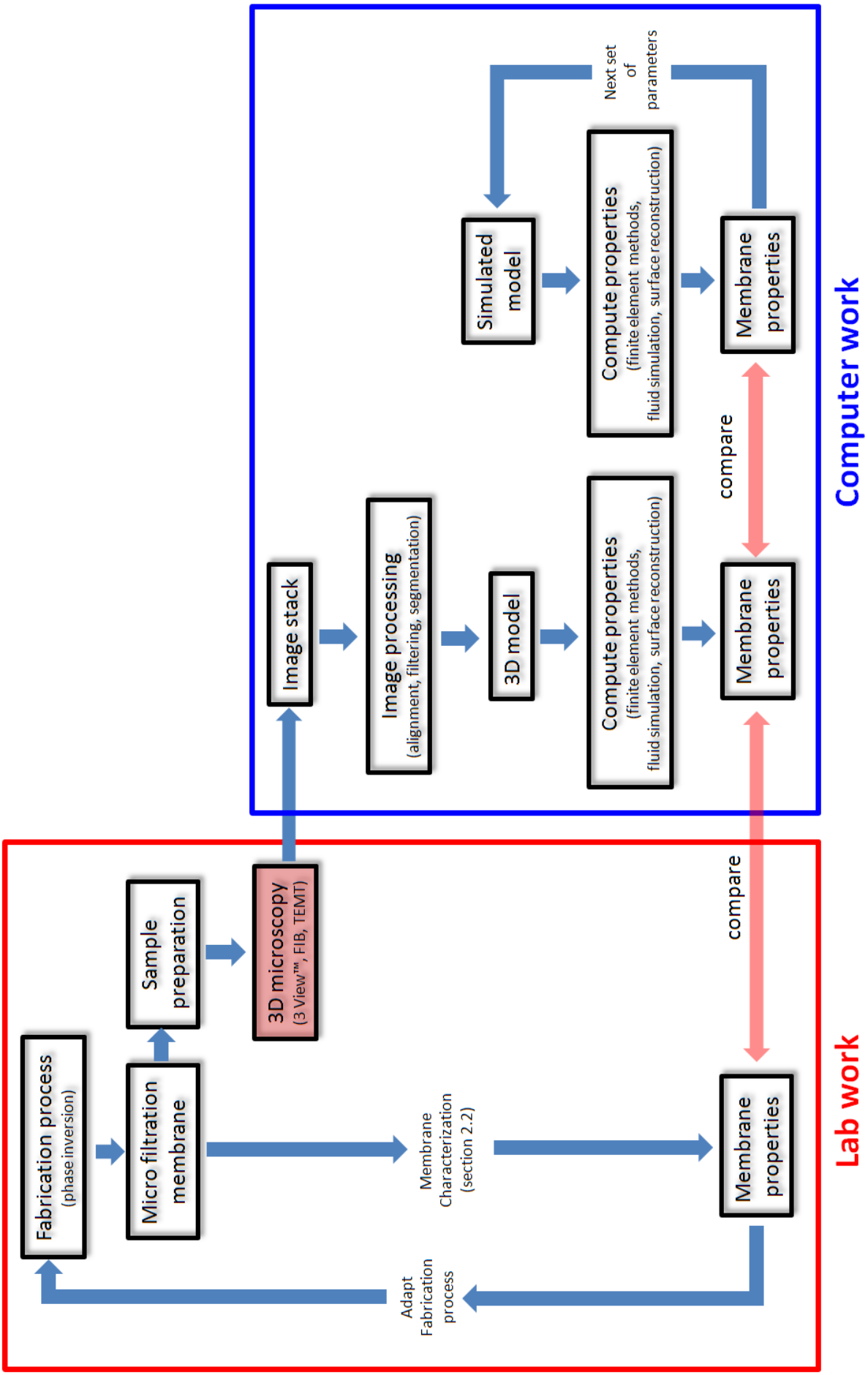

Fig. 75. Flow chart of computer aided membrane engineering; adapted from [76].

5 Experiments under wet conditions

As mentioned in section 3.3.3 the wetting experiment is divided in two parts: the wetting of the membrane via the cooling clamps and the drying of the membrane initialized by pressure reduction. A qualitative description of these two (in reality very complex) processes and some theoretical aspects will be given in the next section.

5.1 Basic theoretical aspects

5.1.1 The wetting process

If the pressure in the specimen chamber of the microscope is raised above the dew point, water condenses at the cooling camps and gets in contact with the membrane sample (see Fig. 39 for the experimental setup). The condensation rate and, in consequence, the amount of water present at the cooling clamps after a certain time depend on both the temperature and the pressure in the specimen chamber. The exact interaction between the water from the cooling clamps and the membrane, however, cannot be investigated. In any case water enters the membrane mainly through its cross-sections. The membrane will finally be completely wetted by a horizontal flow of water parallel to the membrane surface, with the capillary forces acting as the main driving force. A very similar, but simpler situation is the dynamics of the flow within a horizontal capillary which was first studied theoretically and experimentally by Washburn [79]. The movement of the liquid front within a capillary driven by the capillary pressure can be described by:

$$L^2 = \frac{\gamma d t}{4\eta}, \qquad \textbf{(45)}$$

with L, the length of the liquid column at the time t within a capillary of a diameter d. Fisher verified the equation experimentally for pore radii between 3 and 400 µm [80]. A more sophisticated theoretical model including dynamic contact angles was developed by Hamraoui [81]. Later Fisher proved that the Washburn equation can also be used for complex porous materials like biscuits [82], suggesting their suitability for complex microfiltration membranes. The experimental verification for membranes, however, requires a better time resolved experiment.

5.1.2 The drying process [19]

In the case of porous materials capillary forces keep the water in the material. They must be overcome during the drying process, which requires energy input. This can be thermal energy (heat) or induced by a reduction of the environmental pressure (vacuum drying). Once the water has vaporized the water vapor must be transported from the place where it was formed (e.g. from the surface) to the environment. Therefore knowledge of vapor diffusion and also heat transfer is essential. On the other hand, the movement of the liquid front within the sample pores determines the place where the liquid vaporizes. The heat transfer, vapor diffusion and liquid transport inside the material are coupled for a general description of the drying process. As drying is generally a “slow” process, the entire sample is assumed to be in a state of thermodynamic equilibrium. A quantitative theoretical description of the evaporation of water in capillary structures can be found in [83]. Here only a qualitative description of the process is presented.

Generally drying processes are described by so called drying rate curves. The mass loss of a completely wet porous material during the drying process is a measure of the drying rate [20]. Typical drying rate curves are obtained depending on the structure of the porous material. In most cases the drying process can be divided into different sections. The curve of the drying rate shows typical break points, dividing the first part of the drying process from the second one. In the drying curve shown in Fig. 76 (right) the derivative of the mass with respect to time (the mass loss), which is equivalent to the drying rate, is plotted as a function of time. During the first part of the drying process (I) the drying rate is nearly constant. In the second part of the drying process the rate decreases with time (II).

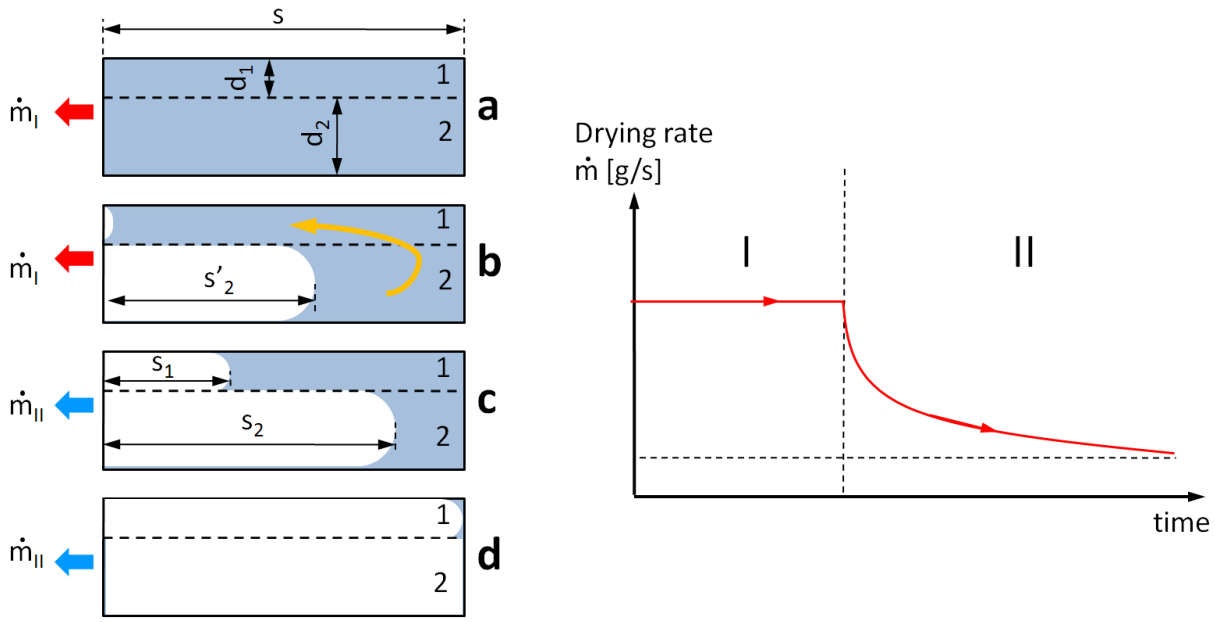

Fig. 76. Left: drying of a system of two capillaries; red / blue arrows indicate the two parts of the drying process; right: typical curve drying rate; adapted from [19].

This behavior will be illustrated based on a simple model of two connected capillaries with different diameters (d_1 and d_2) (Fig. 76 left). At the beginning of the drying process the water evaporates from a flat water surface:

$$\dot{m}_I = \frac{\beta}{RT}\,(P'' - P')\,, \qquad \textbf{(46)}$$

with β the mass-transfer number, P'' the saturated partial water vapor pressure at the surface and P' the partial water vapor pressure of the surrounding air.

Assuming constant environmental conditions, the drying rate remains constant during the first part of the drying process. The respective value can be calculated with equation (46). The evaporated water (from capillary 1) is sucked in by capillary 2. If the capillary force described by the Young- Laplace equation (47) is equal to the friction in the capillary, determined by the Hagen-Poiseuille equation (48), the meniscus starts to move inside the capillary (Fig. 76b) and the break point of the curve of the drying rate can be calculated (for some definitions see Fig. 76):

$$\Delta P_{capillary} = 2\gamma\left(\frac{1}{r_1} - \frac{1}{r_2}\right), \qquad \textbf{(47)}$$

$$\dot{m}' = \frac{r_1^4 \pi \rho}{8\,\eta s_2'}\,\Delta P_{friction}\,, \qquad \textbf{(48)}$$

setting $\Delta P_{friction} = \Delta P_{capillary}$,

leads to

$$\dot{m}' s_2' = \frac{\gamma}{4\eta}\left(\frac{1}{r_1} - \frac{1}{r_2}\right) r_1^4 \pi \rho = \frac{\gamma\rho}{\eta} C_{cap}\,. \qquad \textbf{(49)}$$

The position of the break point is determined by a constant C_{cap} which is dependent on the capillary system. After passing the break point the meniscus at position s_2 cannot move further inside without a simultaneous movement of the meniscus at position s_1 (Fig. 76c). This means the drying level moves inside the capillary system and water vapor diffuses through the dry parts of the capillaries. Therefore equation (46) has to be extended to include diffusion of water vapor:

$$\dot{m}_{II} = \frac{1}{RT}\frac{1}{\frac{1}{\beta}+\frac{s_1 \mu_{diff}}{\delta_{diff}}}(P'' - P') \,, \qquad \textbf{(50)}$$

with δ_{diff} , the diffusion coefficient and μ_{diff} a diffusion resistance factor depending on the actual degree of moisture.

The diffusion reduces the drying rate in the second part of the drying process. The saturated partial water vapor pressure in the capillaries differs from the partial water vapor pressure of the environment, which is assumed to be air.

In the case of vacuum drying, however, the forming gas as well as the environment is water vapor, resulting in vaporization instead of evaporation. In the ideal case the saturated water vapor pressure is equal to that of the environment, which is identical to the pressure in the specimen chamber of the microscope ($P'' = P' = P$), and in this case equation (50) is not valid. The drying rate is determined by the heat which is transported from the environment into the dry parts of the sample. In this case the temperature difference between the environment and the drying front in the porous system as well as the thermal conductivity of the dry parts determine the drying rate:

$$\dot{m}_{II} \propto \frac{1}{\frac{1}{n_\alpha}+\frac{s_1}{\lambda_{th}}}(T_1 - T_2) \,, \qquad \textbf{(51)}$$

with T_1, the temperature of the environment, T_2 the temperature of the drying front, λ_{th} the thermal conductivity of the dry parts of the sample and n_α , the heat transfer number. However the quantities λ_{th}, n_α, δ_{diff}, β and μ_{diff} are dependent on the sample structure (pore structure) as well as on the actual degree of moisture.

The drying process was described at the two limiting cases so far:

- Drying under “ambient” conditions:
  Here equation (46) and (50) are valid as the partial pressures are negligible compared to the overall pressure ($P'', P' \ll P$) and the drying rate is determined by diffusion.

- Drying under vacuum conditions:
  Here equation (51) is valid as only one overall pressure exists ($P'' = P' = P$) and the drying rate is determined by temperature gradients.

It can be assumed that the drying process in the ESEM is affected by temperature as well as by pressure differences. In an ESEM a continuous pumping process takes place, which could cause such a pressure difference and would have to be included in the mathematical calculations of the drying process. The chamber pressure (3.5 Torr during the drying process) is measured by a capacitive gauge (BTG in Fig. 18) located far away from the sample position, and therefore the measured pressure can be different from the pressure close to the sample surface. Unfortunately the actual pressure close to the sample is not measurable.

As the experimental setup did not include a precision balance for measuring mass loss, characteristic temperature curves were obtained by measuring the temperatures at the sample surfaces. The resulting temperature characteristics are typical of the microstructure of individual membranes as described in section 5.3.

5.2 **Surface drying** [4]

As shown in the previous section, the drying level moves from the surface to inner parts of the membrane. As the transport length from the drying level to the surface increases, the capillary forces are no longer able to transport the water to the membrane surface, causing even the smallest pores at the surface to dry up. Once the membrane surface is completely dry, water transport from inner parts of the membrane, e. g. from the separation layer, can only occur in the gaseous state (water vapor).

In the ESEM images of the membrane surface recorded during the drying process water-filled pores appear brighter than dry pores. After segmentation, the equivalent pore diameter of each dry pore was calculated as described in section 3.4.3. This makes it possible to calculate the number, size and size distribution of dry pores as a function of time. A total of 11 images of the DuraPES®600 roll side, 8 images of the MicroPES®6F air side and 13 images of the DuraPES®200 roll side were analyzed during the drying process (analyzed surface area for each membrane type: 180 µm × 157 µm).

Porous structures can generally be characterized using a Log-Normal pore size distribution [84]. During the drying process, however, variations in the distribution can be observed as shown in Fig. 77 to Fig. 79, which display sections of the membrane surfaces, the segmented dry pores and the corresponding pore size distributions (from left to right). The respective images, recorded at the times marked in Fig. 80, show the drying behavior of the MicroPES®6F air side, the DuraPES®200 roll side and the DuraPES®600 roll side. In the case of the MicroPES®6F membrane the pore size distribution of the dry pores shows a Log-Normal distribution for the entire drying process. The DuraPES®600 and DuraPES®200 membranes, in contrast, show a Gaussian distribution at the beginning of the drying process and a Log-Normal distribution at its end. As a consequence, the sum of a Log-Normal and a Gaussian distribution was used for data fitting for the drying process. The differences between the data bars and the fitted curves in Fig. 77a and b as well as in Fig. 78a and b are due to poor statistics caused by the low number of dry pores in the first part of the drying process. Thus, although the pore size distribution of all pores at the membrane surface can be characterized by a Log-Normal distribution, the pores of a specific size may follow a different distribution. In the present case the number of large pores is much smaller than that of the small pores, the latter thus defining the overall Log-Normal distribution.

The mean arithmetic diameter is marked with a vertical line in the pore size distributions. During the drying of the membrane surface the mean diameter of the dry pores of the MicroPES®6F membrane decreases from 3.2 µm to 2.1 µm, that of the DuraPES®200 membrane from 5.75 to 1.8 µm and that of the DuraPES®600 membrane from 5.5 µm to 2.2 µm.

The number of dry pores increases moderately on the air side of the MicroPES®6F, in contrast to the two other membranes, where a modest rise in the first part of the drying process is followed by a very steep increase later on, which is caused by simultaneous drying of the many small pores in between only few large ones.

The assumption that the drying of the separation layer is the last step of the whole drying process cannot be verified directly, however the membrane cross-section can also be observed as shown in section 5.4. On the other hand, the membrane surface temperature characteristics can give additional information about the drying process of the membrane interior, as will be shown in the next section.

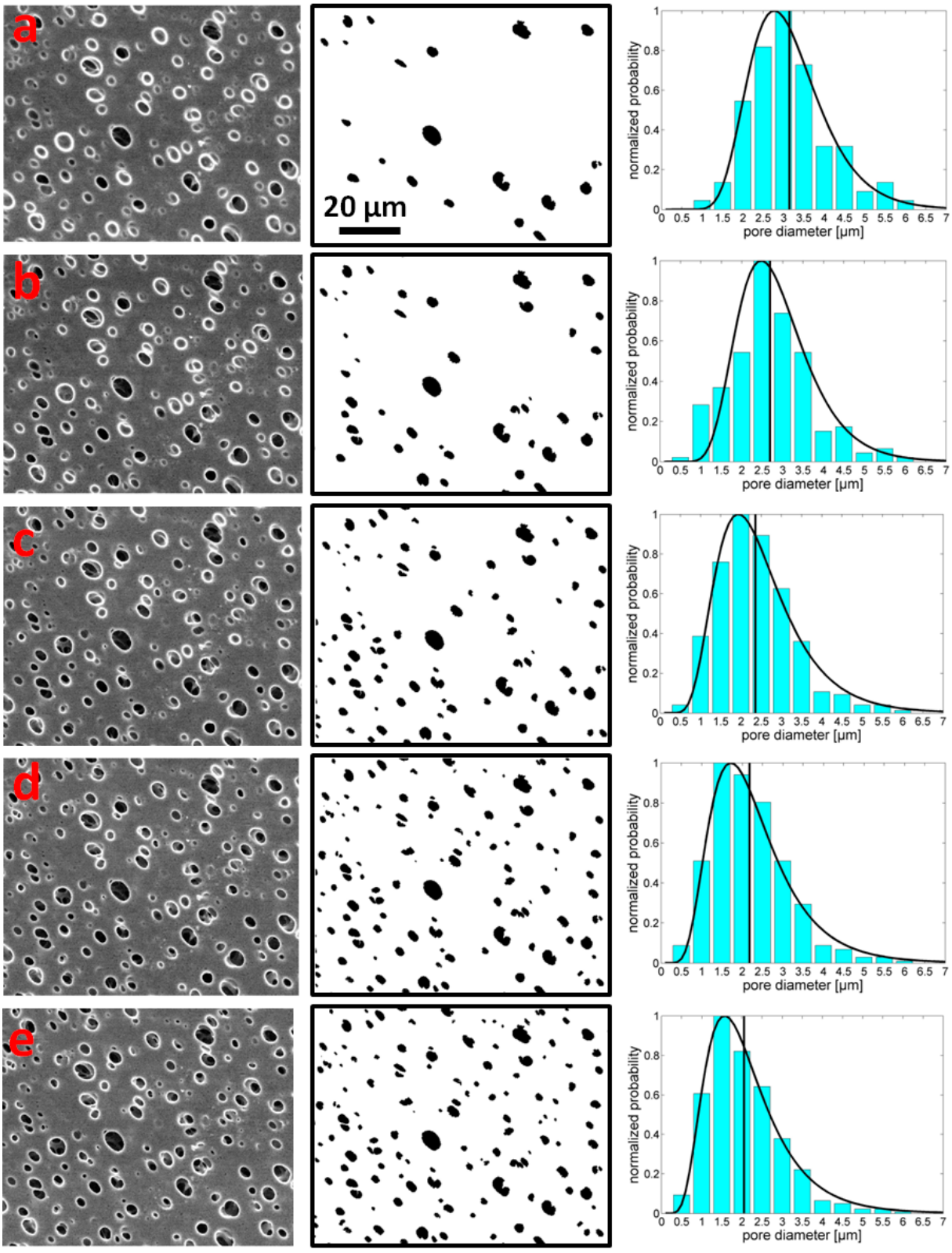

Fig. 77. Drying process on the air side of the MicroPES®6F membrane surface; left: SEM images (ESEM mode, electron energy = 7 keV) of the membrane surface at different stages of drying; center: segmented dry pores; right: pore size distribution of the dry pores; adapted from [4].

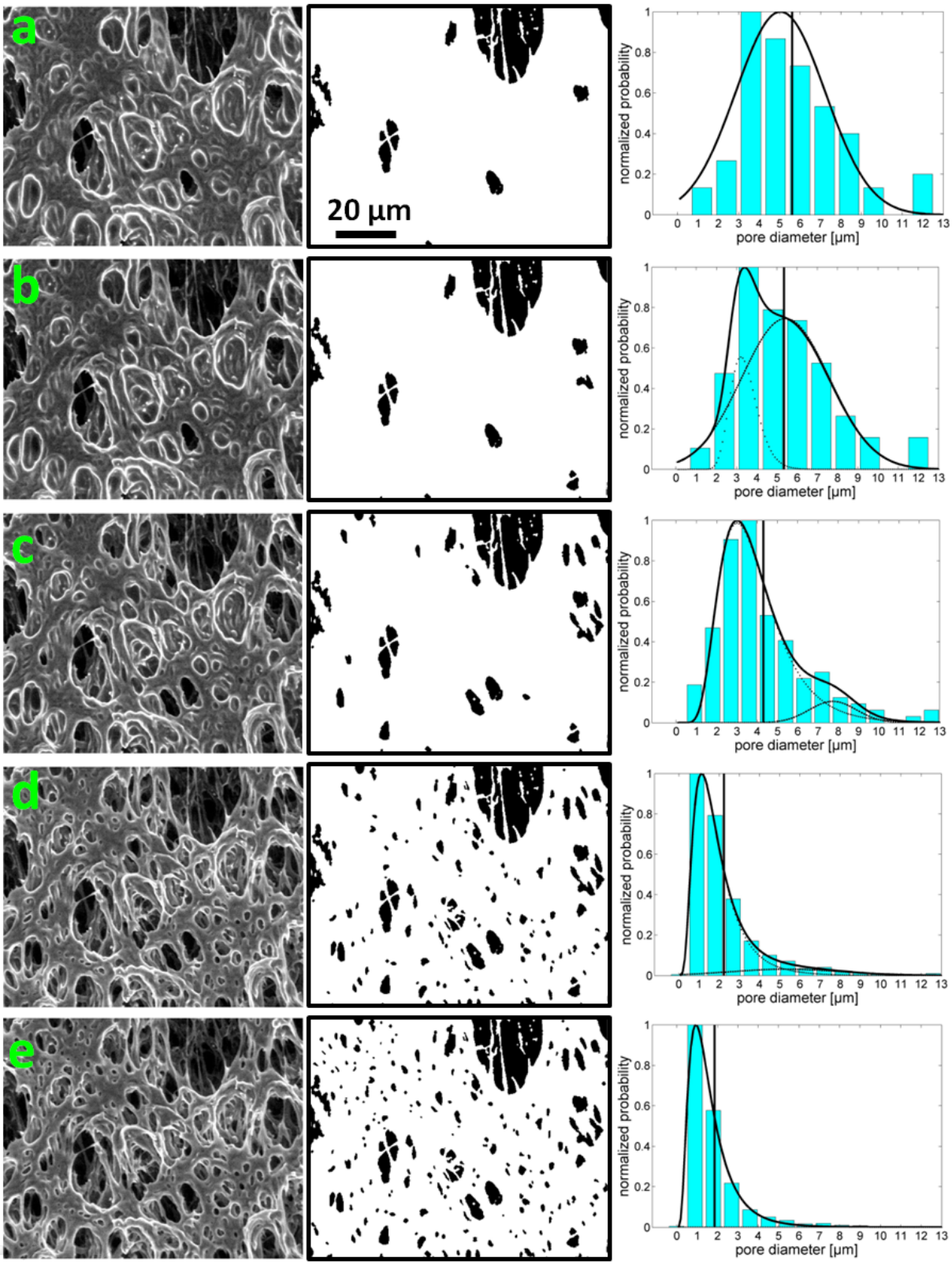

Fig. 78. Drying process on the roll side of the DuraPES®200 membrane surface; left: SEM images (ESEM mode, electron energy = 7 keV) of the membrane surface at different stages of drying; center: segmented dry pores; right: pore size distribution of the dry pores.

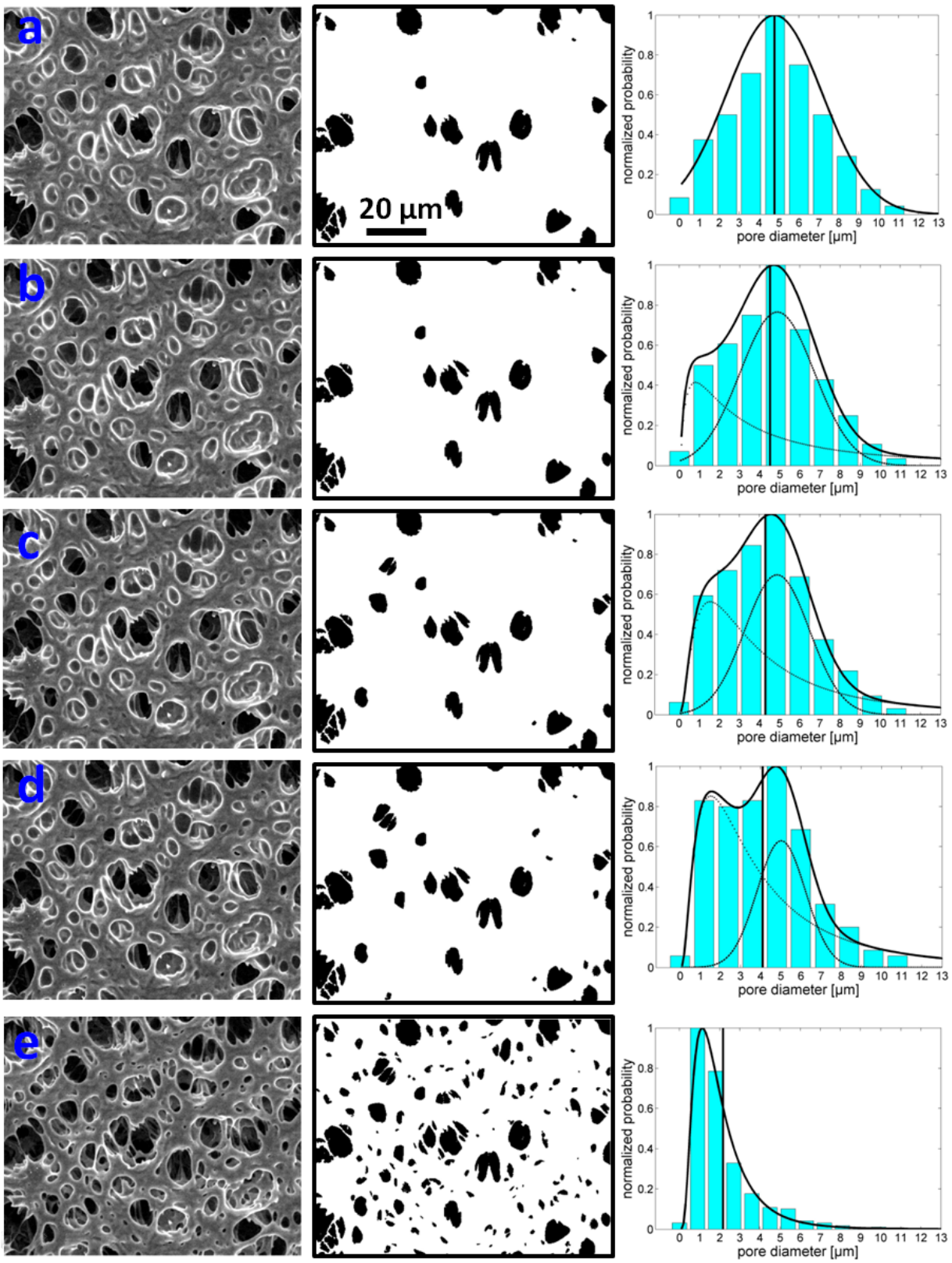

Fig. 79. Drying process on the roll side of the DuraPES®600 membrane surface; left: SEM images (ESEM mode, electron energy = 7 keV) of the membrane surface at different stages of drying; center: segmented dry pores; right: pore size distribution of the dry pores; adapted from [4].

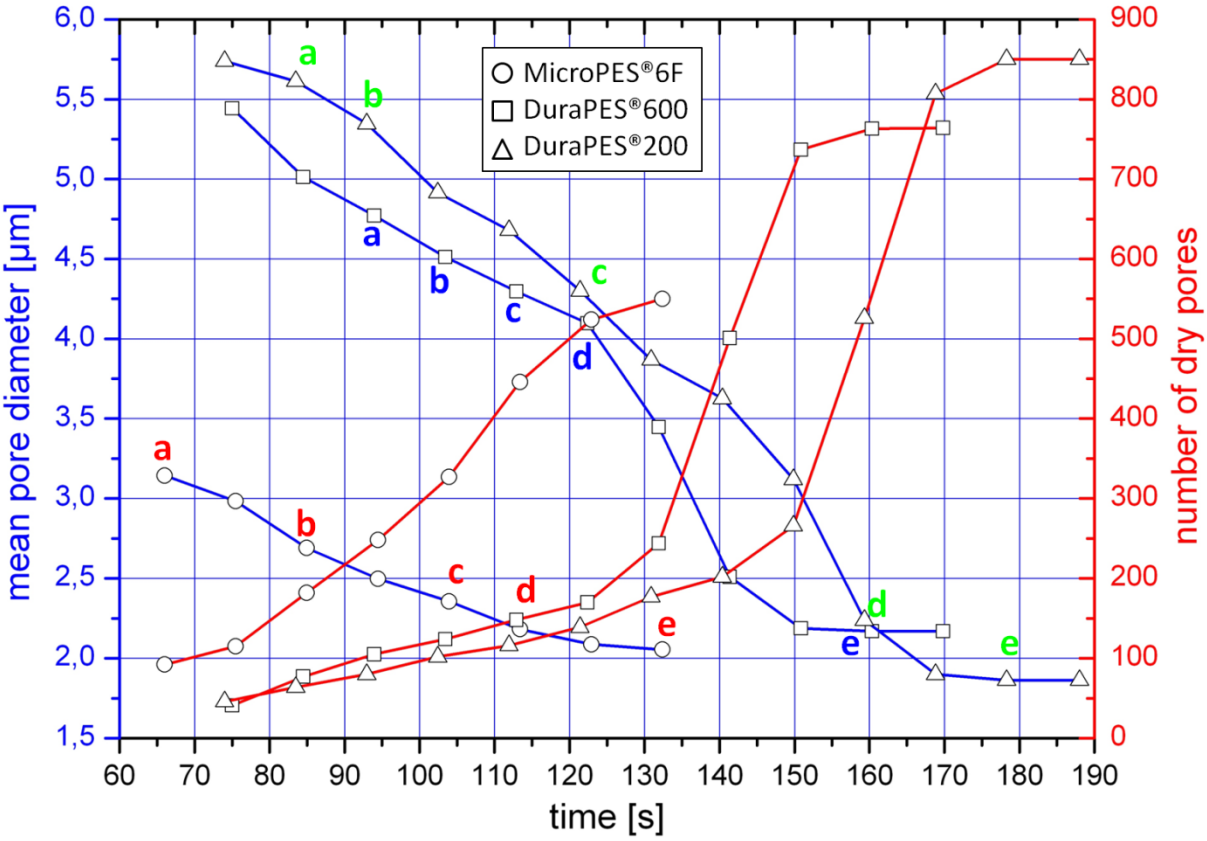

Fig. 80. The number of dry pores and their mean pore size on the air side of the MicroPES®6F and on the roll side of the DuraPES®600 and DuraPES®200 membranes, as a function of the drying time. The time points of recording the images shown in Fig. 77 - Fig. 79 are marked with colored letters; adapted from [4].

5.3 **Temperature characteristics** [4]

In the following, only the drying of the wet membranes will be discussed (right side of the temperature characteristics in Fig. 49 top left and Fig. 81). The temperature at the wet membrane surfaces midway between the cooling clamps is around –2°C. The water is in its super-cooled state. No ice forms because the membrane is very clean and the condensed water contains no seed crystals. The low ESEM chamber pressure and water vapor environment will lead to vaporization instead of evaporation - as discussed in section 5.1.2.

At first, of course, the largest pores at the surfaces start drying, while very small pores stay wet (see also section 5.1.2). If large pores dominate, as e.g. on the roll side of the DuraPES®600 or 200 the vaporizing (drying) level will move fast below the membrane surface. As a consequence, the dry surface layer will start warming up due to the much warmer environment and because it is no longer cooled by the water. But on the other hand, it is still cooled by the water vapor vaporizing from the interior of the membrane. Therefore the temperature rise is only modest, as can be seen in Fig. 81. The beginning of the temperature rise is marked with 1.

An early temperature rise at one of the membrane surfaces thus indicates that the respective surface layer consists mainly of much larger pores than the interior part of the membrane. The larger the pores, the earlier the temperature starts to rise. A temperature rise can only occur, however, if the dry surface layer has a certain thickness. Therefore no such rise is observed on the air side of the investigated membranes, because the separation layer with its small pores is close to this surface. Hence, the difference in the temperatures (marked with ΔT in Fig. 81) measured at the two membrane surfaces is due to the asymmetric structure of the membrane and / or different pore size distributions at the surfaces. With the separation layer centered midway between the two surfaces, a temperature rise would occur at both surfaces. In fouled membranes, with many of the surface pores clogged, the temperature rise would be shifted to a later time.

The time periods during which surface drying occurred on both the roll and air sides are marked with bars in Fig. 81. This information was obtained from the surface images recorded simultaneously with the temperature-time characteristics. The later the start of the drying process at the respective surface, the stronger the capillary forces and the smaller the pores. The later the end of the drying propcess, the smaller the average pore size of the respective layer beneath the surface.

Table 13: The drying time of the air side (left) and roll side (right) for 4 different membranes based on the time values corresponding to the end of the respective bars in Fig. 81. The pore sizes of the respective layers beneath the surface increase from top to bottom (see also Fig. 30). The complete time dependencies of the mean pore size and number of dry pores for the MicroPES®6F, DuraPES®200 and DuraPES®600 membranes are shown in Fig. 80.

Membrane	air side: time at end of surface drying [s]	Membrane	roll side: time at end of surface drying [s]
DuraPES®200	275	MicroPES®2F	240
DuraPES®600	210	MicroPES®6F	220
MicroPES®2F	160	DuraPES®200	180
MicroPES®6F	135	DuraPES®600	170

The sharp increase in the surface temperature at the end of the drying process (marked with a 2 in Fig. 81) indicates that all pores in the membrane interior have dried completely. The membrane surface reaches the temperature of the surrounding gas, which is determined by the temperature in the microscope specimen chamber.

The nominal pore size given by the manufacturer [49] (determined with the bubble-point method see section 2.2.2) differs from the mean pore size at the membrane surface and especially that of the separation layer. The smaller the nominal pore size, however, the smaller generally the mean pore size of the separation layer, determining the retention rate.

The duration of the whole drying process is mainly dependent on the mean pore size of the membrane separation layer and less dependent on the asymmetric pore structure, as can be clearly seen from both Fig. 81 and Table 14. The DuraPES®600 and MicroPES®6F membranes show different asymmetric pore structures, but approximately the same drying times, indicating that the mean pore sizes of the separation layers of the two membranes must be similar. The same is true for the DuraPES®200 and MicroPES®2F membranes.

Table 14: Nominal pore size, duration of the drying process and duration of the temperature differences (ΔT) of the membranes.

Membrane	Nominal pore size [µm]	Duration of the drying process [s]		Duration of ΔT [s]	
		horizontal	vertical	horizontal	vertical
MicroPES®6F	0.6	260	280	40	30
MicroPES®2F	0.2	285	300	80	75
DuraPES®600	0.6	260	280	160	155
DuraPES®200	0.2	290	300	155	150

A change in the chemical nature of the pore surfaces and thus in the contact angle (equation 47) would also change both the start of the temperature rise and the drying time of the membrane.

The drying time of the membranes is also determined by the pressure change after the wetting of the membrane (start of period F in Fig. 49). The lower the final pressure, the shorter the drying time.

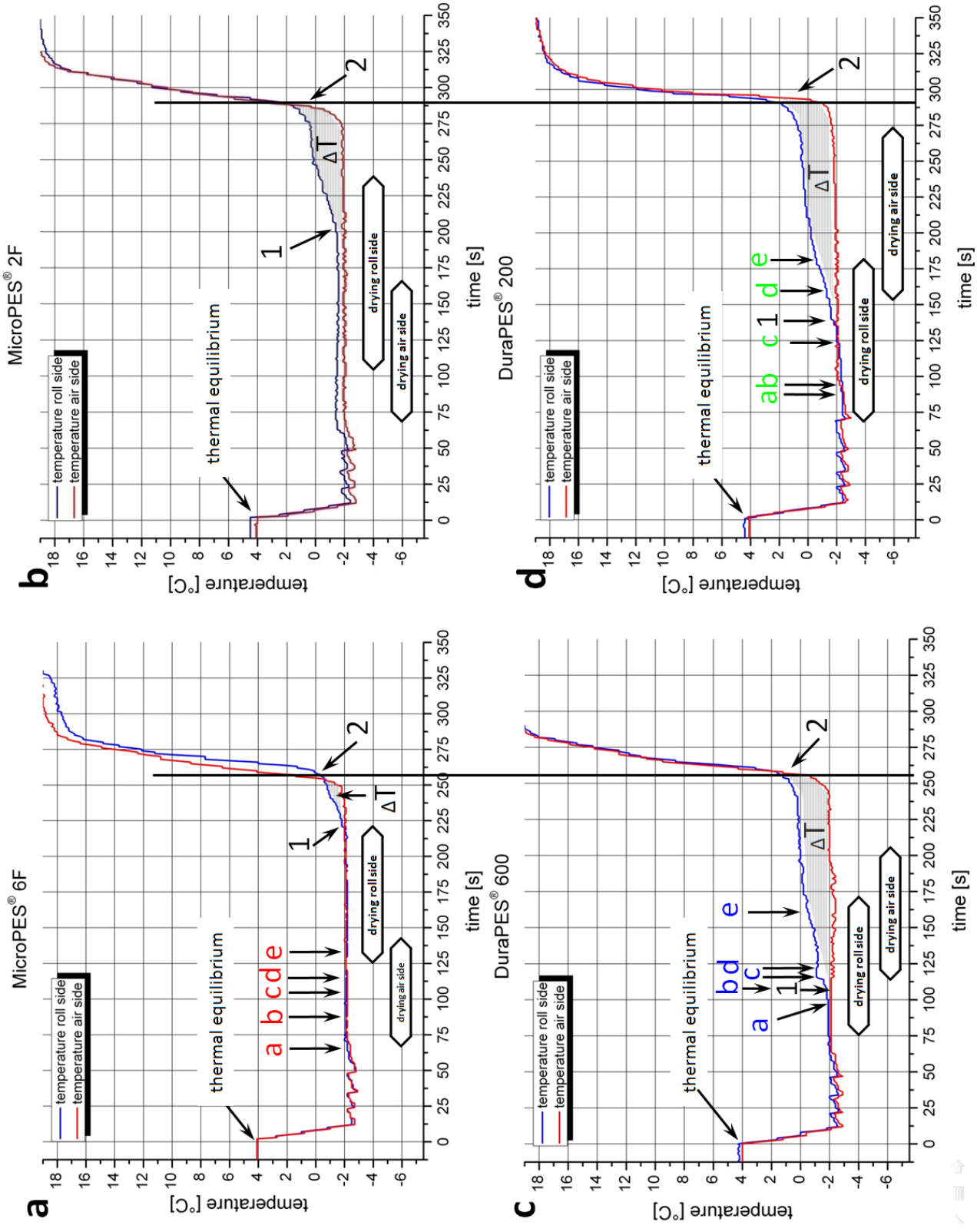

Fig. 81. Temperature characteristics of the membranes investigated. The bars indicate the start and end of surface drying as obtained from the experiments explained in section 5.3. The time points of recording the images shown in Fig. 77 - Fig. 79 are marked with colored letters; adapted from [4].

5.4 Wetting and drying of the cross-sections

The wetting and drying of the membranes was additionally observed at their cross-sections. This should help to get an even better understanding of the drying behavior of the different layers. Therefore the membranes were mounted in a vertical position as described in section 3.3.1. It is obvious that the drying behavior, visible at the membrane cross-section, is different from the drying progress of the "bulk" membrane. The drying level moves from the membrane surface (roll side and air side) as well as from the cross-section surface to the inner part of the membrane. The sequence in which the different layers dry should be visible at the cross-section surface. The DuraPES® type membranes, which have only one separation layer, are expected to dry first at the support layer on the roll side and finally at the separation layer.

Fig. 82 shows the ESEM images of the cross-section recorded during the wetting and drying of the membranes, which were prepared as described in section 3.1.2.1. The images were taken at the times marked in Fig. 83 with the same letters as in Fig. 82. All membranes show first wetting of the separation layer (position marked with 3 in Fig. 82, red arrows). Afterwards a completely wetted cross-section surface becomes visible (marked with red letters in Fig. 82). As expected, the wide structured support layers dry first, while the separation layers stay wet at the beginning of the drying process. Images marked with green letters show a dry separation layer at the cross-section surface. This, however, does not mean that the bulk of the separation layer is also dry. An indication of the final drying step of the separation layer (and thus the complete membrane) is the sharp temperature rise at the end of the drying process - marked with vertical lines in Fig. 83. The MicroPES® membranes show two layers with small pores (see Fig. 30 and Fig. 65), with the separation layer close to the air side and the second layer positioned beneath the roll side. This additional layer is the main reason why the temperature curves of the MicroPES® and DuraPES® membranes do not show the same temperature characteristics on the roll side (duration of ΔT is different).

The temperature curves of the membranes investigated vertically are similar to those investigated in horizontal position (compare Fig. 81 and Fig. 83). However, the duration of the complete drying process is longer (see Table 14), which is due to the fact that the cooling clamps used for horizontal and vertical membrane mounting were different (see section 3.3.1). The fact that the temperature curves obtained in horizontal and vertical position are comparable shows the repeatability and reliability of the experiments.

The drying behavior of the Sartorius 15406 membrane was only investigated in vertical position (cross-section). The main structural difference to the other membranes investigated is that the separation layer is thicker than that of the other membranes positioned nearly in the middle of the cross-section. Due to the symmetry the temperature curves at both membrane sides show nearly the same characteristics. The complete drying process lasts longer (320 sec.) than for the other membranes, which is due to the thick separation layer and the lack of large pores at the surface (see Fig. 31 and Fig. 65).

This study verifies the movement of the drying level from the surface to the interior and clearly shows a stepwise drying of the different membrane layers.

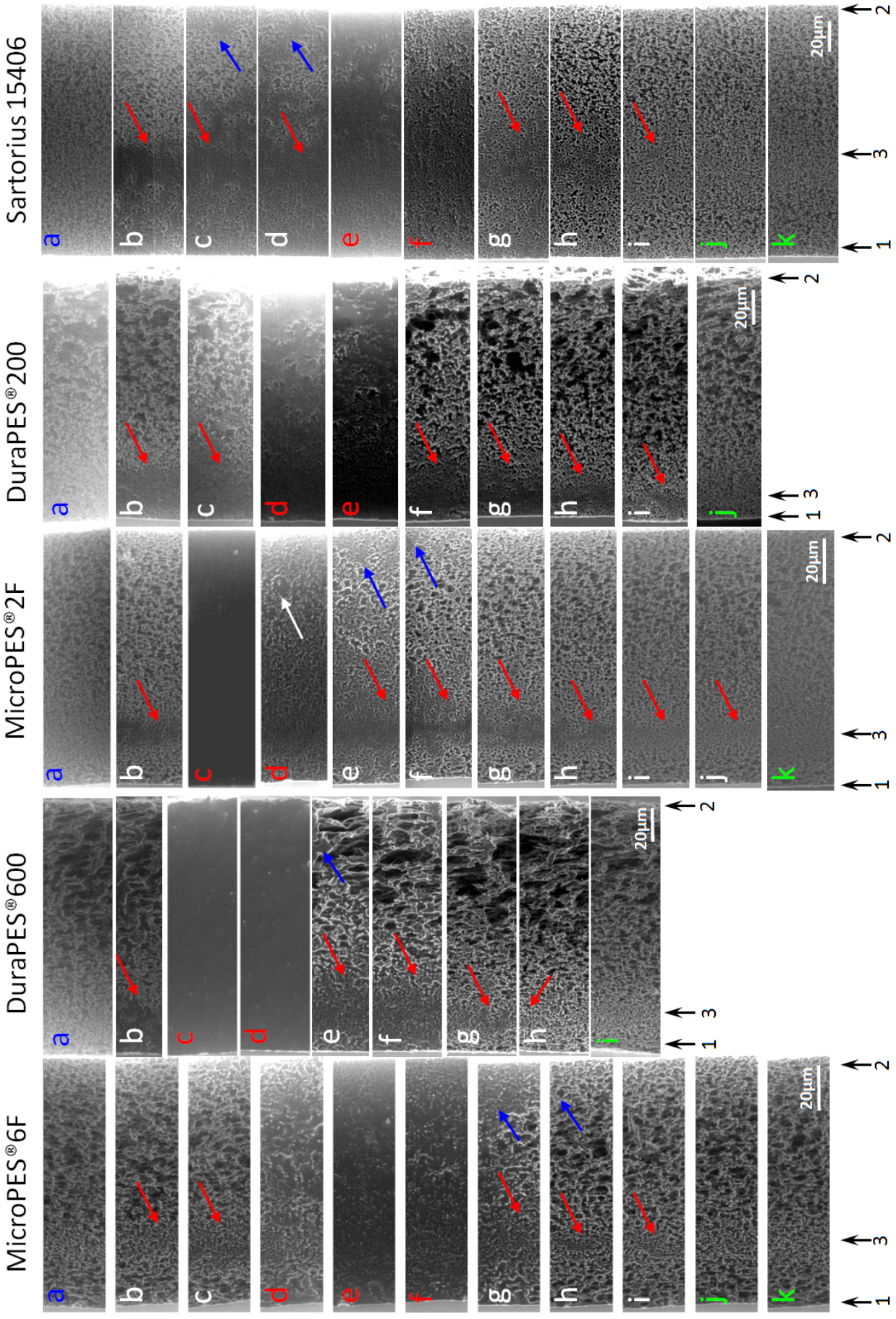

Fig. 82. Images of the wetting and drying progress at the cross-section of the membranes, red arrows mark the drying of the separation layer, blue arrows mark the drying of the layer on the air side (see text). 1: air side, 2: roll side, 3: separation layer (ESEM mode, electron energy = 7 keV).

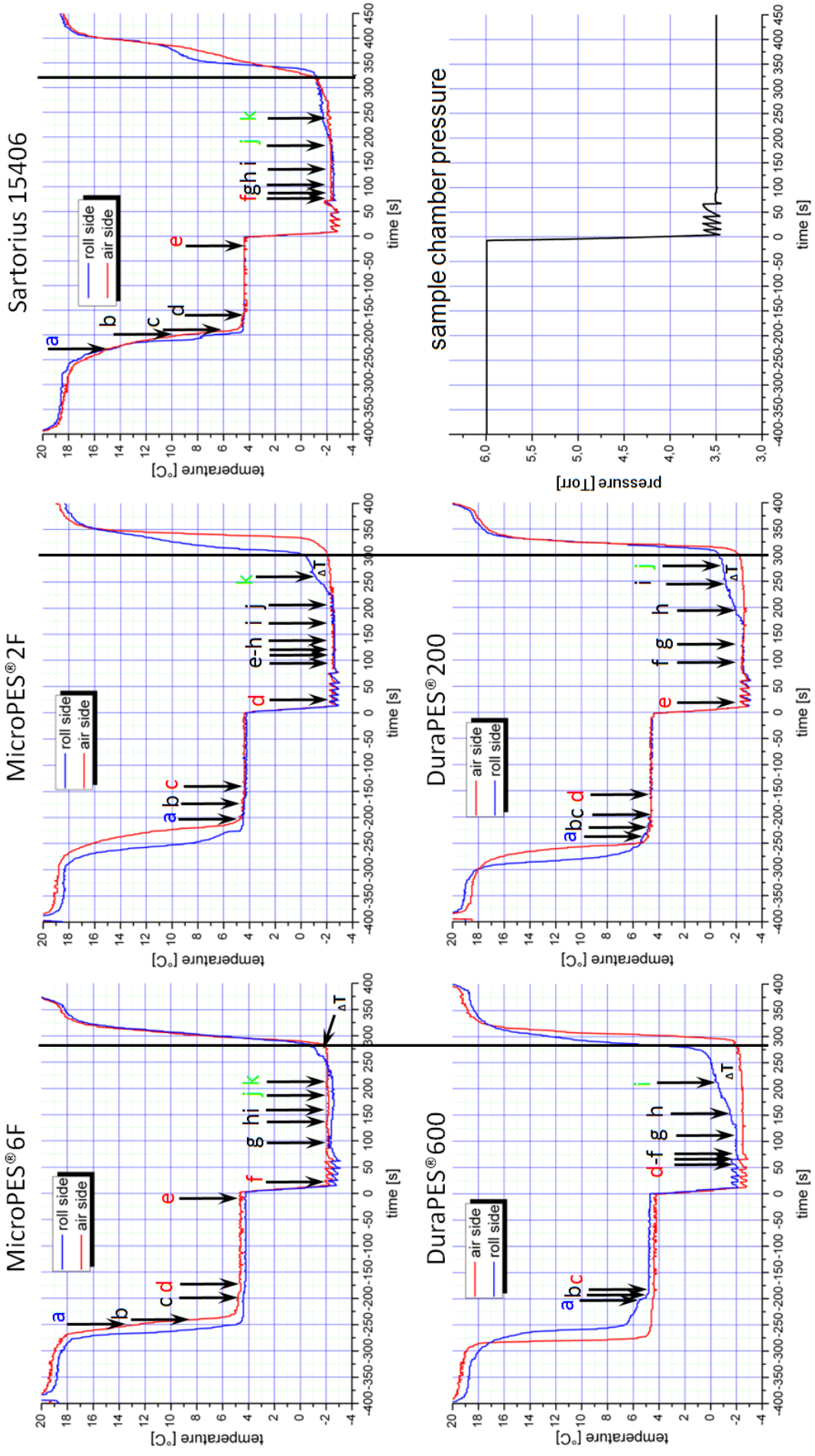

Fig. 83. Temperature characteristics of the membranes investigated in vertical position, more information can be found in the text.

5.5 **Radiation damage**

Kitching et *al.* studied the influence of the electron beam on polypropylene under wet conditions in the ESEM [85]. They used FTIR for determining the chemical changes caused by the irradiation and observed polymer hydrolysis and oxidation. This effect was enhanced in the presence of water.

Three precautions were taken to reduce unwanted influences caused by the electron beam during imaging: Firstly, the electron beam energy was reduced to 7 keV. Secondly, the area in which the wetting / drying process was recorded was not irradiated before the actual start of imaging. Focusing and adjustment of contrast and brightness was performed in a neighboring area. And finally, a large area of 180 µm width was chosen for image recording. The small pores were still clearly visible at this magnification. Nevertheless, the impact of the electron beam on the PES membrane material was investigated by irradiation of two regions of the Sartorius 15406 membrane. The microscope parameters used in the experiment are listed in Table 15. The irradiated regions at the membrane surface are marked position 1 and position 2 in Fig. 84c.

Table 15: Microscope parameters used for beam damage analysis

	Beam energy [keV]	Spot size	WD [mm]	Dwell time [µs]	Image width [µm]	Irradiation time [s]
Position 1	20	5	7.8	10	180	460
Position 2	7	5	7.9	10	180	460

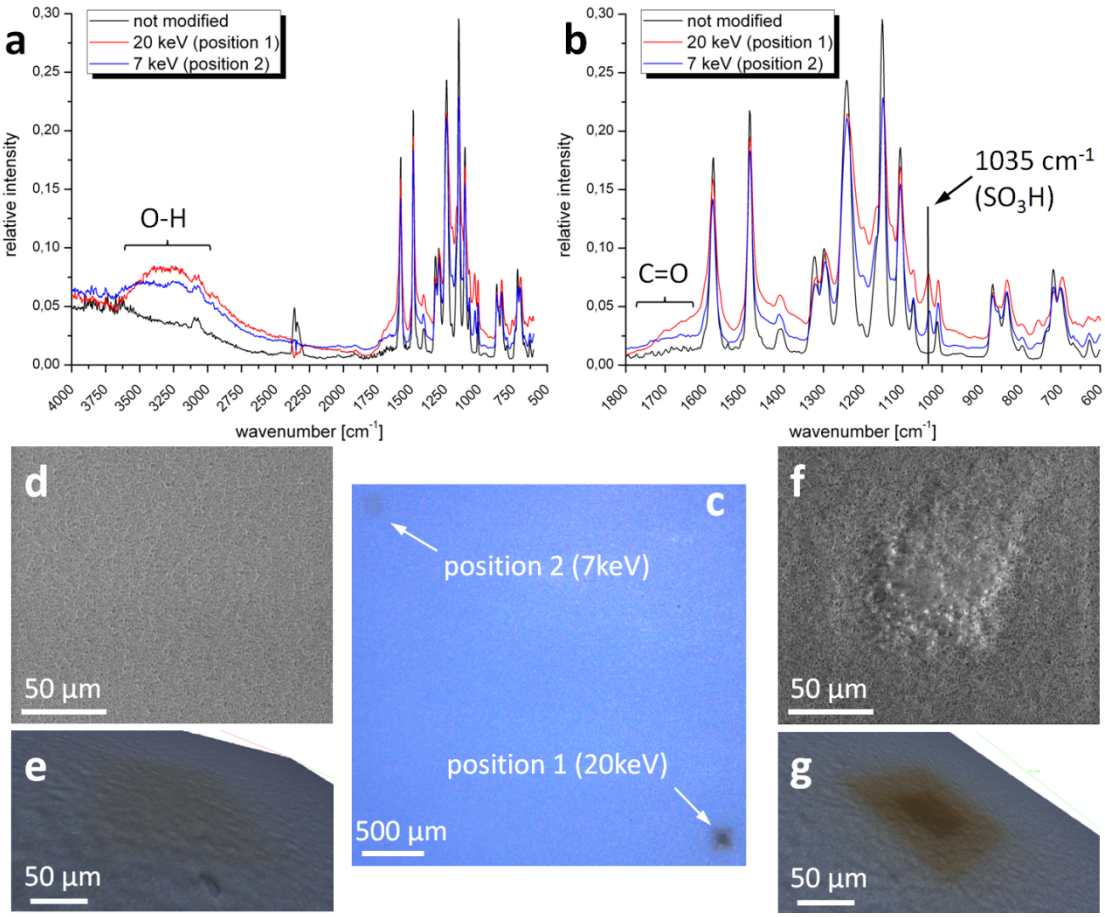

Fig. 84. Impact of electron irradiation on the Sartorius 15406 PES membrane material. a: complete FTIR spectra; b: stretched part of the FTIR spectra; c: LiMi image with positions of the irradiated regions; d: SEM image of position 2 (SE); e: light microscopic image of position 2; f: SEM image of position 1 (SE); g: light microscopic image of position 1.

Both regions were irradiated for a period of 460 seconds, which corresponds to the maximal length of the complete drying process and is much longer than the actual time used for image recording during the wetting experiments. Subsequently, the irradiated regions were investigated by FTIR using the same equipment as described in section 3.1.3. The spectrum in Fig. 84a shows an increased absorption in the range around 3400 cm^{-1}(hydroxyl species (O – H)). The spectrum in Fig. 84b additionally shows increased absorption in the range of 1700 cm^{-1} (carbonyl (C = O)). A peak appeared at 1035 cm^{-1} showing the formation of sulfonic acids. The respective changes of the polymer composition were substantially lower at lower electron energies. These results are in agreement with the study of Kitching [85].

5.6 **Further improvements and outlook** [4]

In the present work, the surfaces of the pore walls of all membranes investigated were hydrophilic. Membranes with the same morphology but different surface properties (partly hydrophobic / hydrophilic surface) should have different temperature characteristics. Fouled membranes with blocked surface pores may also show a longer drying process. Future investigations will thus also include membranes with the same structure but modified pore surface properties.

Additional information may be provided by one-sided drying experiments, where one side of the membrane is covered. The temperature characteristics measured should differ from those obtained from double-sided drying experiments and thus give further information about the drying process and the membrane structure.

Improvements in the wetting of the membrane from the water condensed at the cooling clamps could lead to a better repeatability of the process. This could be achieved by newly designed cooling clamps made from stainless steel, as brass seems to be prone to corrosion. A better, more accurate temperature control of the cooling clamps with reduced transient effects could also help to obtain more reliable information.

Mounting the current experimental setup on a balance and additionally measuring the mass change during the wetting / drying experiments could help both to gain new information on the membrane structure and behavior and to interpret the temperature characteristics in more detail. The drying rate curve and typical break points (see section 5.1.2) in particular could be correlated with the images recorded during the drying process and the temperature characteristics. Sufficiently accurate balance systems are commercially available (from Sartorius or Mettler Toledo). The complete cooling setup including a power supply has to be mounted on the balance. The control of the cooling system should be wireless, because connection wires could distort the measurement results.

The mechanical properties of flat as well as hollow fiber membranes and their fracture behavior can be tested with a tensile stage mounted inside the microscope chamber. Membrane manufacturers are especially interested in the morphological change of the pores under mechanical strain. Such measurements could help to identify the maximum mechanical load that can be applied on the membrane matrix.

5.7 **Conclusions** [4]

In the previous section a new method for membrane characterization under wet conditions was presented. As the pressure range in the microscope chamber is limited, the investigations were performed under low vacuum conditions. If water vapor is used as the chamber gas, the relative humidity in the specimen chamber is determined by the pressure. However, the ESEM sample chamber is a microlaboratory, where well defined conditions (pressure, humidity, temperature) can be adjusted in order to obtain reproducible and comparable data.

Membranes with various morphologies were investigated. The wetting and drying of the pores at the membrane surfaces was observed at high resolution in the ESEM. As a result, both the number and the size distribution of the dry pores at the surface were measured as a function of time during the drying process. In order to gain information about the drying process in the membrane interior, the temperature changes at the membrane surfaces wetted with cooled water were recorded as a function of time. These temperature characteristics reflect the porous structure of the membrane and therefore

provide information about membrane asymmetries, mean pore size, the position of the separation layer, pore size changes along the cross-section of the membrane, changes in the chemical nature of the pore surfaces etc.

Widespread defects inside the membrane microstructure, especially in the separation layer, can have a large impact on membrane performance and safety. The volume investigated in the present experiments, however, is large enough to be able to detect such defects as they should modify the respective temperature-time characteristics.

Some parts of the presented method are time consuming. Semi-automatic image segmentation in particular is not suited for “fast” membrane characterization. However, the work shows new “alternative” techniques for membrane characterization, which can be essential when conventional methods deliver ambiguous results and which could be a helpful tool especially in connection with the design and development of new membranes.

6 Overall conclusions

In the present work two new electron microscopic methods for the characterization of polymeric microfiltration membranes were presented. They have the potential to further expand the pool of established methods for membrane characterization. 3D reconstructions can provide quantitative data about the membrane structure like specific surface area, volume porosity, connectivity and tortuosity, but also parameters like permeability and membrane resistance. These models may also be used as input for finite element simulations for calculating fluid flow, but also mechanical parameters like the influence of mechanical stress on the membrane structure. Wetting and drying experiments enable measurement of the hydrophilic / hydrophobic properties of the pore surfaces and their changes with time, which are not easily accessible with other methods, but also provide information about the membrane structure, albeit on a more qualitative basis. Possibly they can also help to get a better understanding of how fouling changes the fluid flow.

Automated serial slicing and imaging directly in the microscope is a prerequisite for obtaining the data necessary for 3D reconstruction within acceptable time. Traditional techniques would be far too time-consuming. Two such tools are currently available: automated ultramicrotomy and focused ion beam instruments, with the former being the method of choice for polymeric materials like the membranes investigated in this work. But the data must subsequently be processed and this is where image processing comes into play. Only the sophisticated routines for image restoration, enhancement and analysis provided by today's image processing programs enable both successful 3D reconstruction and the extraction of the relevant data. The widely spread availability of powerful workstations makes computer fluid dynamics calculations (CFD) and finite element methods (FEM) possible.

The opportunity to monitor the interaction of a sample surface with water both at high resolution and great depth of focus is a key advantage of *in situ* experiments in an environmental scanning electron microscope. But this instrument provides no direct information about what is going on in the interior of the material during the experiment. Therefore a parameter had to be found that could provide this information, which turned out to be the temperature at the sample surfaces. Accurate temperature measurements at the membrane surface proved a great experimental challenge, but were successfully mastered. The correlation of the temperature characteristics with the images of the membrane surface provided both information about the membrane structure and a basic understanding of the dynamic wetting and drying process.

List of publications

Peer - reviewed articles:

- H. Reingruber, A. Zankel, C. Mayrhofer, and P. Poelt. Quantitative characterization of microfiltration membranes by 3D reconstruction. J.Membr.Sci., 372 (2011) 66.
- H. Reingruber, A. Zankel, C. Mayrhofer, and P. Poelt. A new in situ method for the characterization of membranes in a wet state in the environmental scanning electron microscope. J.Membr.Sci., 399 - 400 (2012) 86.
- T. Koch, D. Salaberger, A. Zankel, H. Reingruber, A. Steiger-Thirsfeld, Y. Voronko, et al. Methods for Characterizing the 3-D Morphology of Polymer Composites. Macromolecular Symposia, 315 (2012) 115.

Journal articles:

- A. Zankel, H. Reingruber, H. Schroettner. 3D Elemental Mapping in the ESEM. Imaging & microscopy 2 (2011), S. 35 - 37.
- H. Reingruber, A. Zankel, P. Poelt. Filtration Membranes, Water and the ESEM. Imaging & microscopy 3 (2011), S. 18 - 21.

Conference proceedings:

- H. Reingruber, P. Poelt. The ESEM and Water in Proceedings MC 2009 First Joint Meeting of Dreiländertagung & Multinational Congress on Microscopy. (2009) S. 355 - 356.
- H. Reingruber. New micro scale methods for the characterization of fluid and gas transport through membranes. Proceedings ICAPM2009. (2009) S. 150 - 154.
- H. Reingruber, A. Zankel, P. Poelt. New micro scale methods for the Characterization of fluid and gas transport through membranes. Proceedings Micro Science 2010 (2010) S. 0116.
- H. Reingruber, A. Zankel, P. Poelt. New microscopic methods for characterizing filtration membranes. Proceedings 13. Aachener Membran Kolloquium. (2010) S. 753 - 755.
- H. Reingruber. New microscopic characterization methods for porous polymeric membranes. Proceedings ICOM 2011 S. ICOM609.
- H. Reingruber, A. Zankel, H. Schroettner, P. Poelt. 3D reconstruction of organic and inorganic materials using *in situ* ultramicrotomy. Proceedings Microscopy Conference 2011 (2011), S. IM3.P140.
- H. Reingruber, A. Zankel, P. Poelt. New microscopic methods for characterizing micro filtration membranes. Abstract Book WFC11 World filtration Congress 2012 S. 158 and electronic Proceedings L19.

Conference talks:

- H. Reingruber. New micro scale methods for the characterization of fluid and gas transport through membranes. At ICAPM2009 in Istanbul; 11.08.2009.

- H. Reingruber, A. Zankel, P. Poelt. New microscale methods for the characterization of fluid and gas transport through membranes. At Micro Science2010 in London; 30.06.2010.

- H. Reingruber, A. Zankel, P. Poelt. New microscopic characterization methods for porous polymeric membranes. At ICOM2011 in Amsterdam; 27.07.2011.

- H. Reingruber, A. Zankel, P. Poelt. New microscopic methods for characterizing micro filtration membranes. At WFC11 World filtration Congress 2012 in Graz; 19.04.2012.

- H. Reingruber, A. Zankel, P. Poelt: New advanced microscopic methods for detailed analysis of strong asymmetric micro filtration membranes. At 62nd Annual meeting of the Austrian physical society in Graz; 20.09.2012

Conference posters:

- H. Reingruber, P. Poelt. *In situ* investigations of porous membranes in a wet environment in the ESEM. At MC 2009 First Joint Meeting of Dreiländertagung & Multinational Congress on Microscopy in Graz; Poster Nr.: M5.P347.

- H. Reingruber, A. Zankel, P. Poelt. New microscopic methods for characterizing filtration membranes. Proceedings 13. At the Aachener Membran Kolloquium in Aachen 2010; Poster Nr. P13.2.

- H. Reingruber, A. Zankel, H. Schroettner, P. Poelt. 3D reconstruction of organic and inorganic materials using *in situ* ultramicrotomy. At Microscopy Conference 2011 in Kiel; Poster Nr. IM3.P140.

- P. Poelt, H. Reingruber, A. Zankel. 3D reconstruction & *in situ* characterization of microfiltration membranes in the ESEM. At Euromembrane Conference 2012 in London; Poster Nr. P2.139

References

[1] A.G. Fane. Membranes and the watercycle: challenges and opportunities, Proceedings 13th Aachener membran Kolloquium, 1 (2010) 65.

[2] J. Pellegrino. Membrane characterization: it just keeps on going better, Proceedings ICOM 2011, (2011) ICOM1862.

[3] H. Reingruber, A. Zankel, C. Mayrhofer, and P. Poelt. Quantitative characterization of microfiltration membranes by 3D reconstruction. J.Membr.Sci., 372 (2011) 66.

[4] H. Reingruber, A. Zankel, C. Mayrhofer, and P. Poelt. A new in situ method for the characterization of membranes in a wet state in the environmental scanning electron microscope. J.Membr.Sci., 399 - 400 (2012) 86.

[5] F.H. She, K.L. Tung, and L.X. Kong. Calculation of effective pore diameters in porous filtration membranes with image analysis. Robot.Comput.Integrated Manuf., 24 (2008) 427.

[6] I. Masselin, L. Durand-Bourlier, J. Laine, P. Sizaret, X. Chasseray, and D. Lemordant. Membrane characterization using microscopic image analysis. Journal of Membrane Science, 186 (2001) 85.

[7] Y. Wyart, G. Georges, C. Deumié, C. Amra, and P. Moulin. Membrane characterization by microscopic methods: Multiscale structure. J.Membr.Sci., 315 (2008) 82.

[8] R. Ziel, A. Haus, and A. Tulke. Quantification of the pore size distribution (porosity profiles) in microfiltration membranes by SEM, TEM and computer image analysis. J.Membr.Sci., 323 (2008) 241.

[9] T. Sarada, L.C. Sawyer, and M.I. Ostler. Three dimensional structure of celgard® microporous membranes. J.Membr.Sci., 15 (1983) 97.

[10] M. Schaffer, J. Wagner, B. Schaffer, M. Schmied, and H. Mulders. Automated three-dimensional X-ray analysis using a dual-beam FIB. Ultramicroscopy, 107 (2007) 587.

[11] W. Denk, H. Horstmann. Serial Block-Face Scanning Electron Microscopy to Reconstruct Three-Dimensional Tissue Nanostructure. PLoS Biol, 2 (2004) e329.

[12] C. Ho, A.L. Zydney. Measurement of membrane pore interconnectivity. J.Membr.Sci., 170 (2000) 101.

[13] S. Nakao. Determination of pore size and pore size distribution: 3. Filtration membranes. J.Membr.Sci., 96 (1994) 131.

[14] S. Ramaswamy, A.R. Greenberg, and M.L. Peterson. Non-invasive measurement of membrane morphology via UFDR: pore-size characterization. J.Membr.Sci., 239 (2004) 143.

[15] D.L. Green, L. McAmish, and A.V. McCormick. Three-dimensional pore connectivity in bi-axially stretched microporous composite membranes. J.Membr.Sci., 279 (2006) 100.

[16] F.H. She, D. Gao, W.M. Gao, D.Y. Wu, Z. Peng, M. Hoang, et al. Characterization of membranes with X-ray ultramicroscopy. Desalination, 236 (2009) 179.

[17] J. Remigy, M. Meireles. Assessment of pore geometry and 3-D architecture of filtration membranes by synchrotron radiation computed microtomography. Desalination, (2006) 501.

[18] R. de la Parra. A method to detect variations in the wetting properties of microporous polymer membranes. Micros Res Tech., 25 (1993) 362.

[19] O. Krischer, W. Kast. Die wissenschaftlichen Grundlagen der Trocknungstechnik, Berlin, Springer, 1978.

[20] E. Staude, J. Passlack. Characterization of ultrafiltration membranes by drying. J.Membr.Sci., 28 (1986) 209.

[21] F. Wechs. Integral asymmetric polyethersulfone membrane, process for its manufacture and its use in ultrafiltration and microfiltration. , B01D69/00; B01D71/68; C08J3/09; C08J9/28; D01D5/247; D01F6/00; D01F6/76; (IPC1-7): B01D69/00; B01D71/68, EP0361085, 1990.

[22] M. Mulder. Basic principles of membrane technology, Dordrecht [u.a.], Kluwer, 1991.

[23] G. Gottstein. Physikalische Grundlagen der Materialkunde, Berlin, Springer, 2001.

[24] M. Ulbricht, O. Schuster, W. Ansorge, M. Ruetering, and P. Steiger. Influence of the strongly anisotropic cross-section morphology of a novel polyethersulfone microfiltration membrane on filtration performance. Separation and Purification Technology, 57 (2007) 63.

[25] P.J. Flory. Thermodynamics of High Polymer Solutions. J.Chem.Phys., 10 (1942) 51.

[26] D.R. Lloyd, S.S. Kim, and K.E. Kinzer. Microporous membrane formation via thermally-induced phase separation. II. Liquid-liquid phase separation. J.Membr.Sci., 64 (1991) 1.

[27] Č. Stropnik, V. Kaiser. Polymeric membranes preparation by wet phase separation: mechanisms and elementary processes. Desalination, 145 (2002) 1.

[28] Membrana GmbH Wuppertal. Prüfvorschrift: Bestimmung der Volumenporosität an synthetischen Membranen. (1999).

[29] DIN 58355 Membranfilter Teil 1 - 6. Beut Verglag GmbH, (2005).

[30] J. Goldstein, D. Newbury, D. Joy, P. Echlin, C. Lyman, and E. Lifshin. Scanning Electron Microscopy and X Ray Microanalysis, 2003.

[31] L. Reimer. Scanning Electron Microscopy, Springer, 1998.

[32] D.J. Stokes. Principles and Practice of Variable Pressure/Environmental Scanning Electron Microscopy (VP-ESEM), John Wiley & Sons, Ltd, 2008.

[33] D.W. Tuggle, J.Z. Li, and L.W. Swanson. Point cathodes for use in virtual source electron optics. J.Microsc., 140 (1985) 293.

[34] K. Kanaya and S. Okayama. Penetration and energy-loss theory of electrons in solid targets. J.Phys.D, 5 (1972) 43.

[35] N.F. Mott, H.S.W. Massey. The theory of atomic collisions. Third edition, London, Oxford University Press, 1965.

[36] Kerr GmbH Technische Kunststoffe Großmaischeid. Werkstoffdatenbank RIWETA 4.1.

[37] D. Drouin, A.R. Couture, D. Joly, X. Tastet, V. Aimez, and R. Gauvin. CASINO V2.42 A Fast and Easy-to-use Modeling Tool for Scanning Electron Microscopy and Microanalysis Users. Scanning, 29 (2007) 92.

[38] W. Reuter. Proc. 6th Intern. Conf. on X-Ray Optics and Microanalysis, (1972) 121.

[39] H. Seiler. Secondary electron emission in the scanning electron microscope. J.Appl.Phys., 54 (1983) R1.

[40] W. Umrath. Grundlagen der Vakuumtechnik. (1997).

[41] B.L. Thiel. Master curves for gas amplification in low vacuum and environmental scanning electron microscopy. Ultramicroscopy, 99 (2004) 35.

[42] J. Rattenberger, J. Wagner, H. Schroettner, S. Mitsche, and A. Zankel. A method to measure the total scattering cross section and effective beam gas path length in a low - vacuum SEM Scanning, 31 (2009) 1.

[43] B.L. Thiel, I.C. Bache, A.L. Fletcher, P. Meredith, and A.M. Donald. An improved model for gaseous amplification in the environmental SEM. J.Microsc., 187 (1997) 143.

[44] A. von Engel. Ionized Gases, Oxford, Clarendon Press, 1965.

[45] G.D. Danilatos. Theory of the Gaseous Detector Device in the Environmental Scanning Electron Microscope, in Anonymous , Advances in Electronics and Electron Physics, Academic Press, 1990, pp. 1 - 102.

[46] K. Joshipura, M. Vinodkumar. Cross sections and other parameters of e^- - H_2O scattering ($E_i < 50$ eV), Pramana, 47 (1996) 57.

[47] G.D. Danilatos. Foundations in environmental scanning electron microscopy. Advances in electronics end electron physics, 71 (1988) 109.

[48] C.P. Royall, B.L. Thiel, and A.M. Donald. Radiation damage of water in environmental scanning electron microscopy. Journal of Microscopy, 204 (2001) 185.

[49] Membrana GmbH Wuppertal. MicroPES®, DuraPES® Data Sheet.

[50] Sartorius Stedim Biotech. Mircofilters Product Overview, (2010).

[51] G. Michler, W. Lebek. Ultramikrotomie in der Materialforschung. München, Hanser, 2004.

[52] R. Garcia. Amplitude Modulation Atomic Force Microscopy, Weinheim, Wiley-VCH, 2010.

[53] P.R. Griffiths. A. James, Fourier Transform Infrared Spectrometry, John Wiley, 2007.

[54] H. Günzler, H.U. Gremlich. IR-Spektroskopie - eine Einführung, Wiley-VCH, 2003.

[55] S. Leighton. SEM Images of block faces, cut by a miniature microtome within the SEM - a technical note Scan Electron Microsc., 2 (1981) 73.

[56] A. Zankel, B. Kraus, P. Poelt, M. Schaffer, and E. Ingolic. Ultramicrotomy in the ESEM, a versatile method for materials and life sciences. J.Microsc., 233 (2009) 140.

[57] G.D. Danilatos. Design and construction of an atmospheric or environmental SEM (part 1). Scanning, 4 (1981) 9.

[58] G.D. Danilatos, J.V. Brancik. Observation of liquid transport in the ESEM, Proc. 44th Annual Meeting EMSA, (1986) 678.

[59] Omega® Newport Germany. Thermoelement Referenztabellen.

[60] B. Sundqvist. Thermal diffusivity and thermal conductivity of Chromel, Alumel, and Constantan in the range 100-450 K. Journal of Applied Physics, 72 (1992) 539.

[61] C. Groth, G. Müller. FEM für Praktiker - Band 3: Temperaturfelder Renningen, expert Verlag, 2009.

[62] R. Leary, R. Brydson. Characterisation of ESEM conditions for specimen hydration control, Journal of Physics: Conference Series, 241 (2010) 012024.

[63] R. Gonzalez, R. Woods, and S. Eddins. Digital Image Processing Using MATLAB, Gatesmark Publishing, 2009.

[64] N. Otsu. A Threshold Selection Method from Gray-Level Histograms. Systems, Man and Cybernetics, IEEE Transactions on, 9 (1979) 62.

[65] C.J. Russ. The image processing Handbook, Boca Raton, CRC Press, 2007.

[66] B. Fischl, E.L. Schwartz. Adaptive Nonlocal Filtering: A Fast Alternative to Anisotropic Diffusion for Image Enhancement. IEEE Transactions on Pattern Analysis and Machine Intelligence, (1999) 42.

[67] M.A. Delesse. Procédé méchanique pour déterminer la composition des roches. C. R. Acad. Sci., 25 (1847) 544.

[68] N. Epstein. On tortuosity and the tortuosity factor in flow and diffusion through porous media. Chemical Engineering Science, 44 (1989) 777.

[69] AVIZO Fire Reference Manual. Avizo XLab Hydro, theoretical elements. (2011).

[70] H. Darcy. Les fontaines pupliques de la ville de Dijon. V. Dalemont, (1856).

[71] K.M. Persson, V. Gekas, and G. Trägårdh. Study of membrane compaction and its influence on ultrafiltration water permeability. J.Membr.Sci., 100 (1995) 155.

[72] O. Reynolds. An experimental investigation of the circumstances which determine whether the motion of water shall be direct or sinuous, and of the law of resistance in parallel channels. Philosophical Transactions of the Royal Society, 174 (1883) 935.

[73] S. Whitaker. The Methode of Volume Averaging, Kluver Academic Publishers, 1999.

[74] F.H. She, K. Nihara, W.M. Gao, P.D. Hodgson, H. Jinnai, and L.X. Kong. 3-Dimensional characterization of membrane with nanoporous structure using TEM tomography and image analysis. Desalination, 250 (2010) 757.

[75] F.H. She, W.M. Gao, Z. Peng, P.D. Hodgson, and L.X. Kong. Micro- and nano-characterization of membrane materials. J Chin Inst Chem Eng, 39 (2008) 313.

[76] A. Wiegmann. Modeling and simulation of filtration processes - a practitioner´s overview, Proceedings WFC11 Graz, (2012) 14.

[77] T. Koch, D. Salaberger, A. Zankel, H. Reingruber, A. Steiger-Thirsfeld, Y. Voronko, et al. Methods for Characterizing the 3-D Morphology of Polymer Composites. Macromolecular Symposia, 315 (2012) 115.

[78] A. Zankel, H. Reingruber, and H. Schroettner. 3D Elemental Mapping in the ESEM. Imaging and Microscopy, 2 (2011) 35.

[79] E.W. Washburn. The Dynamics of Capillary Flow. Phys.Rev., 17 (1921) 273.

[80] L.R. Fisher, P.D. Lark. An experimental study of the washburn equation for liquid flow in very fine capillaries. J.Colloid Interface Sci., 69 (1979) 486.

[81] A. Hamraoui, T.y.p. Nylander. Analytical approach for the Lucas-Washburn equation. 250.

[82] L. Fisher. Physics takes the biscuit. Nature, 397 (1999) 469.

[83] D. Khrustalev, A. Faghri. Heat transfer in the inverted meniscus type evaporator at high heat fluxes. Int.J.Heat Mass Transfer, 38 (1995) 3091.

[84] E. Limpert, W.A. Stahel, and M. Abbt. Log-normal Distributions across the Sciences: Keys and Clues. BioScience, 51 (2001) 341.

[85] Kitching, Donald. Beam damage of polypropylene in the environmental scanning electron microscope: an FTIR study. J.Microsc., 190 (1998) 357.